OAK RIDGE
NATIONAL LABORATORY
MANAGED BY UT-BATTELLE
FOR THE DEPARTMENT OF ENERGY

ORNL/TM-2008/153

Energy and Transportation Science Division

Oak Ridge National Laboratory
Annual Progress Report for the Power Electronics and
Electric Machinery Program

Mitch Olszewski, Program Manager

October 2008

Prepared by
OAK RIDGE NATIONAL LABORATORY
Oak Ridge, Tennessee 37831
managed by
UT-BATTELLE, LLC
for the
U.S. DEPARTMENT OF ENERGY
under contract DE-AC05-00OR22725

UT-BATTELLE
ORNL-27 (4-00)

U.S. Department of Energy
FreedomCAR and Vehicle Technologies, EE-2G
1000 Independence Avenue, S.W.
Washington, D.C. 20585-0121

FY 2008

Oak Ridge National Laboratory
Annual Progress Report for the Power Electronics and Electric Machinery Program

Prepared by:

Oak Ridge National Laboratory

Mitch Olszewski, Program Manager

Submitted to:

Energy Efficiency and Renewable Energy
Vehicle Technologies Program

Susan A. Rogers, Technology Development Manager

October 2008

Contents

Page

Acronyms and Abbreviations

3D	3-dimensional
AEEMS	axially excited electromagnetic synchronous
AlN	aluminum nitride
APEEM	Advanced Power Electronics and Electric Machines
APF	active power filter
BCD	bipolar CMOS-DMOS
BeO	beryllium oxide
CMOS	complementary metal–oxide semiconductor
CPLD	complex programmable logic device
CSI	current source inverter
CVT	continuously variable transmission
DBC	direct-bonded copper
DMOS	double-diffused metal-oxide semiconductor
DOE	Department of Energy
DSP	digital signal processing
ECVT	electronically-controlled continuously variable transmission
EETT	Electrical and Electronics Technical Team
ESR	equivalent series resistance
EV	electric vehicle
FEA	finite element analysis
FreedomCAR	derived from “Freedom” and “Cooperative Automotive Research”
FSCW	fractional-slot concentrated windings
FUDS	Federal Urban Driving Schedule
HEV	hybrid electric vehicle
IC	integrated circuit
ICE	internal combustion engine
IGBT	insulated gate bipolar transistor
INV/CONV	inverter/converter
IPM	interior permanent magnet
JFET	junction field effect transistor
MG	motor/generator
MOSFET	metal-oxide semiconductor field-effect transistor
NMOS	negative-channel metal-oxide semiconductor

OEM	original equipment manufacturer
ORNL	Oak Ridge National Laboratory
PCB	printed circuit board
PCU	power converter unit
PHEV	plug-in hybrid electric vehicle
PM	permanent magnet
PMOS	positive-channel metal-oxide semiconductor
PWM	pulse-width modification
SiC	silicon carbide
SOI	silicon-on-insulator
SR	set/reset
TC	temperature coefficient
THD	total harmonic distortion
VSATT	Vehicle Systems Analysis Technical Team
VSI	voltage source inverter
VTP	Vehicle Technologies Program
WBG	wide-bandgap
WEG	water–ethylene glycol
ZSIN	zero-sequence impedance networks

1. Introduction

The U.S. Department of Energy (DOE) and the U.S. Council for Automotive Research (composed of automakers Ford, General Motors, and Chrysler) announced in January 2002 a new cooperative research effort. Known as FreedomCAR (derived from "Freedom" and "Cooperative Automotive Research"), it represents DOE's commitment to developing public/private partnerships to fund high-risk, high-payoff research into advanced automotive technologies. Efficient fuel cell technology, which uses hydrogen to power automobiles without air pollution, is a very promising pathway to achieve the ultimate vision. The new partnership replaces and builds upon the Partnership for a New Generation of Vehicles initiative that ran from 1993 through 2001.

The Advanced Power Electronics and Electric Machines (APEEM) subprogram within the Vehicle Technologies Program provides support and guidance for many cutting-edge automotive technologies now under development. Research is focused on understanding and improving the way the various new components of tomorrow's automobiles will function as a unified system to improve fuel efficiency. In supporting the development of hybrid propulsion systems, the APEEM effort has enabled the development of technologies that will significantly improve advanced vehicle efficiency, costs, and fuel economy.

The APEEM subprogram supports the efforts of the FreedomCAR and Fuel Partnership through a three-phase approach intended to

- identify overall propulsion and vehicle-related needs by analyzing programmatic goals and reviewing industry's recommendations and requirements and then develop the appropriate technical targets for systems, subsystems, and component research and development activities;
- develop and validate individual subsystems and components, including electric motors, and power electronics; and
- determine how well the components and subsystems work together in a vehicle environment or as a complete propulsion system and whether the efficiency and performance targets at the vehicle level have been achieved.

The research performed under this subprogram will help remove technical and cost barriers to enable the development of technology for use in such advanced vehicles as hybrid electric vehicles (HEVs), plug-in HEVs, and fuel-cell–powered automobiles that meet the goals of the Vehicle Technologies Program. A key element in making HEVs practical is providing an affordable electric traction drive system. This will require attaining weight, volume, and cost targets for the power electronics and electrical machines subsystems of the traction drive system. Areas of development include these:

- novel traction motor designs that result in increased power density and lower cost;
- inverter technologies involving new topologies to achieve higher efficiency and the ability to accommodate higher-temperature environments;
- converter concepts that employ means of reducing the component count and integrating functionality to decrease size, weight, and cost;
- more effective thermal control and packaging technologies; and
- integrated motor/inverter concepts.

The Oak Ridge National Laboratory's (ORNL's) Power Electronics and Electric Machinery Research Center conducts fundamental research, evaluates hardware, and assists in the technical direction of the DOE Vehicle Technologies Program, APEEM subprogram. In this role, ORNL serves on the FreedomCAR Electrical and Electronics Technical Team, evaluates proposals for DOE, and lends its technological expertise to the direction of projects and evaluation of developing technologies.

ORNL also executes specific projects for DOE. The following report discusses those projects carried out in FY 2008 and conveys highlights of their accomplishments. Numerous project reviews, technical reports, and papers have been published for these efforts, if the reader is interested in pursuing details of the work.

Below are summaries of major accomplishments for each technical project.

Direct Water-Cooled Power Electronics Substrate

- Candidate materials and processing methods were identified for a direct-cooled power electronics substrate.
- The optimum ceramic materials for maximum heat transfer were determined.
- Design analysis and thermal and structural finite element analysis (FEA) were completed on five designs.
- An ongoing effort to analyze the compatibility of ceramic substrates with water/ethylene glycol continued.
- A technical report was completed as part of this effort.

Uncluttered Rotor Permanent Magnet Machine for Continuously Variable Transmission Design

- A design was developed conforming to the overall dimensions of the baseline (Toyota Prius) machine.
- Simulations indicate that the radial-gap continuously variable transmission provides a significant torque increase of 30% with a weight gain of only 15%.
- Significant advances were accomplished in the simulation and design of highly complex machines using the uncluttered rotor principle with 3-dimensional flux paths.

Axially Excited Electro-Magnetic Synchronous Rotor Motor

- Mechanical stator and rotor designs were completed to provide a basic model for FEA of the magnetic performance of the motor. The design was based on a basic stator configuration and size, such as the Prius drive. A unique rotor configuration was developed along with axial excitation poles to magnetically excite the rotor.
- FEA modeling was performed.
- A feasible design was shown yielding estimates of specific power equal to1 kW/kg and a volumetric power density equal to 5 kW/L.

Application of Concentrated Windings to Electric Motors without Surface-Mounted PMs

- The analysis of a 9-slot, 8-pole interior permanent magnet (IPM) with concentrated windings was completed and compared with a 48-slot, 8-pole baseline IPM with distributed windings.
- Both motor designs were simulated and a comparison was performed of their performance running the US6 and Federal Urban Driving Schedule drive cycles using ORNL's vehicle simulator.
- It was concluded that benefits can be obtained in reduced torque ripple, reduced copper losses, and increases in efficiency with IPM concentrated winding machines. However, the power demands of the US6 cycle required increasing the gear ratio above the baseline gear ratio.

Amorphous Core Material Evaluation

- The evaluation of these materials concluded that the unavailability of bulk manufacturable amorphous core material and high material costs will continue to prevent *radial-gap* motors from meeting cost targets.
- FEA simulations were performed with amorphous core material in existing motor designs yielding low saturation flux densities.

- Use of this material will require specific motor designs developed to optimize and realize the gains potentially available from this material.

Wide-Bandgap Materials

- Efforts were continued in FY 2008 to characterize, model, and simulate new wide-bandgap devices as they became available from various vendors
- A novel integrated motor/inverter packaging concept using silicon carbide devices was developed. Further work on the design will be continued into the next fiscal year.

An Active Filter Approach to the Reduction of the dc Link Capacitor

- The first year of the project included establishing requirements for an active filter and identifying a specific topology to use.
- An active power filter was designed to replace the dc link capacitor and simulated to ascertain the tradeoffs with its viability in replacing the dc link capacitors.

Advanced Converter Systems for High-Temperature HEV Environments

- A 30 kW continuous, 55 kW peak power buck/boost dc-dc converter was designed, assembled, and tested to prove the benefits of the topology.
- The prototype yielded efficiencies in the 97–98% range during laboratory testing.
- A power density of 8.5 kW/kg and 17.8 kW/l was achieved with the low-temperature prototype.
- A second-generation silicon-on-insulator gate driver chip was developed and tested.

Current Source Inverter for HEVs and Fuel Cell vehicles

- A 55 kW prototype was designed, built, and successfully tested.
- The prototype was able to achieve a reduction in total capacitance to 195μF.
- A voltage boost ratio of up to 3.47 was demonstrated.
- The output voltage total harmonic distortion factor was lower than 12.5%.

Using the Traction Drive Power Electronics System to Provide Plug-in Capability for HEVs

- A prototype of a 55 kW plug-in HEV traction drive inverter with a charging capability of 20 kW was designed, fabricated, and tested.
- Testing was conducted over a load range of 1–14 kW.
- The prototype achieved measured efficiencies between 92 and 97%.
- The total harmonic distortion of the ac current was less than 10% over a wide range of charging power.

Benchmarking of Competitive Technologies

- The Toyota Lexus LS600H was successfully benchmarked.
- Efficiency maps for the modules were generated and destructive teardowns of the modules were completed to determine manufacturing, packaging, and thermal design issues.
- The bus capacitors and motor magnets were analyzed over a temperature range as part of the teardown.
- A technical report was completed detailing the work.

2. Thermal Management Systems

2.1 Direct-Cooled Power Electronics Substrate

Principal Investigator: Randy H. Wiles
Oak Ridge National Laboratory
National Transportation Research Center
2360 Cherahala Boulevard
Knoxville, TN 37932
Voice: 865-946-1319; Fax: 865-946-1262; E-mail: zhr@ornl.gov

DOE Technology Development Manager: Susan A. Rogers
Voice: 202-586-8997; Fax: 202-586-1600; E-mail: Susan.Rogers@ee.doe.gov

ORNL Program Manager: Mitch Olszewski
Voice: 865-946-1350; Fax: 865-946-1262; E-mail: olszewskim@ornl.gov

---

Objectives

- Develop and model an innovative power electronics mounting structure (direct-bonded copper [DBC] substrate) for an inverter that is directly cooled by water-ethylene glycol (WEG), thus eliminating the conventional heat sink and associated heat flow path.
- Reduce the size and weight of the heat sink for power electronics used in hybrid electric and plug-in hybrid electric vehicles (HEVs and PHEVs, respectively).
- Determine the feasibility of a design that directly cools the DBC, preferably using a 105°C coolant temperature.
- Develop mechanical and thermal models of an inverter substrate to predict performance.
- Research manufacturing capabilities and methods that will support the substrate designs.

Approach

- Determine the optimum ceramic materials for maximum heat transfer and minimum cost.
- Evaluate candidate materials and processing methods for a direct-cooled power electronics substrate.
- Select chip sets that will meet the inverter power requirement.
- Establish design parameters for computer models:
  - — determine appropriate thermal load for 3-dimensional simulations
  - — justify the number of chips to use for specific designs
  - — create metrics for a successful design
- Perform finite-element analysis (FEA) to optimize heat transfer characteristics of the assembly.

Major Accomplishments

- Design parameters established.
- Thermal FEA completed on five substrate designs.
- Mechanical stress FEA completed on the two preferred designs.
- Commercial processing methods identified and evaluated.

Future Direction

- Fabrication of preferred design(s).
- Laboratory testing to validate performance relative to modeling results.
- Complete designs based on laboratory results and integrate substrate into inverter package.

Technical Discussion

As consumer interest grows in HEVs and PHEVs, manufacturers are challenged to offer these technologies at reduced costs. The automotive manufacturer's goal is to reduce the price of these vehicles relative to the cost of traditional internal combustion engine (ICE) –powered vehicles. The thermal management of the power electronic systems that must be implemented into these products constitutes a large cost to both manufacturers and consumers. Currently, HEVs utilize two cooling loops. One cooling loop is for the ICE, which operates at approximately 105°C, and a second coolant loop is for the power electronics modules, which operates near 70°C. One way to significantly reduce the cost to both manufacturers and consumers is to use a single coolant loop for both the ICE and power electronics using 105°C coolant as the primary means of heat dissipation.

The purpose of this research and development project is to design a direct-cooled power electronics substrate that would enable the automotive manufacturers to use 105°C coolant, thus eliminating the secondary coolant loop. Thermal performance and mechanical stress FEA were performed on design concepts to ensure they satisfied the design criteria for material strength and thermal heat dissipation. Surveys were also conducted of manufacturers' capabilities and methods that supported the substrate design and fabrication.

Information contained in this annual report serves as a general discussion of this research effort. For more detailed information, please refer to ORNL/TM-2008/112. This report is a "Limited Distribution" report and is classified for Official Use Only. It will be released to the general public after the Oak Ridge National Laboratory (ORNL) patent office publishes the patent for the technology.

Proposed Solution

To enable cooling of the inverter with 105°C WEG, alternative cooling strategies are under consideration. One involves positioning the 105°C coolant as close to the silicon insulated gate bipolar transistor (IGBT) and diode as possible through the use of a (electrically insulating) ceramic heat exchanger.

A uniquely shaped structure was developed that allows for a compact chip layout, provides excellent sealing surfaces, and adequate space to incorporate coolant channels. This structure was designed with highly thermally conductive materials and allows enough surface area for the switches to be sintered/soldered to the assembly. Utilizing a lower thermal-conductivity material, such as alumina, necessitates increasing the width of the structure. This is necessary for heat dissipation. In either case, the length of the entire ceramic structure was maintained at a minimum for volume considerations. This length provides enough surface area for the switches, wire bonds, electrical connections, and sealing surfaces. Issues associated with sealing the substrate were also a concern. The rounded ends of the structure will provide an excellent sealing surface, as opposed to the flat plate designs that are common in micro-channel research. Because of manufacturing restrictions and automotive manufacturer guidelines, typical thin, flat plate DBC substrates are not feasible for direct cooling. More cross-sectional area has to be created to incorporate flow channels to remove the heat.

Additional concepts under consideration incorporate an annular coolant channel into which a thermal enhancement material is placed. In any design case, the ceramic in the substrate would serve the same primary role as a ceramic in a conventional DBC; namely, it would be an electrical insulator. The

substrate would then be metalized with copper to facilitate bonding (e.g., soldering or sintering) to a silicon IGBT and diode.

Candidate Materials and Processing Methods for a Direct-Cooled Power Electronics Substrate

Ceramic materials were sought that combine electrical insulation (>109 ohm-cm), the potential to be chemically compatible with WEG, good thermal conductivity (>50 W/mK), modest tensile strength (>200 MPa), and minimum cost. Candidate materials are listed in the following table.

Table 1. Candidate ceramic materials for a direct-cooled power electronic substrate

Candidate ceramic	Electrical insulation	Thermal conductivity	Cost	Chemical compatibility with WEG
Aluminum oxide or alumina (Al_2O_3)	Excellent	Fair	Low	Probably good
Aluminum nitride (AlN)	Excellent	Excellent	High	Unknown
Silicon nitride (Si_3N_4)	Excellent	Fair to good	High	Unknown
High-resistivity polycrystalline silicon carbide (SiC)	Could be excellent	Good to excellent	Medium to high	Unknown
Beryllium oxide (BeO)	Excellent	Excellent	Medium	Unknown

Some of the candidate ceramic materials are documented [1, 2] as being unstable when in contact with moisture. To examine the mechanical stability of the ceramics in contact with WEG, a series of strength and fatigue tests were performed on aluminum nitride (AlN), aluminum oxide (Al_2O_3), silicon nitride (Si_3N_4), and silicon carbide (SiC) after they were immersed in and impinged with WEG. Preliminary indications are that each material had no dramatic decrease in strength from contact with WEG; however, scanning electron microscopy of ceramic surfaces subjected to WEG impingement for 590 hours shows that erosion is occurring, probably as a result of a chemical reaction between the AlN and WEG. Longer-term studies are continuing. Additionally, electrical resistivity tests were also completed on the ceramic candidates at 25, 200 and 325°C. The results from the electrical resistivity tests showed that each of the candidate ceramic materials maintained an electrical resistivity of between 10^{-9} and 10^{-12} Ω-cm, which is well within the range of insulating materials. Complete results of the testing are documented in ORNL/TM-2008/112.

Ceramic Processing Methods

Ceramic processing methods were identified that could be used to produce a direct-cooled DBC. The manufacturing techniques should combine two characteristics: they should be capable of producing small-scale features (e.g., hole diameters of 1 mm or 0.040 in. or less) in a structure up to 50 mm in length and be mature processes with the capability for large-scale manufacturing applicable to the automotive industry. Four identified ceramic processing methods described in the following sections are considered to be "green-state" fabrication techniques; that is, they are methods that form processed ceramic powder into some desired shape at or near ambient temperature. The following sections describe these current state-of-the-art processing methods that satisfy the fabrication requirements.

Dry Pressing

Dry pressing is one of the most traditional ceramic processing methods. Its advantages are that most ceramic manufacturers are adept at it, it is a mature technology, it is relatively inexpensive, and it is amenable for mass production. Dry pressing alone could not produce the ORNL concept structure, so manufacturers would need to perform green-state machining of the dry-pressed billet to achieve the unique shape and to incorporate the coolant channels. Green-state machining is attractive because

conventional grinding and machining tools can be used, whereas (expensive) diamond tooling is required for machining after a ceramic has been sintered. The disadvantage of this method is that the architecture can be limited by what can be accomplished during green-state machining. For example, very small thru-hole diameters (e.g., 1 mm or 0.040 in.) may be difficult to produce in the ceramic's green state and maintain through the sintering process.

Extrusion

Extrusion is another traditional ceramic processing method. Like dry pressing, its advantages are that many ceramic manufacturers are experienced with it; it is a mature technology; it is relatively inexpensive; and it is amenable for mass production. Like dry pressing, extrusion alone could not produce the ORNL concept structure. Green-state machining would be needed; therefore, fine-scale-features of the final architecture could be limited.

Injection Molding

Injection molding can produce high-precision ceramic parts (e.g., ± 25 μm = ± 0.001 in.) in small or large sizes. It can yield high production volumes (tens of thousands to millions), can be adapted to almost any design, and results in low labor and costs. Another advantage of injection molding is machining costs can often be minimized once die and tooling have been optimized. It avoids the limitations inherent to green-state machining of dry-pressed or extruded billets in that internal features are not limited by symmetry and can be very complex if desired. For example, a helical pattern can be incorporated in a coolant channel to better promote turbulent flow of the WEG.

Ceramatec Process

The Ceramatec process combines tape casting, laser machining of the green tapes, and lamination to produce ceramic components with complex internal channels. Fine tolerances can be achieved, and the process is mature and is under consideration for a wide range of ion transport membrane technologies. Large dimensions are achievable in two of the three dimensions. The mass production capability of this process is not as good as that of dry pressing, extrusion, or injection molding.

Numerous candidate ceramic manufacturers have been identified. All have large-scale ceramic manufacturing capabilities, presently have sizeable ceramic markets, and could satisfactorily manufacture the ORNL concept structure. All were contacted about the heat exchanger concept, and its manufacturability was discussed.

Chip Set Selection

The primary rating of a silicon device is its current-voltage (I-V) characteristics, which dictate how much current the device can conduct at the expense of the forward voltage drop. For IGBTs, these curves depend on the applied gate voltage and junction temperature. For diodes, the characteristic curves are temperature dependent. It was determined that a silicon device can conduct rated current up to its maximum rated junction temperature as long as the waste heat being produced is consistently removed. Because these architectures eliminate large thermal resistances, more heat can be removed. This additional heat removal allows the chip to conduct at the rated current up to its maximum junction temperature.

The IGBT selected for use in modeling was an Infineon Technologies "trench type" IGBT. This chip has a maximum voltage rating of 600 V and a maximum current rating of 200 A. It possesses low $V_{CE(sat)}$, low turn-off losses, short tail current, and a positive temperature coefficient allowing it to be easily paralleled. The diode selected for use was an Infineon Technologies fast-switching diode chip in EMCON 3-Technology. This chip has a maximum voltage rating of 600 V and a maximum current rating of 200 A. It

possesses soft, fast switching characteristics, a low reverse recovery charge, and a small temperature coefficient. Both devices have maximum temperature operating ranges of –40 to 175°C.

Establish Design Parameters for Finite Element Analysis on 3-Dimensional Models for Heat Transfer Optimization

Determine Appropriate Thermal Load for 3-Dimensional Models

In previous research and development efforts, two inverter ratings were used in thermal models: 55 kW peak and 30 kW continuous. A constant efficiency in the inverter over the entire operational range was also assumed in these previous efforts. Thus the thermal load could be determined for continuous and peak loading. However, these assumptions are not entirely valid. Data from ORNL's Semikron [3] testing (table below) show that waste heat magnitudes can approach maximum values while the output is below the peak power rating. This result is due to decreases in efficiencies based on running conditions.

Waste heat produced by Semikron inverter for different output powers

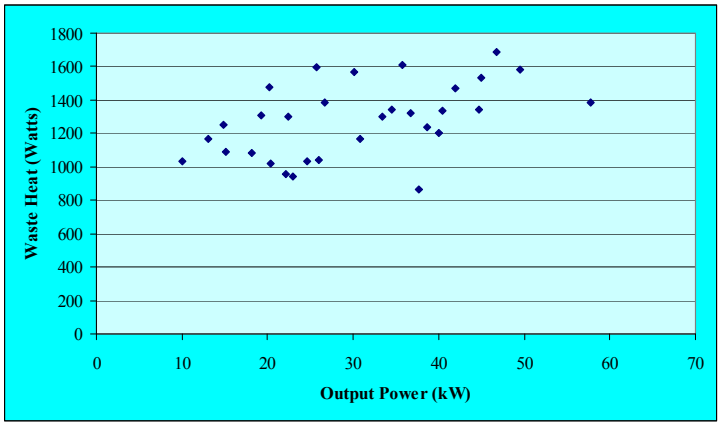

An approximate waste heat distribution for this architecture can be found using Semikron testing evaluation results and a maximum waste heat of 1,746 W. Assuming that the upper and lower leg of each phase will dissipate equal amounts of energy over an operational period, the heat loss per concept structure is 291 W. Each section will have two diodes and three or four IGBTs. It is assumed that the diode losses are about a third of the switch losses. This approximation is based on an application note from Semikron [4].

Using this ratio and four IGBTs per section implies that 75% of the loss will come from the switches and 25% from the diodes, or 54.6 W in losses per switch and 36.4 W in losses per diode. If three switches were used, the losses would be 72.75 W per switch and 36.4 W per diode. No attempt will be made to justify a continuous operating loss because of the efficiency dependency of the heat losses. Furthermore, using the maximum losses allows the design to be configured for the worst-case scenario. The design should then provide more than adequate cooling for transient power fluctuations and continuous load.

In this study, the heat load for the IGBT was varied to simulate the number of switches used for each half electrical phase. A minimum of three switches is required to achieve the current rating that is required for the inverter. Because the devices are being run on the upper end of their operational range, four switches may be used to spread the losses of the inverter out over a wider area and to add a margin of safety. The computer models will predict the maximum temperatures to determine if the selected chip population is a viable option.

Other Analysis Parameters

The fluid inlet velocity varied depending on flow channel size. Initial inlet velocity was consistent with a total inverter flow rate set at 2.5 gallons per minute (GPM). Each of the five designs should be able to pass a 1 mm particle through the flow channels; however, filtering of the coolant may be necessary; this will be determined during component testing. Fluid inlet temperatures were specified at 105°C. All other boundaries were modeled as thermally insulated. This assumption allows for a conservative design, and the actual thermal performance should result in lower junction and fluid temperatures because of other minor heat losses. The material properties used in the FEA modeling can be found in ORNL/TM-2008/112.

Determining the Thermal Performance Criteria

For a design to be considered successful, the thermal models must predict junction temperatures below 175°C and preferably below 150°C. Also, the coolant temperatures must be maintained below the boiling point of a 50/50 WEG mixture so that original equipment manufacturers (OEMs) do not have to alter system pressure ratings. Boiling points for 50/50 mixes of WEG for various system pressures can be found in ORNL/TM-2008/112. The coolant temperature performance criterion used in developing the models was limited to 130°C, which corresponds to 16 psig. As a consequence of concurrently satisfying these constraints and designing a practical direct-cooled ceramic substrate, five different substrate designs were ultimately considered.

Thermal FEA Results for 3-Dimensional Designs

Thermal Performance of Design 1

In Design 1, multiple flow channels are placed through the ceramic structure. They are equally spaced on a bolt circle that maintains a minimum distance of 0.050 in. between surfaces. The minimum distance is maintained to provide structural integrity and is based on ceramic manufacturing limitations.

When a load of 55 W per chip is applied, the maximum projected junction temperature is 141.7°C, and the maximum fluid temperature is 136.5°C for AlN. When Al_2O_3 is used, the projected junction temperature is 182.9ºC and the maximum fluid temperature is 163.0ºC. With SiC, the projected junction temperature is 144.7ºC and the maximum fluid temperature is 138.8ºC. If BeO is used, the projected junction temperature is 143.0ºC and the maximum fluid temperature is 137.5ºC. In each case using different ceramic materials, the maximum fluid temperature exceeds the boiling point with the load resulting from four switches. Therefore, no model needs to be run for the larger load that corresponds to three switches, as the increased load would increase both maximum junction temperature and fluid temperature.

Variations in the WEG mixture were investigated briefly to see if a temperature decrease would result from increasing the thermal conductivity of the solution. Solutions of 60/40 and 70/30 WEG were modeled. The maximum fluid temperatures did decrease but only by about a degree Celsius for each 10% reduction in ethylene glycol. Unfortunately, the boiling points also readjust for the new mix ratios. The boiling points also dropped by about a degree Celsius for each 10% reduction in ethylene glycol; thus the relative difference in maximum fluid temperature to allowable boiling points was constant. Therefore, no noticeable benefit is obtained from altering the fluid mixture from 50/50 WEG.

Thermal Performance of Design 2

Because Design 1 resulted in a maximum fluid temperature that exceeded the boiling point, other options were explored. In order to enhance the thermal conductivity of the fluid, a thermal enhancement material was added to the flow channels. The addition of a thermal enhancer into the flow channels provided a greater surface area within the flow channel to remove the waste heat more efficiently. The selected

material has a much higher structural integrity compared with other types of microstructures and provided a simple means of manufacturing.

The properties for the flow channel must be adjusted to reflect the addition of the thermal enhancement material. Also, the velocity of the inlet must be calculated for an effective area, because the thermal enhancement material blocks some of the inlet area. The material properties of the thermal enhancement material used in modeling the thermal data can be found in ORNL/TM-2008/112. Plug flow was assumed for the flow channels. This assumption is valid based on Darcy's Law for flow through porous media. In short, the thermal enhancement material prohibits boundary layer formation along the walls of the channel, which results in plug type flow.

The maximum fluid temperature is 122.7°C and the maximum projected junction is 129.3°C for AlN with an aluminum thermal enhancement material added to the flow channel and four switches. If BeO is used, the maximum junction temperature is 130.6ºC and the maximum fluid temperature is 123.1°C. When Al_2O_3 is used, the maximum junction temperature is 171.5°C and the maximum fluid temperature is 133.4°C. If SiC is used, the maximum junction temperature is 131.9°C and the maximum fluid temperature is 123.7°C. Results of the model containing an alternative thermal enhancement material in the flow channel can be found in ORNL/TM-2008/112.

The thermal enhancement material adds another benefit in that it can restrict bubble growth in the event of boiling. In an open channel design, bubbles can grow to the point of blocking flow. Furthermore, as a bubble develops on the wall, it creates a local hot spot which could be detrimental to a chip. The thermal enhancement material limits the bubble growth size. Thus if boiling were to occur, which the models do not predict, it could neither significantly block the flow nor create a large hot spot near the wall.

Thermal Performance of Design 3

Design 3 contains one coolant flow channel. This flow channel is filled with a thermal enhancement material. Using a total of four switches and a thermal enhancement material, the maximum junction temperature for AlN is 142.3°C and the maximum fluid temperature is 126.1°C. For BeO, the maximum junction temperature is 143.8°C and the maximum fluid temperature is 126.3°C. If Al_2O_3 is used, the maximum junction temperature is 224.4°C and the maximum fluid temperature is 127.9°C. If SiC is used, the maximum junction temperature is 145.9°C and the maximum fluid temperature is 126.4°C. For three switches using AlN, the temperatures remain within the performance criteria with a maximum junction of 147.9°C and a maximum fluid temperature of 125.6°C. Results of the model containing an alternative thermal enhancement material in the flow channel can be found in ORNL/TM-2008/112.

Thermal Performance of Design 4

After the previous designs for all materials were examined, it became obvious that it would be necessary to explore lower-cost options for the higher-thermal-conductivity materials (AlN, BeO, and SiC). Even though their thermal performance is far superior to that of Al_2O_3, substrates made of these materials would cost almost as much as the whole inverter at the current OEM's cost target. Additionally, concern was beginning to mount over the chemical compatibility of AlN with WEG (and therefore the potential for AlN erosion), lending a further rationale for considering Al_2O_3 because it is chemically inert against WEG.

In this geometry the minimum distance from the exterior of the ceramic shape to the flow channel can be smaller than in the previous models. This smaller distance is a result of an increase in local velocities created by the unique shape. In this design, the maximum chip temperature is 152°C and the maximum fluid temperature is below 125°C. Again, these temperatures satisfy the design temperature constraints. FEA results and probabilistic life design analyses showed that the maximum first-principles tensile

stresses from thermal loading were low and easily within the mechanical capability of the Al_2O_3 ceramic. The probability of survival analysis showed that 999,992 out of 1,000,000 ceramic structures (99.9992%) should sustain the imposed thermomechanical stresses without mechanical failure. Further optimization of this geometry could be explored to increase the probability of survival, but this model shows that an Al_2O_3 ceramic geometry is possible and actually quite viable.

This design also adds some other benefits. A common product with thermal enhancement material is a pipe with the enhancement material bonded onto the outer surface. In Design 4, this thermal enhancement subassembly could be pressed into a larger hole to form the annulus. The ends of the subassembly would have to be brazed closed to prevent a fluid bypass. However, the overall effect would reduce the weight of the substrate and should keep cost lower because less Al_2O_3 is needed to make the part than in a part with a solid core.

Thermal Performance of Design 5

To provide another design option with Al_2O_3, a multiple-flow channel design was explored. In this design process, the size of the flow channel filled with a thermal enhancement material, and the flow channel center location, were varied to determine an optimum design. In the final design iteration, the center of the hole was offset from the center of the chip to provide the coolest chip temperatures. The resulting temperatures proved that the offset dimension was critical for this design to meet the performance criteria.

The FEA ran on this model used a top silicon chip heat generation of 37 W to represent a diode and a side silicon chip heat generation of 55 W to represent an IGBT. The maximum chip temperature is 153°C and the maximum fluid temperature is below 125°C, and those meet the design temperature constraints. Again, these temperatures meet the maximum limits of the design parameters. FEA results and probabilistic life design analyses showed that the maximum first-principles tensile stresses from thermal loading were low and easily within the mechanical capability of the Al_2O_3 ceramic. The probability of survival analysis showed that 999,906 out of 1,000,000 ceramic structures (99.9906%) will sustain the imposed thermomechanical stresses without mechanical failure. Further optimization of this geometry could be explored to decrease the face-to-radius distance and increase the probability of survival, but this model shows that an Al_2O_3 ceramic geometry is possible and actually quite viable.

Design Results

Because of cost limitations, Designs 1–3 had to be modified in order to meet the design goals. These changes resulted in Designs 4 and 5, which show that 105°C coolant can be used with an Al_2O_3 substrate. These substrates will be joined by a manifold placed inside the capacitor. This design layout is similar to the refrigerant-cooled inverter researched by ORNL [5].

The capacitor(s) necessary to complete the inverter design dictates the overall volume of the direct-cooled power electronics substrate. Since this component has a larger volume than many of the other required components, volume reduction can be limited by the physical size of the capacitor. Based on capacitor designs obtained from the SBE, Inc., Power Ring Division, the preferred design in this research and development effort has a power density approaching 14 kW/L. However, this preferred design uses a ceramic substrate with a high-thermal-conductivity capability, which comes at a higher cost. If a lower-cost ceramic substrate is used, such as alumina, the cost is significantly reduced but the power density approaches 7.5 kW/L because of the size of the substrate necessary to spread the thermal load.

Cost Comparison

The direct-cooled power electronics substrate project is a totally new concept and therefore untried in industry. Costs can be quantified on conventional inverter architectures based on component purchase prices, material costs, and manufacturing assembly costs. The tangible expenses in this research effort are

material costs, fabrication costs for ceramic components, and estimated cost savings from the elimination of the conventional heat sink, the base plate/heat spreader, and the thermal interface material (TIM). Each of the ceramic fabrication costs is listed in the table below and is based on material and tooling costs per 100,000 pieces.

Table 2. Cost summary for ceramic materials considered in the fabrication of a direct-cooled power electronics substrate.

Description	Material extrusion cost	Copper plating	Purchase price	Total cost per inverter
Aluminum nitride	$45.87	$3.12	$48.99	$293.94
Alumina	$2.97	$3.12	$6.09	$36.54
Silicon carbide	$30.25	$3.12	$33.37	$200.22
Beryllium oxide	$19.59	$3.12	$22.71	$136.26

If the ceramic of choice in the final inverter design were Al_2O_3, based on the information in the table above, the cost to produce the copper-plated ceramic substrate in a quantity of 100,000 units would be approximately $36.54. The savings from a conventional inverter, such as Semikron, would be $64.02 from just the elimination of the heat sink and the base plate. Additional savings would be realized by the elimination of the TIM, as well as a weight savings of ~3 kg per inverter in this research effort because the base plate and heat sink would not be required. These cost savings do not take into account the wire bonds or the cost of the IGBTs and diodes or the capacitor, since these costs are widely known for any inverter structure in mass production.

Design Matrix Summary

To help evaluate the effectiveness of each design, a performance matrix and weight system was developed. It contains the loads, thermal data, manufacturing variables and trade-offs, and cost. In addition, velocities were determined for each design that exceeded the performance criteria to determine how much flow increase would be required to meet the design intent. This increase in velocity was helpful in determining the preferred designs; however, an OEM recommended the volumetric flow rate be maintained at a maximum of 2.5 GPM. For a complete design matrix summary of each design, please refer to ORNL/TM-2008/112. Designs 4 and 5 meet the OEM's cost and performance targets.

Conclusion

This research effort concludes that directly cooling an Al_2O_3 ceramic substrate with 105°C coolant while maintaining silicon temperatures below their maximum operation temperature is viable. The shape of the substrate, the size and shape of the capacitor, the coolant flow channels, a thermal enhancement material placed within the flow channels, and the chip population on the substrate all play a key role. The unique shape of the designs discussed in this report were chosen because the required surface area could be obtained within the smallest package volume. Additionally, the unique structure of the shape is far easier to seal from the coolant than other types of planer structural shapes.

The addition of a thermal enhancement material into the flow channels provided a greater surface area within the flow channel to remove the waste heat more efficiently. This thermal enhancement material has a much higher structural integrity than other types of microstructures and provided a simple means of manufacture. FEA results were run using two types of thermal enhancement material; however, cost, availability, and environmental concerns due to manufacturability of the higher-thermal-conductivity material steered this research effort toward a more cost-effective approach.

The capacitor(s) necessary to complete the inverter design dictates the overall volume of the direct-cooled power electronics inverter. Since this component has a larger volume than many of the other required

components, volume reduction can be limited by its size. The preferred design in this research and development effort has a power density approaching 14 kW/L. However, this preferred design uses a ceramic substrate with a high-thermal-conductivity capability, which comes at a higher cost. If a lower-cost ceramic substrate is used, such as alumina, the cost is significantly reduced but the power density approaches 7.5 kilowatts kW/L as a result of the size of the substrate necessary to spread the thermal load.

Performance testing of Designs 4 and 5 will be performed to validate the FEA results. These designs meet the specified design criteria while providing a lower cost to the OEMs. Additionally, Designs 2 and 3 met the specified design criteria but at a higher cost. They could be constructed with three or four chips so long as the coolant system pressure is kept high enough to prevent boiling but low enough that the OEMs do not have to alter conventional radiator components. For initial bench testing in FY 2009, diodes will be used on Designs 4 and 5 to generate the waste heat needed to validate the modeling.

Publications

R. H. Wiles, C. W. Ayers, A. W. Wereszczak, and K. T. Lowe, *Direct Cooled Power Electronics Substrate,* ORNL/TM-2008/112, Oak Ridge National Laboratory, 2008.

Kirk T. Lowe and Rao V. Arimilli, "Application of Solution Mapping to Reduce Computational Time for Actively Cooled Power Electronics," in *Proceedings of the 4th Annual Comsol Conference*, in press.

References

1. Chung-Daw Young and Jeng-Gong Duh, "Corrosion of aluminum nitride substrates in acid, alkaline solutions and water," *Journal of Materials Science,* **30**(1), 185–195 (January 1, 1995).
2. S. Fukumoto, T. Hookabe, H. Tsubakino, "Hydrolysis behavior of aluminum nitride in various solutions," *Journal of Materials Science,* **35**(11), 2743–2748 (June 2000).
3. *Testing of the Semikron Validation AIPM Unit at the Oak Ridge National Laboratory – January 2005*, ORNL/TM-2005/44.
4. P. Salvati, F. Brucchi, and A. De Medici, "Sinusoidal inverter using SEMITOP® modules for electric vehicles applications," Application Note: SemiKron.
5. "Thermal control for inverters and motors," in *Annual Progress Report for the Advanced Power Electronics and Electric Machinery Program,* Oak Ridge National Laboratory, 2007.

Patents

Randy H. Wiles, Andrew A. Wereszczak, Curtis W. Ayers, and Kirk T. Lowe, "Direct Cooled Power Electronics Substrate," provisional patent number 61/037,129, March 17, 2008.

3. Electric Machinery Research and Technology Development

3.1 Uncluttered Rotor PM Machine for a CVT Design

Principal Investigator: Donald J. Adams
Principal Technical Investigator: John S. Hsu
Oak Ridge National Laboratory
National Transportation Research Center
2360 Cherahala Boulevard
Knoxville, TN 37932
Voice: 865-946-1321; Fax: 865-946-1262; E-mail:adamsdj@ornl.gov

DOE Technology Development Manager: Susan A. Rogers
Voice: 202-586-8997; Fax: 202-586-1600; E-mail: Susan.Rogers@ee.doe.gov

ORNL Program Manager: Mitch Olszewski
Voice: 865-946-1350; Fax: 865-946-1262; E-mail: olszewskim@ornl.gov

---

Objectives

- Develop a new machine that combines the motor and generator/motor into one unit with the potential to be used as a continuously variable transmission (CVT), as well as other applications that require two electric machines. The expected advantages of this new machine are
  - Additional torque coupling between the two rotors for producing more wheel torque
  - The potential for a simpler, less costly CVT from combining a motor and generator into one machine with only a single permanent magnet (PM) rotor
  - Brushless design
  - Based on the uncluttered rotor principle, the concept can be extended for kinetic energy storage to reduce battery stress

Approach

Because the use of a secondary rotor working in conjunction with a PM rotor is a totally new technology, there is no previous experience that can be used for reference. The development process is an iterative process in determining the positive and negative aspects of various structural arrangements through both mechanical finite element analysis (FEA) and electromagnetic simulations. Numerous challenges associated with this technology and the process required to model, simulate, and derive results are to be addressed for complex 3-dimensional (3D) models.

The FY 2008 goal was to continue the modeling and simulation of the CVT, derive motor characteristics and parameters from the simulations, and perform a first order cost evaluation.

Major Accomplishments

In FY 2006 a proof-of-concept secondary rotor that had no rotating windings, and a wound core stator for exciting the secondary rotor, were fabricated. The brushless secondary rotor concept was validated through tests conducted on a prototype motor. The physics of the CVT machine were explained in the FY 2006 report.

In FY 2007, simulations were initially conducted for axial-gap and radial-gap approaches. The radial-gap machine was selected for detailed simulations. The simulation results further confirmed that the principle

of this new type of machine is workable; the torque of the PM rotor can be transferred directly to that of the secondary rotor, the stationary excitation core of the secondary rotor sees no rotational torque, and the axial force can be practically eliminated by an axially symmetrical arrangement.

In FY 2008 it became evident that modeling and verifiable simulation of such a complex electromagnetic machine is extremely difficult. The simulations require considerable computer power and time, resulting in slower progress on the work. This truly is a novel machine and to our knowledge no such simulation had been done before. Nevertheless, a design was demonstarted in simulations that resulted in a 30% effective power increase with only a 15% weight increase compared with the baseline machine (a Toyota Prius).

Future Direction

Because of budgetary constraints in FY 2008, a decision was made not to continue this particular project into FY 2009 as planned and not to build a prototype. Much was learned during this project about the behavior of complex electric machines and how to simulate and design such a machine with a significant 3D flux component. This knowledge and the tools developed during this project will be utilized in future projects, some of which have already been selected for funding in FY 2009.

This study proves that the uncluttered rotor concept can be used for the radial-gap electric machine structure. The axial-gap structure is somewhat easier to fit geometrically because it has more room available for the uncluttered rotor and its excitation. Moreover, this machine has a much wider impact than what is shown from the radial-gap model simulations, because the uncluttered rotor opens a door for new types of electric machines that require a brushless rotating armature. Such a machine can be used in numerous applications in addition to hybrid-electric-type automotive applications.

Technical Discussion

The old traditional brush-type electric machines, such as the commutator dc motor and the slip-ring synchronous machine, rely on brushes and/or slip rings to transfer the electric energy to rotating components without speed interference. For example, the brushes and slip rings of a wound field synchronous machine can deliver a dc current to the excitation field coil. Regardless of the rotor speed, the dc current going through the brushes would not be cluttered by the rotation frequency. This is quite different from using a wound stator that has the same number of poles as the wound rotor for energy transfer to the rotor. The frequency of the induced electromotive force in the wound rotor is linearly proportional to the speed of the rotor. The rotation frequency is cluttered into the rotor-induced voltage. The uncluttered rotor developed at Oak Ridge National Laboratory (ORNL) specifically solves this cluttering problem.

The uncluttered rotor concept opens a door for advanced brushless machine developments. The CVT in this study relies on the uncluttered rotor to transfer electric energy through the magnetic flux coupling that does not require a set of contacting slip rings and brushes. The uncluttered rotor can be viewed as a rotating stator (or armature) without brushes.

Besides the use of the uncluttered rotor for brushless energy transfer, the CVT of this investigation utilizes the counter torque of a rotating armature for torque amplification. This concept is explained through Fig. 1.

The upper sketch in Fig. 1 shows a traditional motor with a rotating rotor. A mechanical load is coupled to the shaft; the stator sees the same torque but in an opposite direction to the shaft torque. The stator frame must be bolted down to the floor; otherwise the stator would roll on the floor.

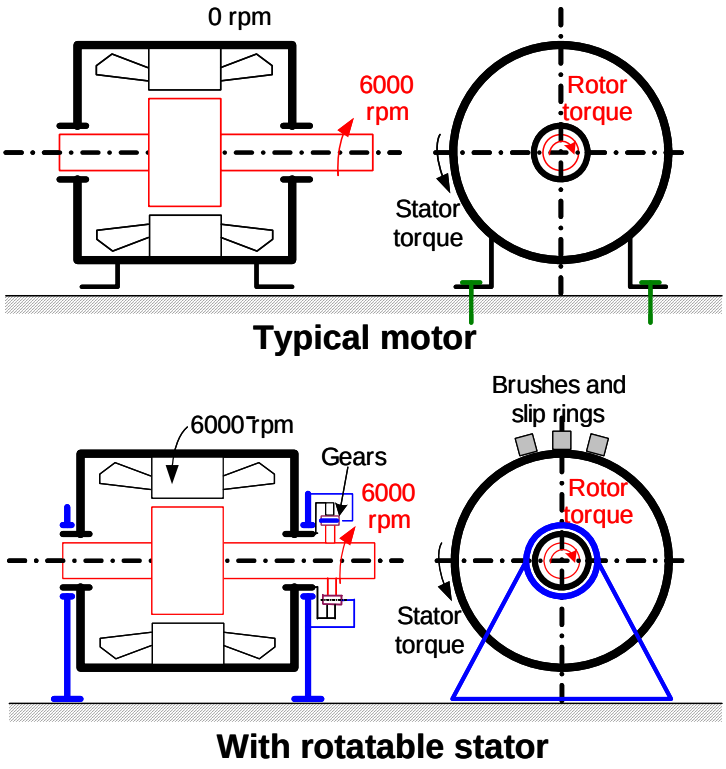

Fig. 1. Typical motor and a motor with rotatable stator.

The lower sketch in Fig. 1 shows that if the stator is allowed to rotate freely through the addition of more bearings and slip rings are used for energizing the stator windings, the stator will rotate in a direction opposite to the rotor. If a gear set is coupled between the stator and the rotor shaft, the direction of the stator torque will change and will be the same as the shaft rotating direction, resulting in the amplification of the shaft torque output. The amplification ratio depends on the gear ratio.

With this understanding of the uncluttered rotor for brushless energy feeding and the use of the rotating stator (or rotating armature, to be exact) for torque amplification, the ORNL CVT technique is discussed.

Figure 2 shows a sketch of the axial-gap CVT machine. As planetary gears are used in many leading hybrid vehicles, the sample CVT machine is connected to a planetary gear. The radial-gap CVT sketch used in the calculations for this report is not shown because it has export control restrictions.

Although some existing hybrid vehicles might use more than one set of planetary gears, Fig. 3 illustrates the operation principle with an example of one planetary gear set. If the uncluttered rotor is coupled to the sun gear that rotates in a given direction, then assuming the planetary gear is not rotating (i.e., the engine is not running), the ring gear will be driven to rotate in an opposite direction. The output torque of the ring gear can be increased according to the gear ratio when the sun gear runs faster than the ring gear. In our sample simulation, the ring gear is coupled to the PM rotor.

Inside the bore of the wound stator are the PM rotor, uncluttered rotor, and exciter coils. The interior PM (IPM) rotor interacts with the stator currents from its outer periphery and interacts with the uncluttered rotor from its inner periphery. The exciter core is stationary. Therefore, it does not see the centrifugal

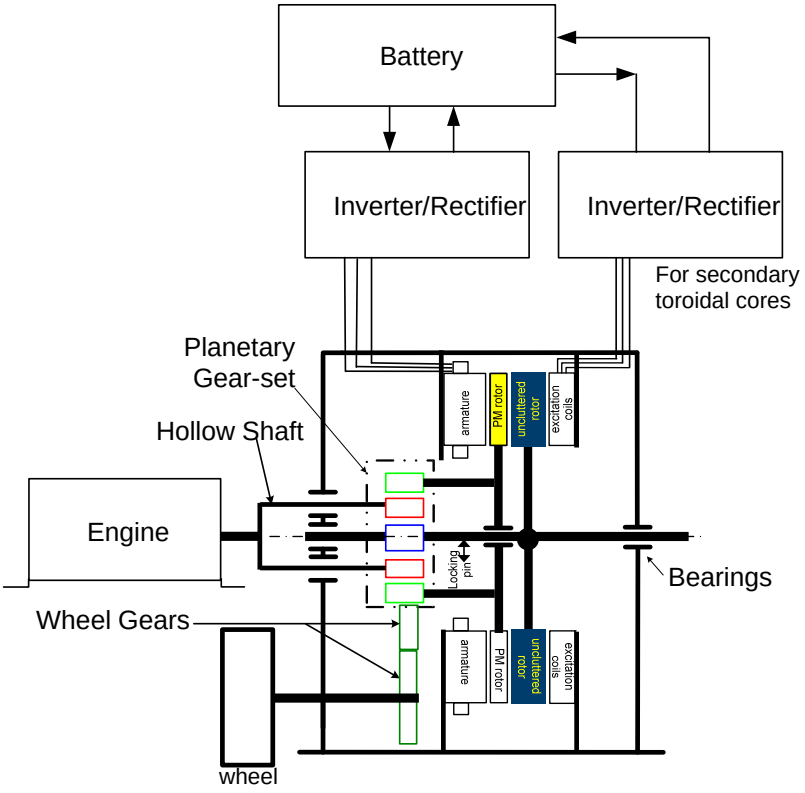

Fig. 2. Sketch of an axial-gap sample CVT machine in a vehicle.

force; higher-saturation-level, high-frequency compressed powder material should be investigated further for this application.

There are many possible designs for CVTs using the uncluttered rotor concept. The two major groups are the radial-gap and the axial-gap configurations. Because of the long computation time required for a 3D model, the computations in this study are focused on a radial-gap model to see what can be gained and to obtain scaling equations for other models with different dimensions.

Beginning with a baseline design for comparison purposes, a Prius IPM motor stator of 3.4-in. stator core length was used as a starting point for the study. It determines the dimensional boundary for this sample study. The rotor outer diameter of the Prius motor remained unchanged, but the rotor lamination slot configuration was changed for the CVT assembly. The center portion of the IPM rotor was modified to have an additional torque-producing air gap for the uncluttered rotor and to accommodate its stationary exciter core.

Unlike a 2D finite element simulation traditionally used in motor design, which takes only minutes to solve, a 3D model such as the sample CVT can take hours (or days) to solve one simulation. The simulations to adequately assess the operation of this concept were extremely computation- intensive and time-consuming.

The comparison of component weights between the Prius motor and the ORNL CVT machine is shown in Table 1. The ratio of total weights between the ORNL CVT machine and the baseline (Prius) motor is 94.8/82.5 = 1.149 = 1.15

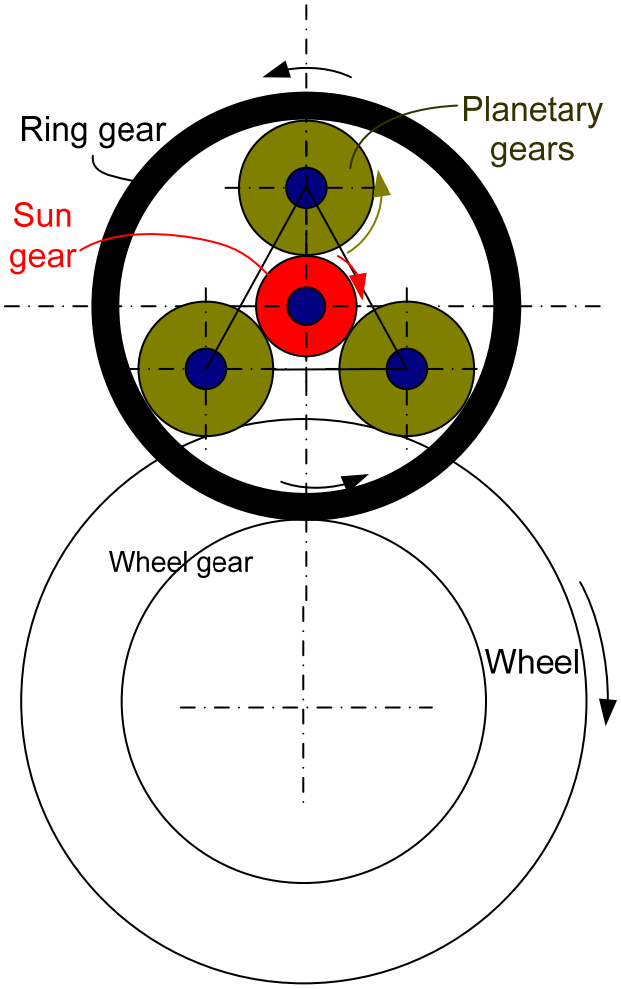

Fig. 3. Planetary gear in a hybrid vehicle.

Table 1. Comparison of component weights between baseline (Prius) and ORNL CVT machines

Components	Prius (lb)	ORNL CVT (lb)
Stator core	42.2	42.2
Stator copper	15.0	15.0
PM core	22.5	6.1
PM	2.8	2.6
Uncluttered rotor and excitation	0	28.9
Total	82.5	94.8

Uncluttered rotor torque estimation

The ratio of the uncluttered rotor torque from interacting with the PM rotor and the stator torque from interacting with the PM rotor can be derived from the law of physics; torque is the product of force and the torque arm length, and the force is derived from the product of current, turns, and conductor length.

$$\frac{(Uncluttered\ rotor\ torque)}{(Stator\ torque)} \approx \left(\frac{Number\ of\ equivalent\ exciter\ slots}{Number\ of\ stator\ slots}\right) \cdot \left(\frac{Excitor\ slot\ length}{Stator\ slot\ length}\right) \cdot \left(\frac{Exciter\ diameter}{Stator\ bore}\right) \tag{1}$$

Substituting the numbers into Eq. (1) gives the torque ratio of

$$\frac{(Uncluttered\ rotor\ torque)}{(Stator\ torque)} \approx \left(\frac{2}{48}\right) \cdot \left(\frac{11"}{3.4"}\right) \cdot \left(\frac{3.98}{6.375}\right) = 0.084 \tag{2}$$

When the stator produces 401 Nm of torque, with the same ampere-turns per equivalent exciter slot the uncluttered rotor produces

$$(Uncluttered\ rotortorque) \approx 0.084 \cdot 401Nm = 33.7Nm. \tag{3}$$

Equation (1) can be used as a coarse scaling tool for new configurations with different dimensions.

Figure 4 shows the plot of the 3D finite element uncluttered-rotor torque versus the phase angle of the phase-1 exciter coil; under the same number of exciter-slot ampere turns as that of the stator slot, the peak uncluttered rotor torque is –36.7 Nm. The 36.7 magnitude is not far away from the 33.7 Nm magnitude predicted by the coarse scaling Eq. (3).

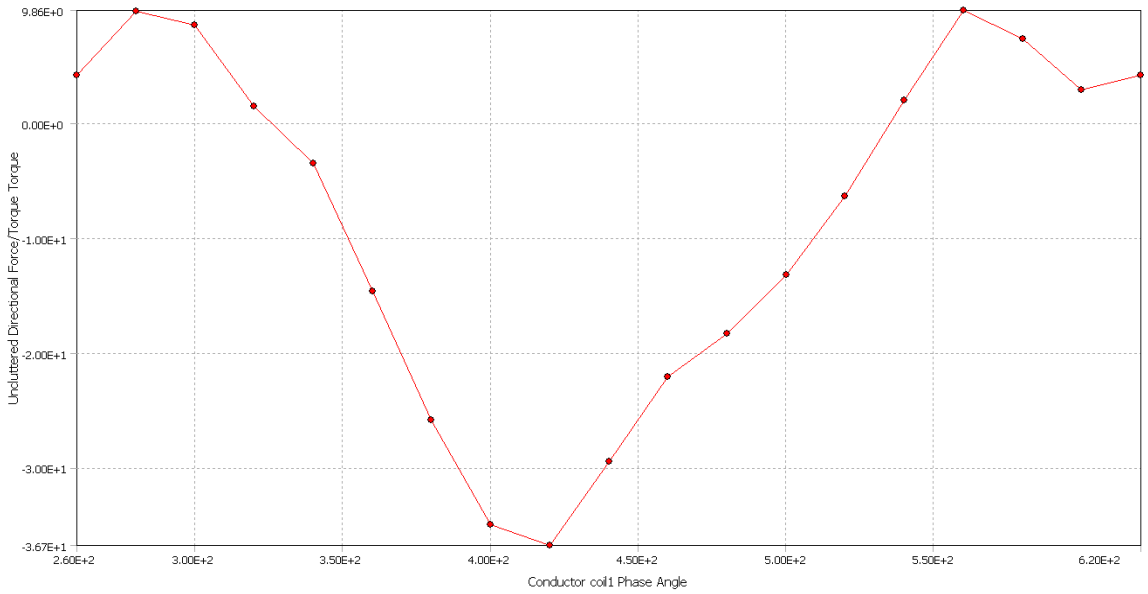

Fig. 4. Uncluttered rotor torque versus conductor coil-1 phase angle.

The peak torque produced by the interaction between the PM rotor and the wound stator core is 401 Nm, as shown in Fig. 5 for the torque versus conductor-a phase angle.

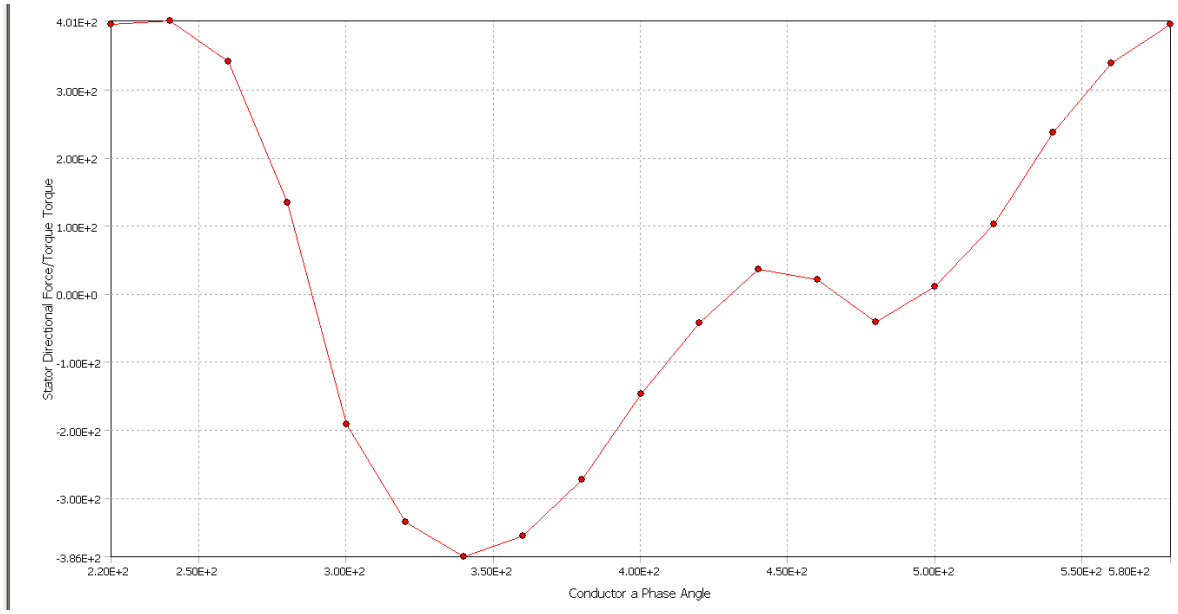

Fig. 5. Torque produced by stator wound core and PM rotor versus conductor-a phase angle.

Impacts of the uncluttered rotor torque on the CVT

The impact of the 36.7 Nm torque on the wheel torque from the CVT is quite remarkable. Assume the gear ratio between the ring gear and the sun gear equals the ratio of the permissible speed limits of the uncluttered rotor and the PM rotor. In our sample case, this ratio is (14,000 rpm/6,000 rpm) = 2.33. The additional torque to the wheel is the sum of the following torques:

1. The torque (36.7 Nm) produced by the interaction between the uncluttered rotor and the PM rotor.
2. The counter torque of the uncluttered rotor received from the PM rotor is a negative 36.7 Nm; this –36.7 Nm torque drives the sun gear and subsequently transfers to the ring gear and drives the wheel. Taking the gear ratio of 2.33 and the torque direction change into consideration, the effect to the wheel from this counter torque is 36.7 • 2.33=85.5Nm.
3. The total additional torque produced by both the torque of (1) and the effective counter torque of (2) is 36.7 + 85.5 = 122.2Nm.

The CVT power output as compared with that of the baseline (Prius) motor is (122.2 + 401) / 401 = 1.30. A 30% increase of torque (or power) is obtained.

Conclusions

- The 3D simulations confirm that the ORNL uncluttered-rotor CVT concept can be applied to a commercially available IPM machine.
- During simulations the center portion of the PM rotor of the IPM machine was modified to accommodate the uncluttered rotor and its excitation. The modified machine contour diameter and length were confined to the original IPM machine.
- At 287 A of root mean square phase current (or 406 A current amplitude), the stator gives 401 Nm maximum torque and the uncluttered rotor gives 36 Nm maximum torque.
- From the mechanical stress standpoint, the IPM rotor is allowed to run at 6,000 rpm while the uncluttered rotor with a smaller diameter is allowed to run up to 14,000 rpm.

- The uncluttered rotor can be used to drive the sun gear of the planetary gear set. Its 36 Nm torque is amplified to (14,000/6,000) • 36 = 84 Nm at the ring gear that drives the wheel.
- The machine power rating is thus increased to (401 + 36 + 84) / 401 = 1.30 times without increasing the overall contour size.
- As compared with the Prius motor, the ORNL CVT has a 30% torque (or rating) increase with a total weight increase of only 15%.
- This 30% power gain takes advantage of the high-speed capability of the small-diameter uncluttered rotor and the existing planetary gear for converting the counter torque of the uncluttered rotor to drive the wheel.
- The 30% power gain is produced by two exciter coils, compared with the 48 stator coils in the original IPM machine. Each of the two exciter coils has about the same ampere-turn rating as each of the 48 stator coils. The copper loss of the two exciter coils is about 2/48 = 4.2% of the 48 stator coils. From the copper loss standpoint, the machine has 4.2% additional copper loss to gain an additional 30% power output.
- The additional core loss has two contradicting factors. First, the loss per volume would be higher as a result of the higher speed of the uncluttered rotor. Second, the volumes of the exciter and uncluttered rotor are small. Special attention must be paid to the core loss reduction for the uncluttered rotor (e.g., using thin and low-loss laminations) and the exciter core (e.g., using low-loss compressed powder with 1.5 Tesla saturation-level materials). However, the core-loss reductions need to be further investigated.
- The scaling equations provide a tool for other machine configurations.
- This uncluttered rotor concept opens a door for various brushless electric machine improvements.
- A prototype machine has not yet been built. It should be the next step for further research on the uncluttered rotor concept.

Publications

J. Hsu, "Hybrid-secondary uncluttered induction (HSUI) machine," *IEEE Transactions on Energy Conversion* **16**(2), ITCNE4, (ISSN 0885-8969), 192–197 (June 2001).

J. Hsu, "Closure on hybrid-secondary-uncluttered induction (HSUI) machine," *IEEE Transactions on Energy Conversion* **17**(1), ITCNE4, (ISSN 0885-8969), 150 (March 2002).

References

1. J. Perahia, "Discussion of hybrid-secondary-uncluttered induction (HSUI) machine," *IEEE Transactions on Energy Conversion* 17(1), ITCNE4, (ISSN 0885-8969), 150 (March 2002).

Patents

1. John Hsu, "Hybrid Secondary Uncluttered Induction Machine," U.S. Patent No. 6,310,417, October 30, 2001.
2. John Hsu, "Simplified Hybrid-Secondary Uncluttered Machine and Method," U.S. Patent 6,891,301, May 10, 2005.
3. John Hsu, "Hybrid-Secondary Uncluttered Permanent Magnet Machine and Method," U.S. Patent 6,977,454, December 20, 2005.
4. John Hsu, "Electric Machine for Hybrid Motor Vehicle," U.S. Patent 7,270,203, September 18, 2007.
5. John Hsu, "Radial Gap Hybrid Secondary Uncluttered Permanent Magnet Electric Machines," Invention Disclosure 1934, May 7, 2007.

3.2 Axially Excited Electro-Magnetic Synchronous Motor

Principal Investigator: C. W. Ayers
Oak Ridge National Laboratory
National Transportation Research Center
2360 Cherahala Boulevard
Knoxville, TN 37932
Voice: 865-946-1342; Fax: 865-946-1262; E-mail: ayerscw @ornl.gov

DOE Technology Development Manager: Susan A. Rogers
Voice: 202-586-8997; Fax: 202-586-1600; E-mail: Susan.Rogers@ee.doe.gov

ORNL Program Manager: Mitch Olszewski
Voice: 865-946-1350; Fax: 865-946-1262; E-mail: olszewskim@ornl.gov

---

Objectives

- Produce a reasonably detailed design of an axially excited electromagnetic synchronous (AEEMS) motor, which is a synchronous high-torque motor using no permanent magnet (PM) material.
- Use finite element magnetics modeling to optimize the design in order to provide a reasonable estimate of size and weight.
- Determine the feasibility of the concept for lowering manufacturing costs owing to the rotor's simplicity and the lack of PM materials.
- Perform a cost analysis to determine if the concept results in a lower-cost machine compared with the Prius motor.

Approach

This project proposes a mechanical design for the rotor and axial excitation stator, expected to work in conjunction with a conventional radial-gap stator. The concept is called the AEEMS motor. This design focuses on a high-speed rotor capability, optimization of the flux paths for the magnetics in the axial stator and the rotor, and minimization of weight and added materials.

Magnetics finite element analysis (FEA) modeling was performed for the rotor and axially excited stator based on the mechanical design, and iterations between the two were performed throughout the design and modeling stages to improve the design. Evaluating the three-dimensional flux paths for this motor/rotor design was the main effort required for the magnetics modeling. The software used for this effort was ProEngineer Mechanica (mechanical and thermal FEA) and Ansys EMAG magnetics software (magnetic FEA).

Major Accomplishments

- The mechanical stator and rotor design has been completed to provide a basic model for the FEA of the magnetic performance of the motor. The design was based on a basic stator configuration and size such as is used in the Prius drive. A unique rotor configuration was developed along with axial excitation poles to magnetically excite the rotor.
- The stator design, which was originally believed to follow a conventional philosophy, evolved during the project and resulted in a different lamination structure that enhances the magnetic performance of the motor. The overall geometry of the stator is essentially the same, but the laminations are different.
- FEA modeling has been performed on the basic motor design, providing data that were fed back into the mechanical design.

- Multiple iterations were made in the rotor and stator designs, with FEA model results continually providing insight leading to mechanical changes and performance improvements.
- A feasible design has been shown with estimates of a specific power = 1 kW/kg and a volumetric power density = 5 kW/L.

Future Direction

This project combined technologies developed at ORNL utilizing brushless field excitation with a novel stator design from a FY 2007 project with the University of Wisconsin. Combining these technologies shows promise in moving toward the 2015 motor targets. This project accomplished the goal of ascertaining potential benefits from a motor using external field excitation without a PM rotor.

The decision has been made not to continue this specific project into FY 2009. In an effort to maximize resources, the lessons learned from this effort are being carried forward and consolidated into another FY 2009 project that involves similar concepts and builds upon this work.

Technical Discussion

This concept is a motor that is expected to be lower in cost than a PM motor, with a higher speed capability and higher power density. Rotor manufacturing will be simplified because no PM installation is required. Simplified manufacturing and changes in some materials produce the lower cost.

Inherent in this motor design is the natural ability to field weaken as speed increases as a result of the full control capability of the electromagnetic excitation coils used for rotor magnetization. Since the rotor can be naturally "weakened" as speed increases, core losses in the rotor will be much lower than in PM motors. This reduction in core losses in the rotor increases the efficiency of the inverter/motor system over the efficiency of a conventional inverter/PM motor system.

This design will produce a motor that provides traction motor functions for hybrid electric vehicles with a higher power density. Along with this performance improvement, a more robust and lower-cost motor design is expected. This design also has no dependence on rare earth materials/magnets with their associated cost, availability, temperature, and performance issues.

The design is based on a Prius-size core for convenience of comparison. The tradeoff between adding copper excitation coils and steel axial excitors and deleting the magnet material is estimated to result in a cost reduction. Total motor cost can be estimated based on comparisons with Prius and Camry motor construction. It is possible that some savings in manufacturing and assembly might occur in addition. Steel laminations for the stator can be made from radial subsections used to make up the whole circular stator core, instead of from one large circular stamping with a lot of waste area. The rotor is not expected to use laminations. The stator segments will be smaller and simpler and have more efficient punchings without the associated material losses inherent in single-piece circular punchings. See the Cost Analysis section of this report for cost comparison details.

The AEEMS motor concept uses a rotor that contains no PM material but provides magnetic flux paths axially excited by electromagnetic poles on the ends of the motor. To accomplish this excitation, axial excitors are required. These add iron and copper to the motor, adding weight and volume. These additions, though, are offset by removal of the expensive PM material from the design.

Figure 1 shows a cutaway of the motor concept with copper windings removed to allow the main components to be viewed. The rotor shaft and the trapezoidal blue components in the center make up the rotating portion of the motor. The large circular components wrapping around the motor are the axial excitors that provide magnetic flux in the rotor and flux communication to the stator. There is an axial air

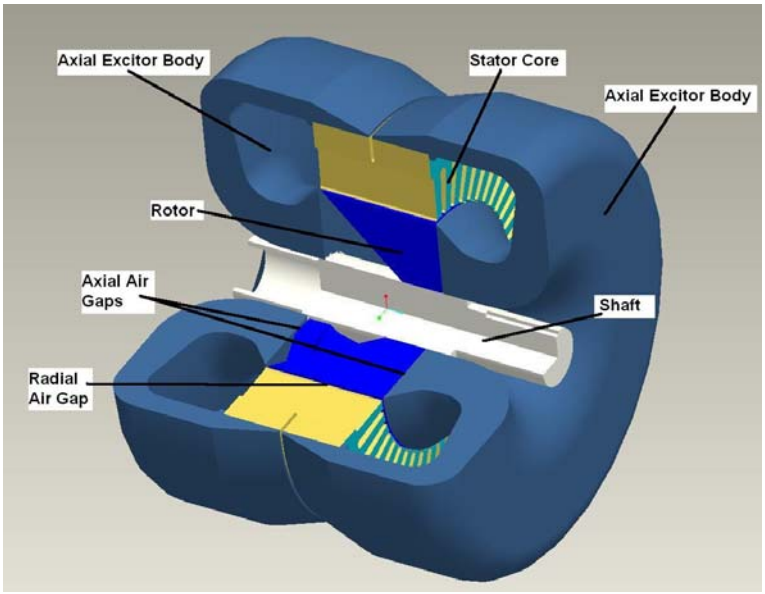

Fig. 1. AEEMS prototype design; 3D ProEngineer model used for FEA modeling.

gap between the flared axial excitor pole faces and the rotor axial face (a brushless design), and there is also the conventional radial air gap between the rotor circumference and the stator teeth.

Figure 2 is an exploded view showing the parts of the assembly opened up to provide more details of the design of the motor. The two rotor halves interleave together, and air gaps between all portions provide a magnetic break between the two sections. One rotor will have a positive flux orientation relative to the stator, and the other rotor half will have a negative flux relative to the stator. The axial excitors provide this flux with coils wound around the yoke adjacent to the shaft bearings. The two coils on opposite ends of the motor will have current flowing in opposite directions to provide the positive and negative rotor pole orientations.

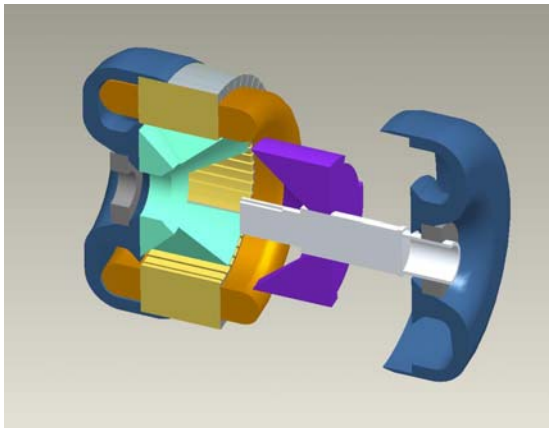

Fig. 2. Exploded view of the AEEMS motor showing subcomponents.

The stator design was originally intended to be a conventionally laminated stator with laminations similar to those in the Prius stator. During the development of the concept, it became clear that a different type of stator construction would be necessary. The new stator concept contains lamination punchings that are much simpler in shape and can be made with reduced punching waste. The simpler punchings come with a slightly more complex assembly requirement. This arrangement is required to promote magnetic flux in the correct directions in the stator, providing the lowest resistance to magnetic flux. The stator windings

are conventional, but the new arrangement of the laminations is required to handle the flux from the axial excitor magnetic field.

Note that in Fig. 3, the rectangular punchings are arranged to make up the new stator concept. In this prototype photo, the angle between segments is created by inserting an extra small tab of lamination in the yoke of the stack. A more developed prototype may use a wedge of lamination placed between the segments in the center of the yoke portion. This stator design essentially requires three different lengths of punchings, all the same width (essentially zero waste).

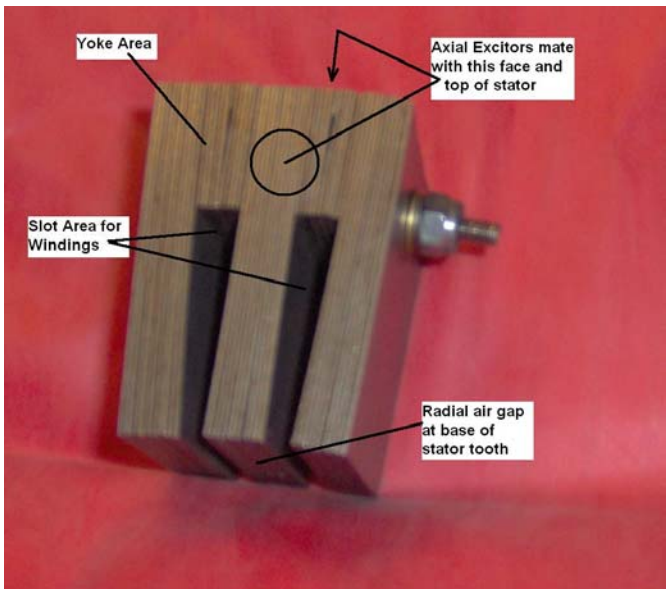

Fig. 3. Photo showing two slots of a prototype of the AEEMS stator lamination concept.

A ProEngineer model was made to show the construction with more of the detail that would probably be used in an actual prototype. The prototype in Fig. 3 was a quick demonstration model put together with simple pieces. Figure 4 shows a quarter section of the stator design from a ProEngineer model. This lamination arrangement allows magnetic flux to flow freely in the axial direction, allowing the axial excitation design to function.

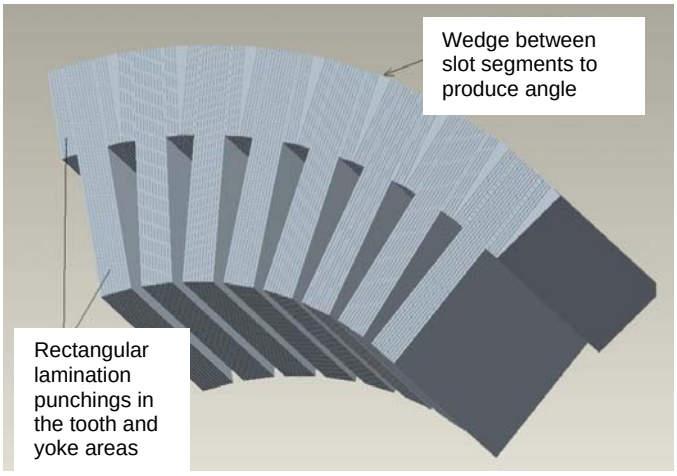

Fig. 4. Rectangular punching style stator construction for the AEEMS motor.
This concept requires a wedge-shaped piece between each stator segment.

Finite element analysis results

Ansys EMAG software was used to model the magnetic performance of the motor components. Small slices were first used, 22.5° segments, to speed up the solution time and aid in achieving a quick understanding of the basic magnetic behavior of the design. As the design became better understood magnetically, the model was made more complex, and eventually a 360° full model was used to perform the magnetic solutions. The full model results provided the direction for mechanical design changes.

Figure 5 contains a 90° segment from early in the development stage, showing how the magnetic flux lines behave in the material. At this stage, fundamental concepts were being explored; sources of leakage were being searched for and mitigated by changes in the mechanical design (such as the circumferential slot shown, which was determined to be unnecessary for flux control).

The colored arrows show flux line direction, and the yellow and red lines depict areas nearing flux saturation. These areas can then be modified to reduce the saturation tendency by placing material where it is needed or to remove material, and weight where it is *not* needed when flux density is very low.

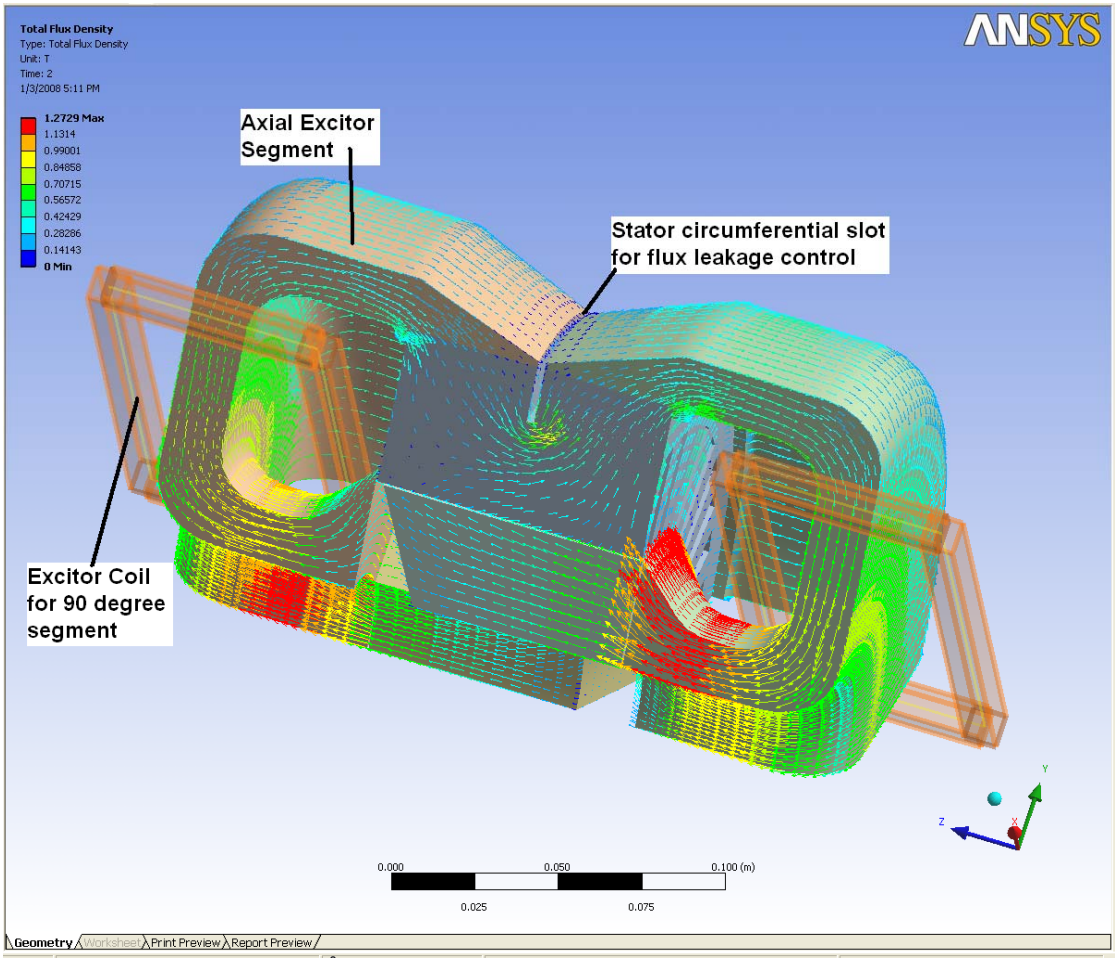

Fig. 5. A 90° model segment from ProEngineer software used with Ansys EMAG software to evaluate magnetic performance.

Figure 6 shows the view of flux lines in the full 360° motor model. The locked rotor torque estimated from this configuration was 235 N m. The motor design provides flux paths in the conventional 2-dimensional plane of the motor and in the third dimension parallel to the shaft. The design allows the flux to go axially (i.e., out of the page) through the pole side faces, around through the excitor sections, and into the stator edge and outer circumference.

The design uses reluctance torque, combining a mix of two different reluctance paths— one in the plane of the motor and another in the axial direction. It is believed that these two separate paths can be further studied and developed to produce an even higher torque design in future work.

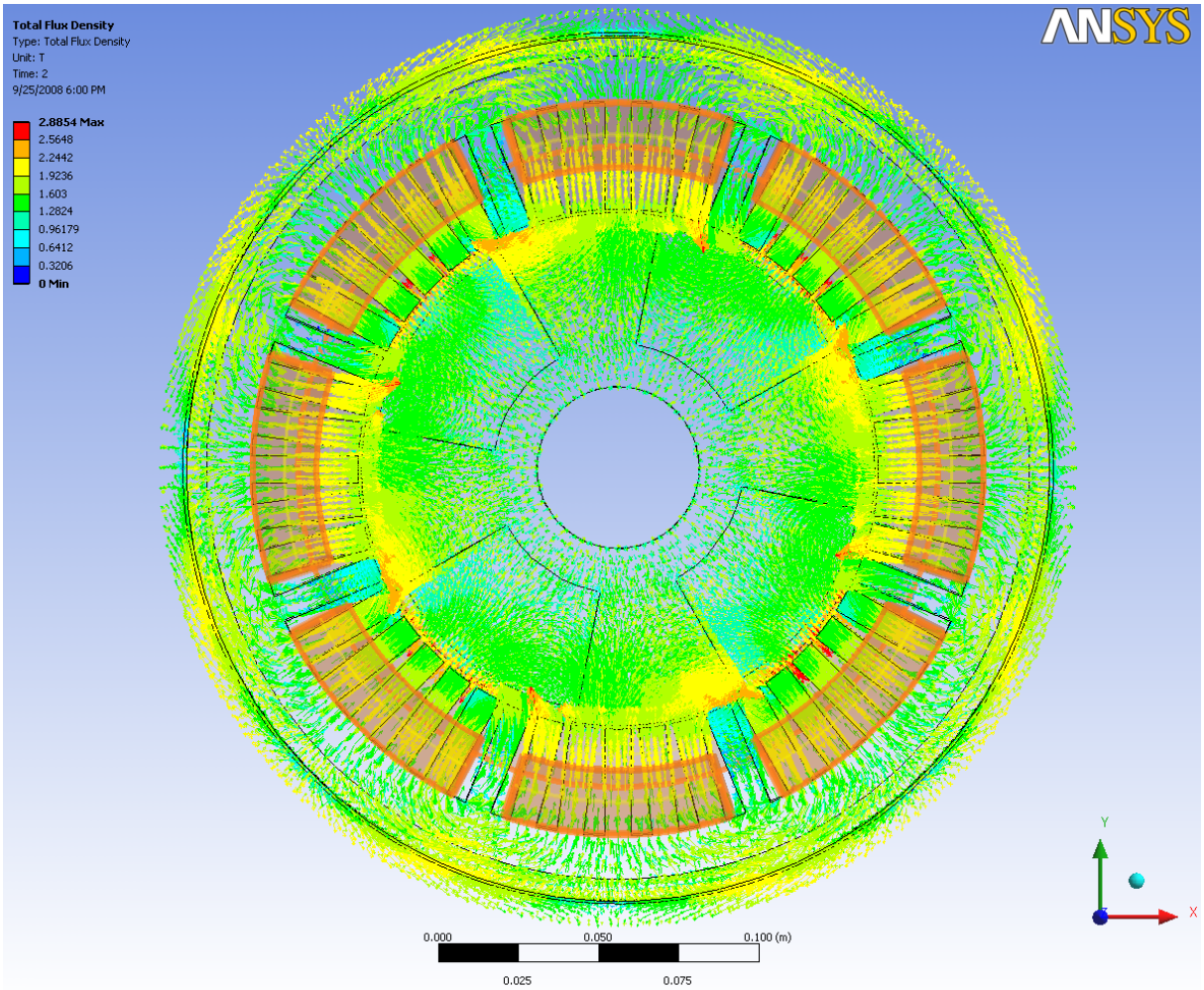

Fig. 6. Model results from Ansys EMAG for a 360° slice of the motor.

Figure 7 shows the 360° model from a side view (with one excitor removed), which gives an indication of the complexity of the 3-dimensional flux in this type of motor. Torque results from various EMAG solver runs are shown in the plot in Fig. 8. After a reasonable model was found with good torque performance, multiple runs were made while the rotor angle was changed to search for the best rotor position for peak torque. The peak torque was seen in a couple of very similar geometries in the "4/24 data" and the "Misc at tdc+57", shown in Fig. 8.

Some areas of leakage between rotor halves were reduced, and a configuration with increased radial air gap area was analyzed to produce the final improvements in the design so as to achieve 235 N m peak torque. Note that this is the highest torque possible; further study is very likely to increase this number to even better torque levels. This value was determined to be a good stopping point for the feasibility study based on findings and budget.

The intent of the feasibility study has been met, with positive results.

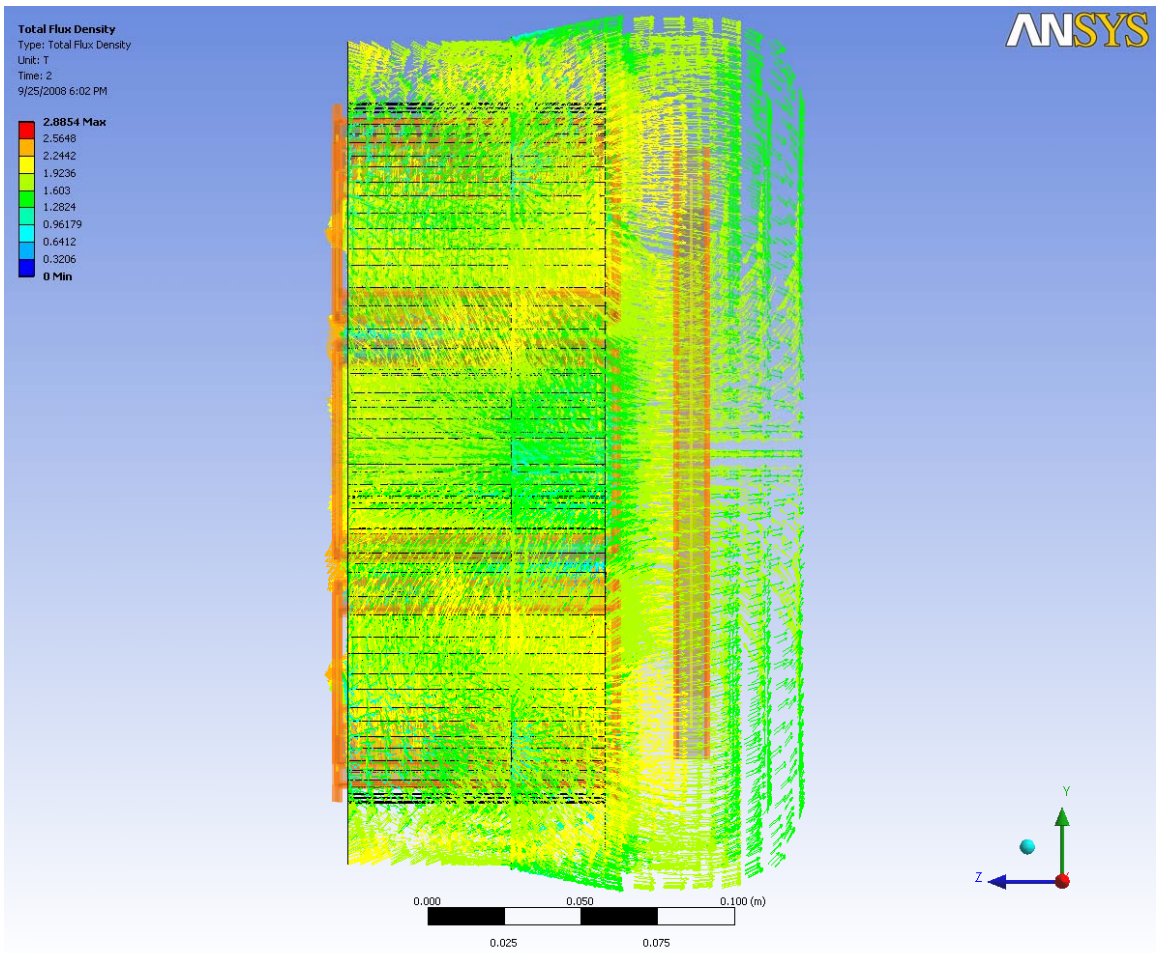

Fig. 7. Side view of the 360° EMAG model.

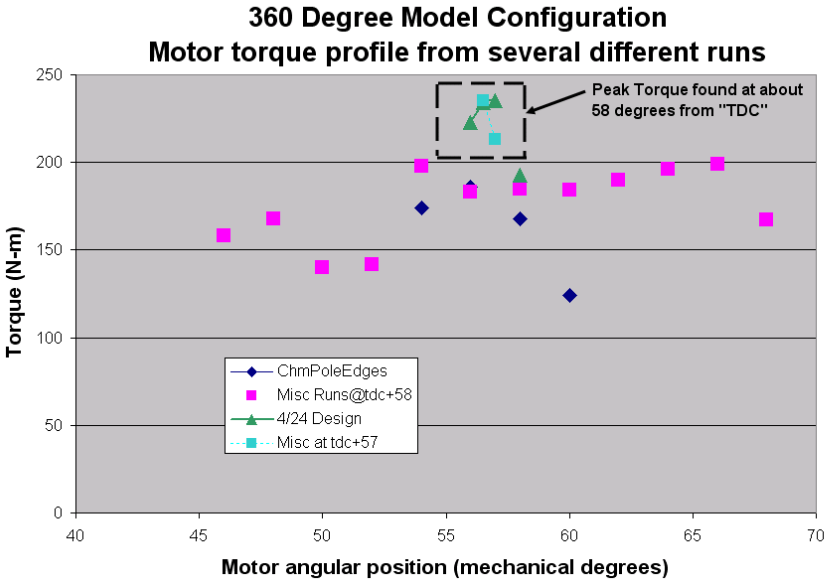

Fig. 8. Plot showing torque achieved with various motor geometries versus motor angular position.

Cost analysis comparison of this motor design with the Toyota Prius design

The approximate cost for finished neodymium iron magnets (simple rectangular shape) is about $60/kg (cost information furnished by Arnold Magnetics in August 2008).

Prius PM material volume is estimated to be V = 11 in^3. This was calculated from the Prius magnet cross-section dimensions and the lamination stack length of 3.29 in. Using this volume, the mass was calculated for the PM material:

$$\text{Mass of PM } (11\ in^3) \times (0.3\ lbm/in^3) = 3.3\ lbm \text{ (equals } 1.5\ kg)$$

Based on this calculation, the approximate cost of the PM in the Prius motor = 1.5 kg · $60/kg = $90.

Copper costs have changed rapidly during the past year, so a few sources were checked to estimate the present raw copper cost. As of about August 22, 2008, costs were as follows:

Wikipedia	$2.80 / lbm
New York Futures	$3.36 / lbm
AllBusiness.com	$3.50 / lbm → $7.70 / kg

The $49 cost estimate decrease is mainly due to the removal of PM material from the motor design. In addition to the estimation in Table 1, the dollar amount needs to be normalized to the projected power density of the AEEMS motor compared with the Prius power density.

Power estimates

AEEMS power is calculated to be 61.5 kW peak with an assumed base speed of 2,500 rpm (this number needs to be validated by further study). The volume of the model, created in ProEngineer Wildfire 3D

modeling software, was found to be 12.0 L. The mass (also from the ProEngineer software model) was found to be 63 kg.

Prius specific power:	1.1 kW/kg
Prius power density:	3.3 kW/liter
AEEMS specific power:	0.97 kW/kg
AEEMS power density:	5.1 kW/liter

The costs in Table 1 need to be normalized to the differences in specific power and power density found in the two motor designs. In other words, the cost reduction shown in Table 1 for the AEEMS motor needs to be lowered according to the lower specific power but increased in light of the higher power density.

Based on specific power:

$$\text{AEEMS cost} = \frac{0.97}{1.1} \times -\$49 = -\$43$$

Table 1. Material additions/subtractions from the Prius motor design

Item description	Added to	Subtracted from	Cost ($)
Stator iron	0	0	+ $ 0
Excitor iron	24.8 kg		$ 25
Excitor copper	2.1 kg		+ $ 16
Permanent magnet material			– $ 90
AEEMS cost compared with Prius		7.3 kg	– $ 49

Based on power density:

$$\text{AEEMS cost} = \frac{5.1}{3.3} \times -\$49 = -\$\ 75$$

Based on these numbers, the AEEMS estimated cost *reduction* relating to materials would be an average of $59.

Manufacturing cost considerations

The AEEMS stator lamination design provides for a very simple and cost-effective punching with essentially zero waste. This compares with the type of standard punching used in conventional motor stators, such as those in the Prius, which have a significant amount of unavoidable waste.

While the stator punchings may provide some amount of savings in manufacturing material, the difference in the AEEMS stator assembly procedure will probably show a small increase in effort that would offset the savings in lamination waste. The actual increase/decrease in cost for the stator construction will require further study.

Stator wiring will be fairly conventional, so stator wiring and assembly costs will be basically unchanged. The added magnetic excitors will require winding, but the windings will probably be done as a simple spun core and will be inexpensive to fabricate and install.

The rotor, by specific design, will have no PMs; therefore, the rotor fabrication and assembly will be very simple, with similar or slightly lower cost and effort compared with an induction motor. Any cost savings in this area are likely to offset the slight costs associated with the excitor winding and assembly.

Overall, at *this stage* of the concept study, the manufacturing costs seem to be approximately equal between a Prius or Camry comparison motor and the AEEMS concept design. No large differences are anticipated.

Conclusion

This feasibility study has shown that the AEEMS design can produce significant torque, up to 235 N m, for this size of stator and rotor (based on the 2004 Prius size). The information gained this year indicates the design is a feasible concept and could be further refined and made more complete with future work. A first-order cost analysis based on comparison with a known motor, the Prius PM traction motor, has shown that it may be possible to produce the AEEMS motor at slightly less cost. The important comparison is that this design is slightly lower in cost and requires no PM material, thus fulfilling a need for an alternative motor design in addition to common designs such as induction and PM motors.

The motor configuration studied in this year's effort shows these estimated results:

Locked rotor torque	235 N-m
Total mass	63 kg
Total swept volume	12 liter
Estimated power (base speed 2,500 rpm)	61 kW peak
Specific power	0.97 kW/kg
Volumetric power density	5.1 kW/liter

Further development is required to determine the potential efficiency, nominal base speed capability, and rotor speed capability of the motor.

3.3 Application of Concentrated Windings to Electric Motors without Surface-Mounted PMs

Co-Investigators: John W. McKeever and Pedro J. Otaduy
Oak Ridge National Laboratory
National Transportation Research Center
2360 Cherahala Boulevard
Knoxville, TN 37932
Voice: 865-946-1316; Fax: 865-946-1262; E-mail: mckeeverjw@ornl.gov

DOE Technology Development Manager: Susan A. Rogers
Voice: 202-586-8997; Fax: 202-586-1600; E-mail: Susan.Rogers@ee.doe.gov

ORNL Program Manager: Mitch Olszewski
Voice: 865-946-1350; Fax: 865-946-1262; E-mail: olszewskim@ornl.gov

---

Objectives

- To determine if electric motor configurations using interior permanent magnets (IPMs) can benefit from using fractional-slot concentrated windings (FSCW) instead of distributed windings in electric vehicle (EV) or hybrid electric vehicle (HEV) traction drives.

Approach

Task 1. Redesign a (computer model of a) commercially available baseline IPM motor by replacing distributed windings with concentrated windings.

- Four concentrated winding configurations with 8 poles were chosen because they were compatible with the baseline IPM, which had 8 magnets (4 pole pairs). The configurations, expressed as slots/poles, were 9/8, 12/8, 24/8, and 48/8; they have fundamental harmonic winding factors of 0.945, 0.866, 0.500, and 0.256, respectively.
- These configurations were modeled in SPEED and their performance parameters and torque ripple examined to determine if any of them had potential to be an HEV traction drive.

Task 2. Craft an algorithm that represents saturation in a lumped parameter model of an IPM motor with sufficient accuracy to provide insight into the effect of saturation on IPM motor performance.

- The purpose of this task was to provide insight about and quantify the effect of magnetic saturation on inductances, Lq and Ld, as the line current and motor speed change. Inductance relates the flux-links to current. Values of Lq and Ld change as the motor core becomes magnetically saturated during operation. Corrected values were needed to perform Task 4—a simulation of the motor traversing two standard driving schedules, the US06 and the Federal Urban Driving Schedule (FUDS)—to compute an average performance in terms of miles per gallon. The difficulty of creating a physics-based algorithm forced us to obtain our insight and inductance correction coefficients from SPEED's PC-BDC software, which applies finite element analysis (FEA) of the flux-links using its PC-FEA module as a function of speed and line current as the rotor turns. The ratio of the inductance computed by FEA to the inductance computed with saturation neglected defines the saturation correction coefficients used in Task 4.
- A script was written to obtain the saturation coefficient dependency on current and speed. The script queries the PC-BDC FEA software looping through ranges of motor speed, current, and control angle.

The control angle delivering the maximum efficiency was used to select the parameters needed for use in Task 4.

Task 3. Complete a performance analysis of 55-kW IPM motors with concentrated windings to identify a configuration that can meet FreedomCAR targets.

- Analysis of the 9/8 IPM with concentrated windings was completed and compared with a baseline IPM model having distributed windings.

Task 4. Determine the average efficiency (in mpg) for the 9/8 IPM with concentrated windings as it traverses US06 and FUDS driving schedules and compare it with the average efficiency (in mpg) for the baseline 48/8 IPM with distributed windings.

- Resurrected and updated ORNL's driving schedule simulation program, which is on a LabVIEW platform.
- Coordinated the results from Task 2 to make them compatible for use in the simulation program.
- Completed simulations of the US06 and FUDS driving schedules using models of the 9/8 IPM with concentrated windings and the 48/8 IPM baseline with distributed windings as traction drives, and compared their performance.

Major Accomplishments

- Compared with the 12/8, 24/8, and 48/8 adjusted to have the same number of coils per phase, the 9/8 IPM with FSCW was the only configuration with acceptable torque ripple of 8% at base speed; consequently, it was selected for further analysis.
- Saturated inductance correction coefficient tables were calculated for the 9/8 IPM with concentrated windings and for the baseline 48/8 IPM with distributed windings in preparation for the simulation of these motor models traversing the US06 and FUDS. The simulation was conducted as Task 4 using ORNL's driving simulation program.
- Detailed modeling of the 9/8 IPM with concentrated windings showed that
  - The number of turns per coil for maximum power is 11, up by 3 from the number used to compare torque ripple among the 8-pole configurations with concentrated windings.
  - Torque ripple is half that of the baseline IPM with distributed windings.
  - The base speed is 5,800 rpm, 2.3 times higher than the 2,500 rpm base speed of the baseline IPM with distributed windings.
  - At base speed, the power delivered to the shaft is 12.8% higher than that delivered by the baseline IPM.
  - The torque versus rpm performance curve extends over 6 times base speed, allowing the motor to deliver significant power at high speeds, characteristic of motors with concentrated windings.
  - In spite of 4% more bridge flux leakage, the efficiency at base speed is over 98%, 11.6 percentage points higher than that of the baseline IPM, because better copper use reduced current density in the stator wires by a factor of 3, from 32 to 11 A/mm^2.
  - Although the current density diminishes as the speed increases to 18,500 and 33,460 rpm, the efficiency drops from 98 to 86%—about the same as the baseline IPM at its 2500 rpm base speed—because of increasing eddy current and hysteresis losses in the core.
  - Compared with the baseline IPM with distributed windings, the $/kW, kW/kg, kW/L, and efficiency of the 9/8 motor with concentrated windings are better at speeds up to 18,500 rpm; but this edge is lost because of a 10 kW reduction in shaft power between 18,500 and 33,460 rpm.
  - Because concentrated windings make better use of copper, more copper was used; to offset the increased copper costs, the savings from simplified fabrication must be more than the 2% assumed in this study.

- Simulations of the US06 and FUDS cycles with the 9/8 IPM with concentrated windings and the baseline 48/8 IPM with distributed windings have been completed and show that the following:
  - If the gear ratio were increased 1.25× above the base gear ratio, from 4.114 to 5.145, the baseline IPM with distributed windings could meet US06 and FUDS cycle requirements with a maximum of 51.4 mpg and 72.8 mpg, respectively.
  - The US06 and FUDS requirements could be met by the 9/8 IPM with concentrated windings only after the gear ratio was increased 3.5× above the base gear ratio, from 4.114 to 14.399. This would achieve values of 50.13 mpg and 70.68 mpg, respectively, slightly below baseline values.
  - To fully negotiate the US06 and FUDS cycles, the IPM with concentrated windings had to be operated at speeds of up to 33,460 rpm, which means that the rotor would have to be specially reinforced and might not be feasible for these dimensions.
  - The gains in efficiency at base speed and half maximum speed for the 9/8 IPM with concentrated windings occur because of reduced copper losses but are overwhelmed by eddy current and hysteresis losses as the speed climbs to 33,460 rpm.
  - Eddy current losses in the magnets, were not included in this study but should be included in future calculations.

Future Direction

No additional work is planned. However, results of this study suggest that motor modeling should include calculation of magnet losses and that 9-slot, 8-pole or other IPM configurations with concentrated windings should be designed in concert with standard driving schedules to meet their requirements at reasonable motor rotor speeds without inordinately increasing the gear ratio.

Technical Discussion

Early motor development began with concentrated windings but changed to distributed windings because they produced sinusoidal back-emfs (electromotive forces). Concentrated windings have reawakened research interest for several reasons, including increased fault tolerance at higher operating speeds, reduction of the end turns, improved packing of wires in the stator slots, and reduced fabrication costs. This project focused on simulating different interior PM motor configurations using concentrated windings to assess their performance benefits.

Four slot/pole configurations with concentrated windings compatible with the baseline IPM 8-pole rotor are 9/8, 12/8, 24/8, and 48/8 in order of reducing winding factor. The four were modeled for comparison to have 32–33 turns per phase so that the 9/8 had 11 turns/coil and 3 coils/phase, the 12/8 had 8 turns/coil and 4 coils/phase, the 24/8 had 4 turns/coil and 8 coils/phase, and the 48/8 had 4 turns/coil and 8 coils/phase. Figure 1 compares the torque ripple of these four configurations at base speed.

The torque fluctuation of the 9-slot and 12-slot stators are similar, but the torque ripple is 3.5 times greater for the 12-slot stator. The 24- and 48-slot stators deliver much lower torque at base speed. The torque ripple for the 9/8, 12/8, 24/8, and 48/8 is 8.5%, 27.4%, 52.3%, and 218%, respectively, showing that the 9/8 configuration is closest to the FreedomCAR target for torque. For this reason it was selected for more detailed analysis.

A script was written to calculate the motor model's characteristic values of flux links and inductance, Ld and Lq, using the finite element capability of SPEED's PC-BDC module, which accounts for magnetic saturation. Calculations were performed over three loops: for speeds of 1,000 to 18,500 rpm in steps of 2,500 rpm, for ISP (the current set point) values from 10 to 400 A in steps of 50 A, and for advance control angles of 0 to 90 degrees in steps of 5°. An interesting feature of the 9/8 configuration is its ability to deliver power at speeds well above its base speed of 5,800 rpm. This is shown in Fig. 2, which summarizes the results obtained for torque, current, power, efficiency, and the advance angle that

produces maximum efficiency between 1,000 and 18,500 rpm. Figures 3a and 3b show the values of Ld, Lq, psiMd (PM drive flux-links), and efficiency as a function of advance angle for currents limited by the two extreme current set point values of ISP = 10 and ISP = 400, respectively. Information from plots like those in Fig. 3 characterizes core saturation, which relates values of Ld, Lq, and psiMd to current in the stator. It was necessary to complete these calculations to prepare for Task 4, which is to simulate the motor operating as a traction drive traversing standardized driving schedules. Plots like those in Fig. 3 are then summarized as shown in Fig. 4, which is a plot of values Ld, Lq, and psiMd as a function of the stator's ampere-turns, a form that may now be used by ORNL's driving schedule simulation program.

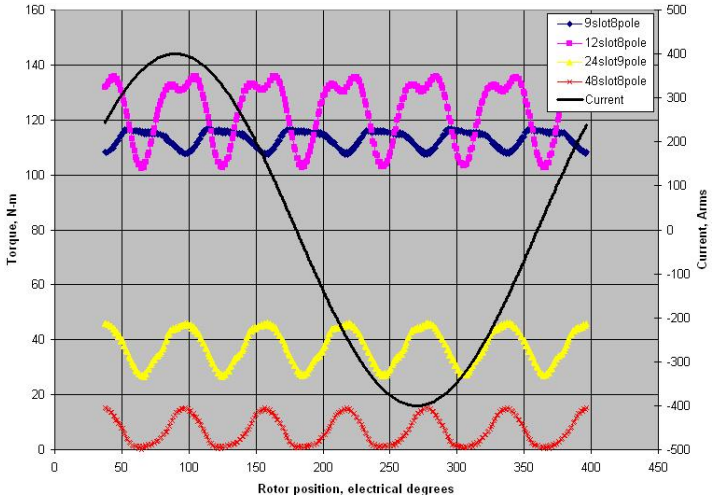

Fig. 1. Torque ripple for IPMs with 8-pole concentrated windings configured for 33 turns per phase.

The 9/8 configuration in Fig. 5 was initially ranged using smaller intervals of gamma in the computational loops of SPEED's PD-BDC (with the embedded PC-FEA module) to determine the number of turns per coil that would produce maximum shaft power. From Fig. 6, we see that the value of TC (turns per coil) should be 11 or 12. We chose TC=11.

The advance angle is the angle between the terminal voltage and the back-emf generated by the rotor, which coincides with the q-axis. To determine the base speed, the advance angle at which the motor delivers maximum power was determined first at each speed for which the corresponding torques and powers are shown in Fig. 7. The base speed, 5,800 rpm, was determined as the speed at which the torque starts to drop. The slope of the drop is much less than for the baseline IPM.

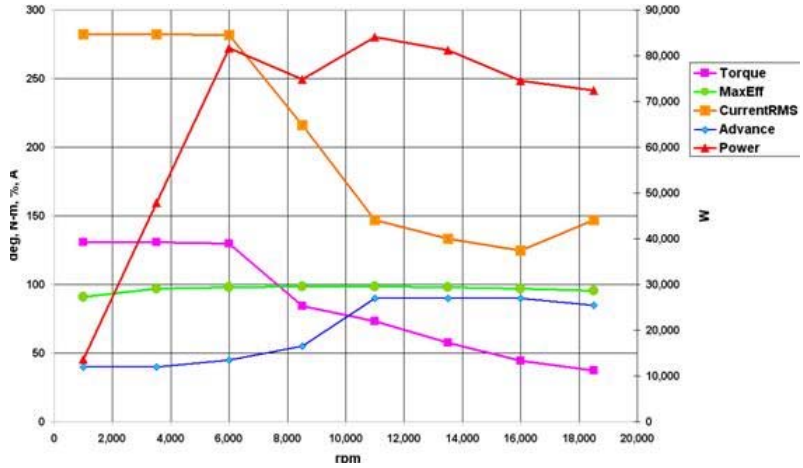

Fig. 2. Performance parameters to 18,500 rpm for 9-slot, 8-pole IPM with concentrated windings.

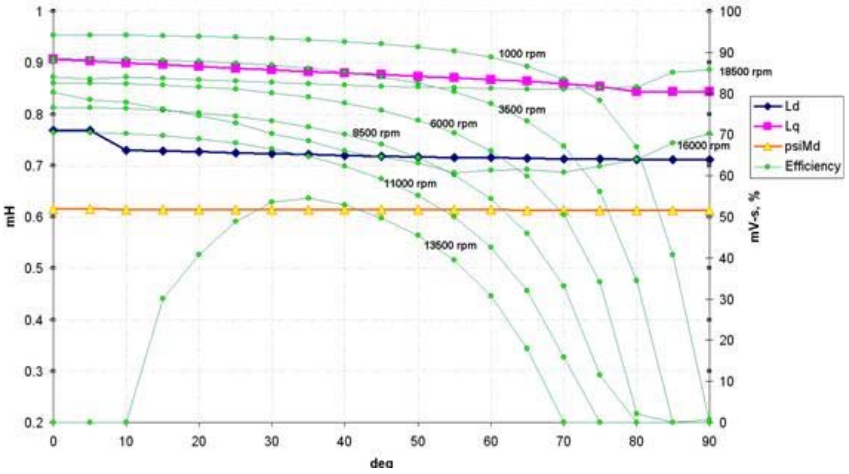

(a) Parameters as a function of advance angle for current controlled by a current set point, ISP=10.

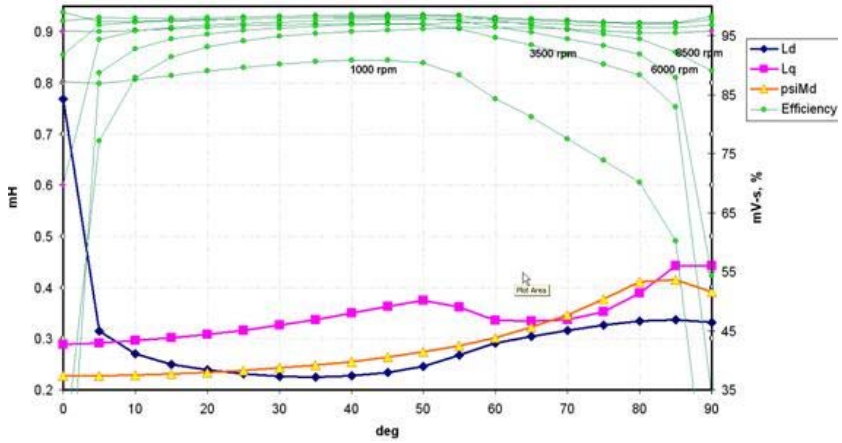

(b) Parameters as a function of advance angle for current controlled by a current set point, ISP=400.

Fig. 3. Lq, Ld, flux links (psi) as a function of advance angle for an unsaturated (ISP=10) and for a saturated (ISP=400) IPM core.

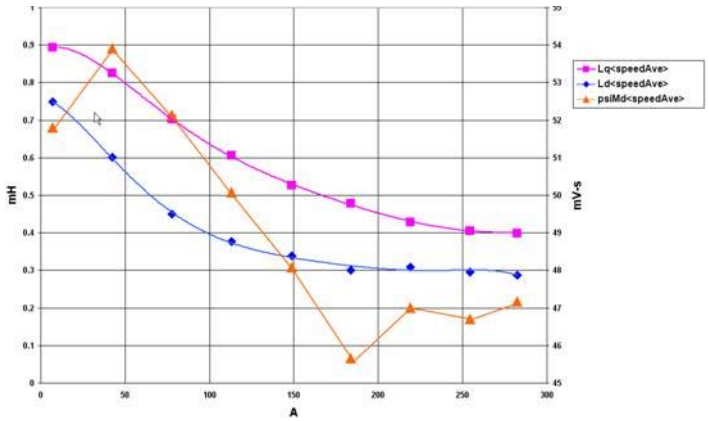

Fig. 4. Inductance and flux links showing the effect of core saturation in the 9-slot, 8-pole IPM.

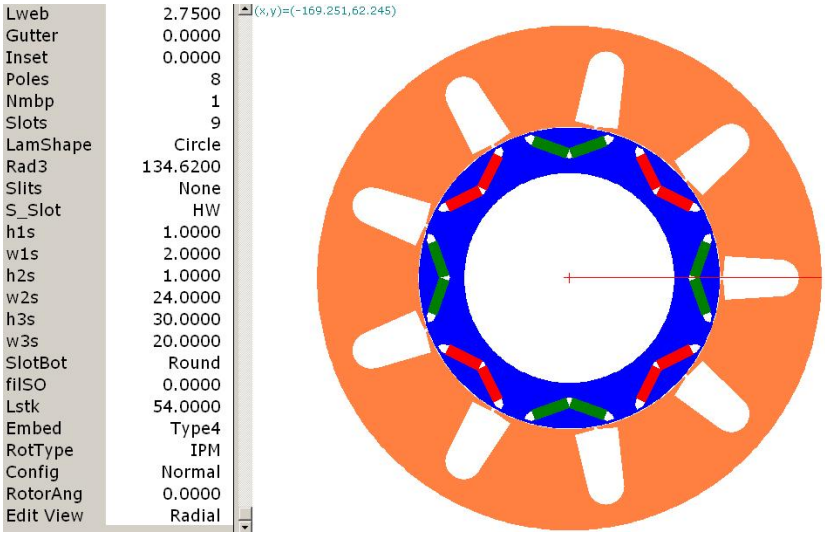

Fig. 5. Outline of IPM configuration with 9 slots and 8 poles.

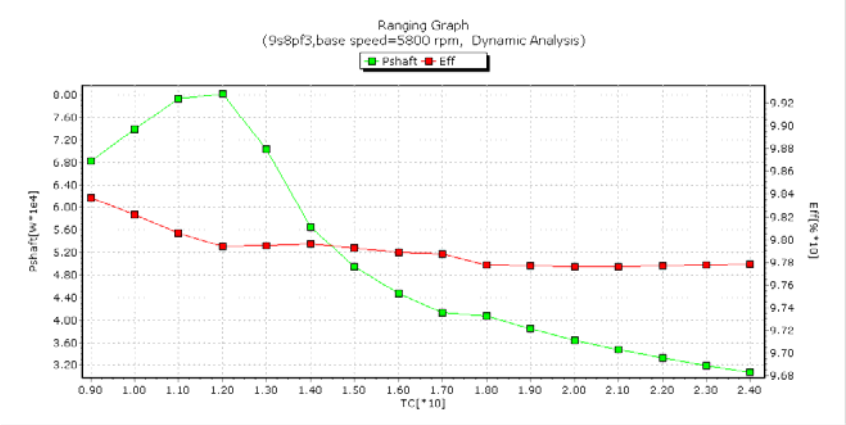

Fig. 6. Maximum shaft power is delivered when there are 11 or 12 turns per coil.

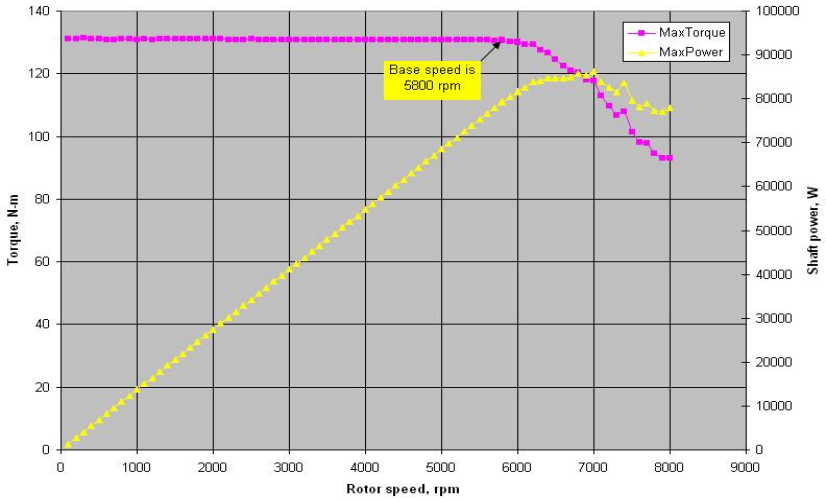

Fig. 7. Determination of base speed when torque begins to drop.

The template editor from SPEED's PC-BDC module shows the physical dimensions in Fig. 8.

Dimensions							
Config	Normal	RotType	IPM	Poles	8	Slots	9
Lstk	54.0000	Embed	Type4	LM	5.3100	S_Slot	HW
Rad3	134.6200	Rad1	80.1900	BetaM	120.0000	SD	14.0000
Stf	0.9700	Inset	0.0000	MagWid	38.4800	SO	2.0000
MOH	0.0000	Bridge	1.0000	SOang	20.0000	TWS	5.0000
RotorAng	0.0000	RadSH	56.3000	TGD	1.0000	Gap	0.7700
Ecc	0.0000	Polarity	Normal	DimGroup	Default	Edges	Bridged
Windings							
Connex	Wye	Throw	1	Offset	3	TC	11
WdgType	Custom	PPATHS	1	Ext	0.0000	NSH	13
WireSpec	SFill	SFg	0.7000	XET	1.0000	InsThick	0.0364
Skew	0.0000	wb	2.0000	ct_Liner	0.2000	Liner	0.4000
Control							
RPM	5800.0000	Vs	450.0000	Drive	Sine	DCSource	Fixed DC
ISP	400.0000	DuCy	0.5000	Sw_Ctl	ISP_HB	*gamma	43.0000
HBA	32.0000	HBtype	Constant	dq0	true	alpha6	0.0000
ChopType	Soft	FixfChop	ISChop12	fChop	40.0000	uCFR	600.0000
SVmode	Auto	VGCoefft	1.0000	u_MSVM	0.8000	MIX	1.0000
PGain	1.0000	IGain	0.0000	G_d	0.0000	G_q	0.0000
NumPoly	1			uVdm	0.0000	uVqm	0.0000
PolyOffs	1	Bifilar	false	NphUni	4	kBif	0.0000
Settings							
ISLA	64.0000	Tol	8.0000	Tol_ISLA	Auto	Cycles	0
EMFCalc	ToothFlux	eCalc	Auto	CalcVwfm	dPsi/dt	XRx	0.0000
CalcVer	cv9	dqRevert	false	eqRevert	false	RTorq	On
TorqCalc	Pos_Seq	TSMin	0.0000	TSMax	0.0000	rpmBase	1000.0000

Basic design | Magnetics | Calc. Options | Thermal | Embedded FEA | Harmonics

Fig. 8. SPEED's PC-BDC template editor for the 9/8 IPM with concentrated windings.

Figure 9 is a flux density map that shows how the flux pattern differs between the 9/8 configuration with concentrated windings and the baseline 48/8 configuration with distributed windings. Note that while the baseline IPM has 4 axes of symmetry, the 9/8 IPM has only one.

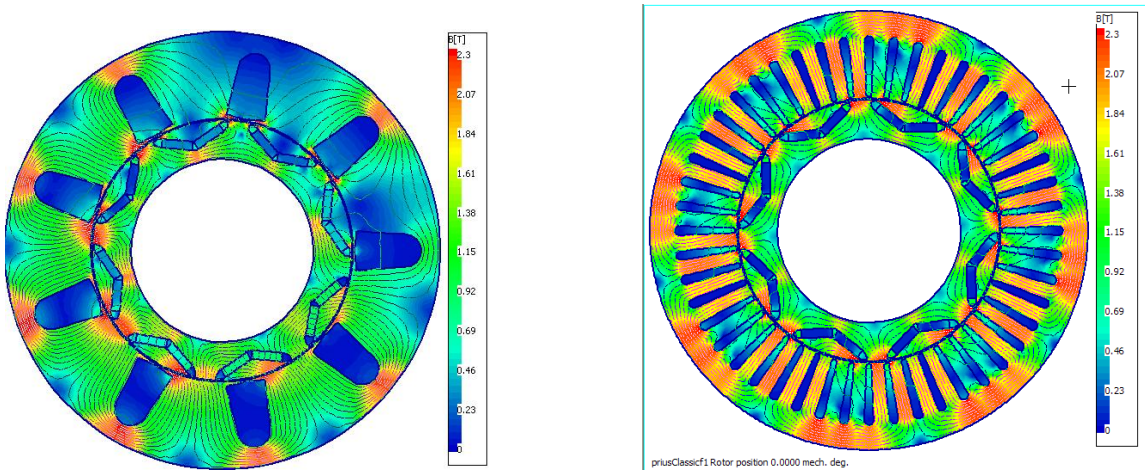

(a) 9/8 configuration with concentrated windings **(b) Baseline configuration with distributed windings**

Fig. 9. Flux density maps showing asymmetric flux linkages of the 9/8 motor during operation at 5,800 rpm compared with the axisymmetric flux linkages of a baseline motor.

Table 1 compares the motor weight and cost of the 9/8 IPM with concentrated windings against the baseline IPM with distributed windings. The assumption used in this study is that the savings permitted by simplifying fabrication is 2% of the manufacturing and miscellaneous cost. Costs and weights from Table 1, certain performance parameters from Table 2, and volumes of 6.07 L for the baseline IPM with distributed windings and 5.88 L for the 9/8 IPM with concentrated windings were used to calculate the targets in Table 3.

Table 1. Comparison of mass and cost of a baseline IPM having distributed windings with an IPM having concentrated windings.

Component or feature	Price ($/kg)	Baseline commercial IPM model with distributed windings (6.07 L volume)		9/8 IPM model with concentrated winding (5.88 L volume)	
		Mass (kg)	Cost ($)	Mass (kg)	Cost ($)
Sintered magnets	89.18	0.671	59.84	0.671	59.83
Rotor core laminations	3.07	3.391	10.41	3.391	10.41
Stator core lamination	2.91	11.411	33.21	11.577	33.69
Rotor shaft (75 mm)	3.97	5.718	22.70	5.718	22.70
Copper wires	7.34	5.230	38.39	6.031	44.27
0.22-in. thick Al housing	2.20	3.10	6.82	3.01	6.63
Manufacturing and misc.			40% of material cost 68.55		38% of material cost[1] 67.46
Total		29.52	239.92	30.40	244.99

[1] The 2% difference in manufacturing and miscellaneous costs is the savings assumed from simplified fabrication procedures (bobbin winding the stator segments followed by stator assembly).

Table 2. Comparison of performance parameters and FreedomCAR targets of a baseline IPM having distributed windings with an IPM having concentrated windings

	Baseline IPM with distributed windings at base speed, 2,500 rpm	9/8 IPM with concentrated windings at base speed, 5,800 rpm	9/8 IPM with concentrated windings at 18,500 rpm	9/8 IPM with concentrated windings at 33,460 rpm
Shaft power, kW%	70.46	79.50	72.40	62.78
Shaft torque, N-m	269.1	130.9	37.37	17.92
Efficiency, %	86.5	98.07	95.45	86.23
Shaft fluctuations, N-m	39.59	9.66	3.05	2.63
Mean FE torque, N-m	253.41	113.2	12.59	9.95
J, A/mm^2	32.44	10.72	5.55	4.53
Line current, A_{rms}	277.4	281.4	144.1	118.7
Id, A	-237.4	-191.0	-132.0	-114.1
Iq, A	143.5	206.6	57.8	32.8
Lq, mH	1.0775	.3578	.4343	.4343
Ld, mH	.6871	.2312	.3371	.3371
Copper loss, W	10886	1370	367	244
Core Loss, W	95	197	3080	9781
Bridge flux leakage, %	14.8	19.0	14.9	14.9

Table 3. Values corresponding to FreedomCAR targets

Quantity	Baseline IPM with distributed windings	9/8 IPM with concentrated windings at 5,800 rpm	9/8 IPM with concentrated windings at 18,500 rpm	9/8 IPM with concentrated windings at 33.460 rpm	Approximate 2015 targets
$/kW	3.41	3.08	3.08	3.90	7
kW/kg	2.39	2.62	2.38	2.06	1.3
kW/L	11.6	13.5	12.31	10.7	5
Efficiency, %	86.5	98.1	95.5	86.2	97
Torque ripple, %	15.6	8.5	24.2	26.4	5

The driving schedule simulation employs a vehicle model that computes the power needed at the vehicle's tires for it to follow a specified speed-versus-time profile. The performance of the IPM motor is modeled following the standard d-q transformation approach described in reference 1. The IPM motor uses the fundamental Ld and Lq inductances and magnet flux-linkages with their dependence on stator current shown in Fig. 4. These are determined with Version 8.0 of SPEED-FE employing a 2-dimensional finite element computation of saturation effects. At every time step, the model computes the voltage, electrical current, and advance control angle needed to meet the power demanded by the driving schedule.

The inverter model receives from the motor model a demand for power, voltage, current, and advance control angle and computes the power demand on the battery. The computed total power demand for the battery includes the losses in the cabling and battery. To facilitate comparison between the 9/8 IPM with concentrated windings and the baseline 48/8 IPM with distributed windings, it was assumed that the vehicles traveled over level ground without climatic wind and that the transmission losses, which occur between the motor's output axle and the tires, were zero. Figure 10 shows the chronological demand velocity of the vehicle for the US06 and FUDS schedules.

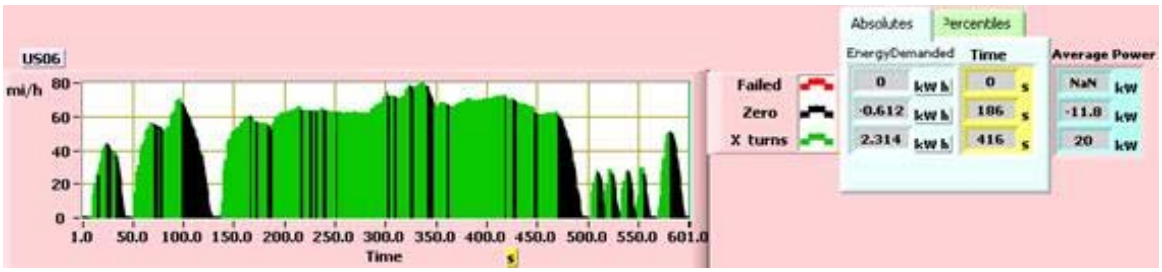

(a) US06 cycle

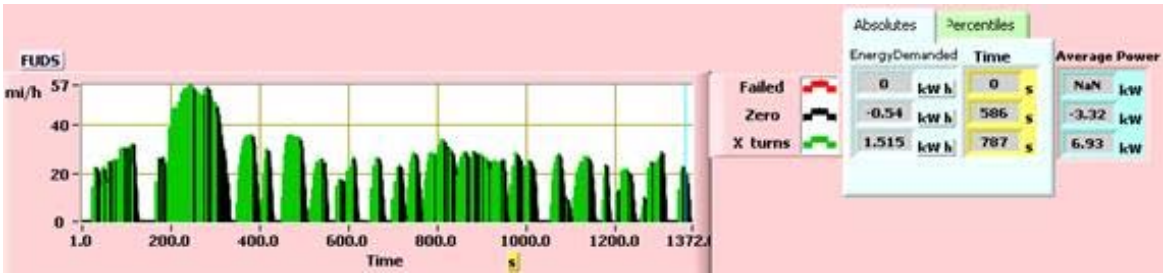

(b) FUDS cycle

Fig, 10. Vehicle demand velocity versus time for two standard driving schedules.

Considering that the tire diameter and vehicle velocity determine the rotational speed of the wheels, it is the task of the effective gear ratio between the wheels and the electric motor's rotor to operate the motor in its optimum speed range. For example, the baseline IPM with distributed windings can meet demands of the US06 and the FUDS cycle with a gear ratio of 4.114. The 9/8 IPM with concentrated windings with the same gear ratio fails to meet the power demand several times along the driving cycle, accumulating a deficit of 13.2% and 5.8% of the total energy demanded by the US06 and FUDS cycles, respectively. This may be remedied by increasing the gear ratio multiplier, defined as the total gear ratio divided by 4.114, which eliminates the energy deficiency and produces a valid mpg rating. As the gear ratio multiplier continues to increase, the mpg value passes through a maximum and again encounters a region with an energy deficiency. This means that there is a value for the gear ratio multiplier at which maximum mpg occurs.

Figure 11 is the simulation summary of the baseline IPM with distributed windings traversing the US06 and the FUDS cycles. Figure 12 is the simulation summary of the 9/8 IPM with concentrated windings traversing the US06 and the FUDS cycles. Table 4 summarizes the results of ORNL's US06 and FUDS driving simulations in which one traction drive model was a baseline 48/8 IPM with distributed windings and the other was the new FSCW 9/8 IPM.

Conclusion

At its base speed of 5,800 rpm, the 9/8 IPM with concentrated windings performs better than the baseline IPM with distributed windings. It has half the torque ripple and a third of the current density reflected in an eighth of the copper losses. It delivers 12.8% more power at an efficiency 11.6 percentage points higher. ORNL's driving schedule simulation program revealed that, in spite of its superior performance at base speed, it could not meet the power demands of the US06 driving schedule unless the gear ratio was multiplied by 3.5 to increase the effective gear ratio from 4.114 to 14.399. This increase requires the motor's rotor to operate at angular velocities of up to 33,460 rpm, which is unreasonably high. Further work is warranted to coordinate motor design with the required performance of IPM motors with concentrated windings.

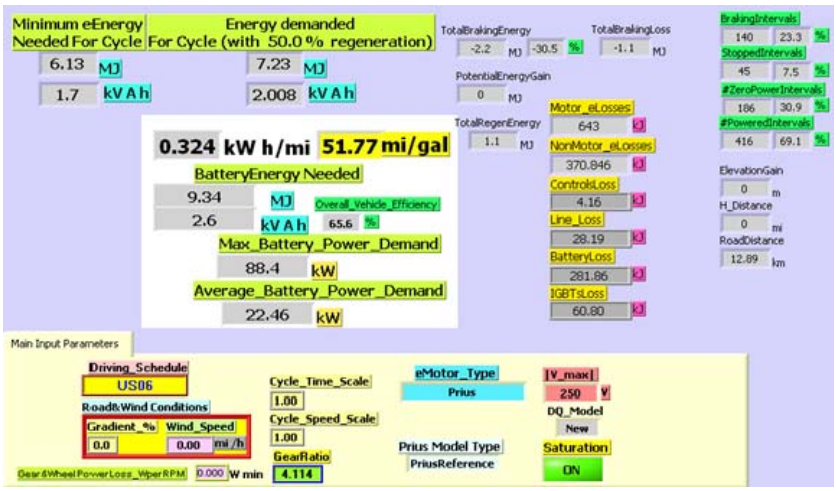

(a) US06 cycle

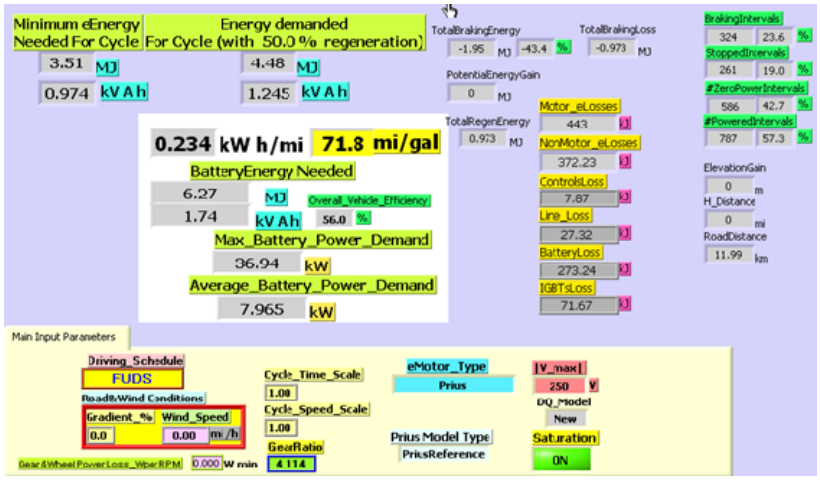

b) FUDS cycle

Fig. 11. Simulation summary of baseline IPM with distributed windings for two driving cycles.

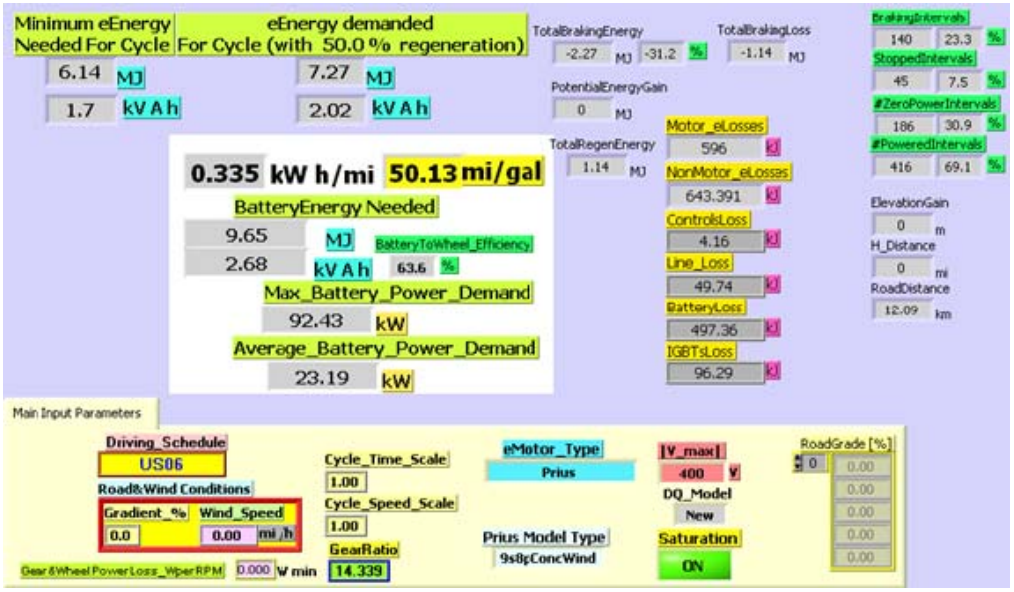

(a) US06 cycle

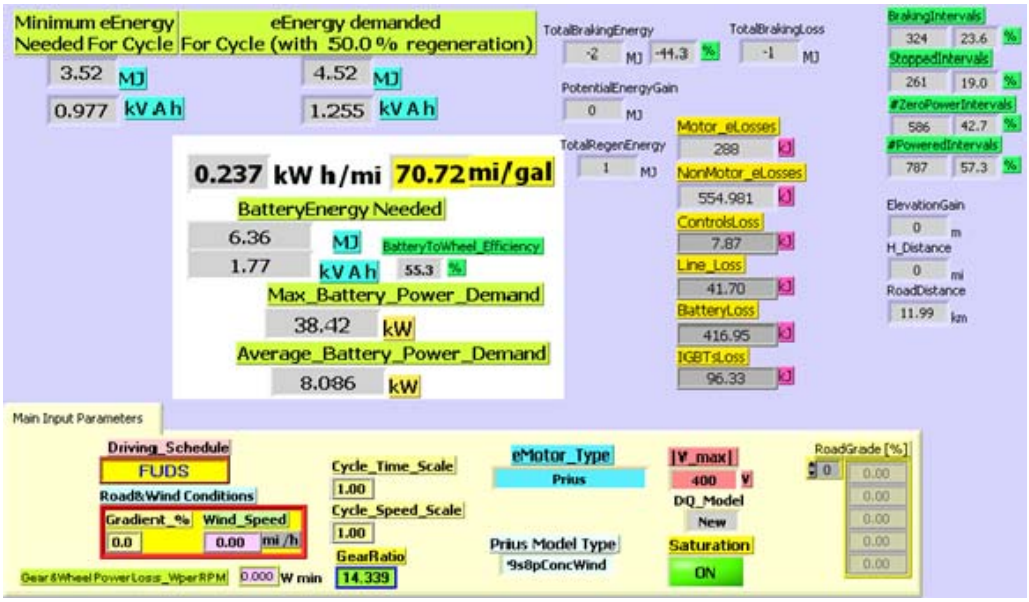

(b) FUDS cycle

Fig. 12. Simulation summary of 9/8 IPM with concentrated windings for two driving cycles.

Table 4. Summary of miles per gallon for baseline IPM with distributed windings and 9-slot, 8-pole IPM with concentrated windings traversing US06 and FUDS cycles

	Baseline 48/8 distributed windings				9/8 concentrated windings			
	US06 cycle		FUDS cycle		US06 cycle		FUDS cycle	
Reducing gear*	% energy deficiency during operation	Miles per gallon	% energy deficiency during operation	Miles per gallon	% energy deficiency during operation	Miles per gallon	% energy deficiency during operation	Miles per gallon
0.5×	2.23		0	61.89				
1×	0	51.77	0	71.80	13.2		5.86	
1.25×	0	51.40	0	72.34				
1.5×	4.7		0	71.93				
2×	29.5		5.6		2.14			61.93
3×					.0815			69.33
3.25×					.0244			
3.5×					0	50.13		70.68
4×					0	49.90		71.24
4.5×					0	49.33		71.19
6×					0	48.53		70.78

* The base gear ratio of the simulation is 4.114, which means that the motor's rotor rotates 4.114 times faster than the vehicles' wheels.

Reference

1. P. J. Otaduy, J. S. Hsu, and D. J. Adams, *Study of the Advantages of Internal Permanent Magnet Drive Motor with Selectable Windings for Hybrid Electric Vehicles*, ORNL/TM-2007/142, Oak Ridge National Laboratory, 2007.

3.4 Amorphous Core Material Evaluation

Principal Investigator: John W. McKeever
Oak Ridge National Laboratory
National Transportation Research Center
2360 Cherahala Boulevard
Knoxville, TN 37932
Voice: 865-946-1316 ; Fax: 865-946-1262; E-mail:mckeeverjw@ornl.gov

DOE Technology Development Manager: Susan A. Rogers
Voice: 202-586-8997; Fax: 202-586-1600; E-mail: Susan.Rogers@ee.doe.gov

ORNL Program Manager: Mitch Olszewski
Voice: 865-946-1350; Fax: 865-946-1262; E-mail: olszewskim@ornl.gov

---

Objectives

- Conduct a four-step evaluation of the potential for soft amorphous or nanocrystalline core materials to improve the efficiency of radial-gap interior permanent magnet (IPM) motors.
  - — Obtain the latest magnetization and loss data from vendors to use in motor simulation.
  - — Obtain cost data from vendors to compare with the cost of standard laminated M-19 core material.
  - — Determine feasibility of manufacturing bulk pieces of amorphous material sufficiently large to fabricate a stator and core for a 55-kW radial-gap IPM motor.
  - — Perform simulations comparing a baseline IPM motor having a standard M-19, 24 gauge 3% silicon steel laminated core with a motor having a core fabricated from 8-in. wide by 0.001-in. thick Metglas® 2605SA1 tape.

Approach

Task 1. Acquire latest material property data from vendor for motor performance simulations.

- Communications with experts such as Matthew Willard (Naval Research Laboratory) were made to acquire background data on amorphous (non-detectable crystal size) and nanocrystalline (crystal sizes below 0.1 μm) materials. Vendor representatives at Metglas®, Hitachi Metals, and AK Steel provided Metglas and M-19 loss and cost data.
- Magnetec was initially responsive but later became unwilling to communicate further because the company has no development of shredded powder cores and cannot make stacked laminations because of the brittleness of their material, which is advertised as Nanoperm®.
- Light Engineering, Inc., was contacted regarding one of its commercially available axial-gap motors made with Metglas to find out if it could meet the FreedomCAR cost target.

Task 2. Perform motor performance analyses.

- Loss data for Metglas were put in a form compatible with SPEED software for simulations of the performance of a baseline IPM that is similar to a commercially available IPM motor. Cost data for Metglas were obtained for comparison with cost data for M-19 silicon steel.
- Performance simulations of the baseline IPM with a Metglas core were compared with simulations of a baseline IPM with a standard M-19 silicon steel core.

Task 3. Perform cost impact analysis

- Representatives from Metglas and Hitachi discussed the feasibility of applying Powerlite® technology, which Hitachi uses to produce small amounts of material for use in chokes, to produce larger chunks of material for use in stator segments and rotors of radial-gap IPM motors.

Major Accomplishments

- Determined that the study should focus on amorphous Metglas rather than nanocrystalline Nanoperm, which is in reality Finemet. This proved to be a good choice because even though the Metglas flux density saturation was 0.4 T above that of Nanoperm, it was still not sufficiently high to deliver the required power at 2,500 rpm or 6,000 rpm.
- Obtained Metglas 2605SA1 loss data and reduced it to a form that could be used in SPEED software for motor simulations at 167 Hz (2,500 rpm) and 400 Hz (6,000 rpm).
- Determined the material cost of Metglas 2605SA1 is 4.5 times that of M-19 laminated silicon steel.
- Determined there is no known way to produce bulk pieces of Metglas 2605SA1 at reasonable cost for radial gap motor stators and rotors. Commercial axial-gap motors that can meet FreedomCAR targets except for cost are available from Light Engineering.
- Calculated and compared the performance of a baseline IPM with a standard M-19 core and the same motor with a Metglas 2605SA1 core. The comparison showed there is no gain in efficiency at 2,500 rpm or 6,000 rpm at maximum current.
- Detailed examination of the simulations showed the following.
  - The increased magnetic permeability of the Metglas led to a 2.2% increase in flux leaking through the bridge at 2,500 rpm and an increase of 0.4% at 6,000 rpm.
  - The reduced saturation flux density of Metglas (1.56 T) compared with the standard M-19 silicon laminates (2.2 T) prevented the Metglas motor from achieving sufficient flux linkages to deliver the amount of torque and power delivered by the M-19 motor.
  - Because of the lower saturation of the Metglas core, the additional copper losses overshadowed the reduction in eddy current losses leading to reduced efficiency

Future Direction

- Further work in this area is not planned.
- If further work were pursued, two significant areas would require development:
  - A major effort would be necessary to develop a way to produce bulk material from as-made 0.001 Metglas tape, such as weaving on a computerized loom.
  - A major effort would be necessary to develop an IPM that can deliver the required power at the saturation flux density of Metglas.

Technical Discussion

Willard of the Naval Research Laboratory sent a reference to a 1999 document (of which he was a co-author) that summarizes then-recent developments in the synthesis, structural characterization, properties, and technology applications related to amorphous and nanocrystalline soft magnetic materials [1]. ORNLs initial research path was to investigate the nanocrystalline material marketed by Magnetec as Nanoperm. Willard knew of only one commercially available nanocrystalline soft magnetic alloy, which is marketed under the names of Finemet by Hitachi Metals and Vitroperm® by Vacuumschemeltze. Its composition is Fe-Si-B-M-Nb-Cu, whereas the alloy Nanoperm has the composition Fe-Zr-B-Cu [2]. The Magnetec product Nanoperm has a composition like that of Finemet rather than like the alloy composition associated with Nanoperm.

Representatives from Metglas (which was acquired by Hitachi Metals) and from Hitachi Metals were helpful and were willing to discuss related technology by phone as well as email. Hitachi's chief engineer suggested that the nanocrystalline materials about which we were inquiring are unsuited for motor

applications because they are too brittle to handle and their saturation flux density is only 1.2 T. Instead, he recommended an amorphous Fe-based alloy, such as Metglas, which is more ductile and has a saturation flux density of 1.6 T. His recommendation and our comparison of the properties of Finemet and Metglas led to our decision to evaluate the Metglas alloy 2605SA1.

Vendor loss data for Metglas 2506SA1 (from an Electric Motor Education and Research Foundation CD containing the third edition of *Lamination Steels*) were put into a form compatible with SPEED software for a comparative IPM motor performance simulation using a standard M-19 core and a Metglas core. These loss data were submitted to a nonlinear least squares fit using the form of the Steinmetz equation for eddy current loss and hysteresis loss,

$$P_{loss} = C_h f B_{Peak}^{a+bB_{peak}} + C_e f^2 B_{Peak}^2 \quad . \tag{1}$$

The parameters from the fit for loss in W/lb were, $C_h = 0.0010316$, a = 1.4712, b= –0.21237, and $C_e = 1.36585 \times 10^{-6}$. The first three parameters were entered as calculated in the SPEED database for Metglas. The last parameter was entered into the SPEED database as $C_{el} = C_e/(2\pi^2) = 6.919 \times 10^{-8}$ to be compatible with the database form of the eddy losses. The fit provided loss values in W/lb within about 1% at 400 Hz and 6% at1000 Hz. The upper limit for this study was 400 Hz..

The efficiency of a baseline IPM motor with a laminated M-19, 24 gauge silicon steel core was compared with the efficiency when the core was replaced by Metglas 2605SA1. The efficiency curve as a function of line current is shown in Fig. 1. The surprising result—that there was no gain at 2500 rpm until the line current was below 100 A, even though Metglas reduced core losses by a factor of 25—suggested that other properties were impacting the performance. Figure 2 compares the magnetization curves for laminated M-19, 24 gauge silicon steel and for Metglas 2605SA1 on a small scale to emphasize the crossover at 3000 A-turns/m, and compares the 1.56 T saturation of the Metglas with the 2.2 T saturation of M-19. Saturation of the magnetic flux density in the motor with a Metglas core prevented the motor from delivering the power available to the motor with the M-19 core (Fig. 3).

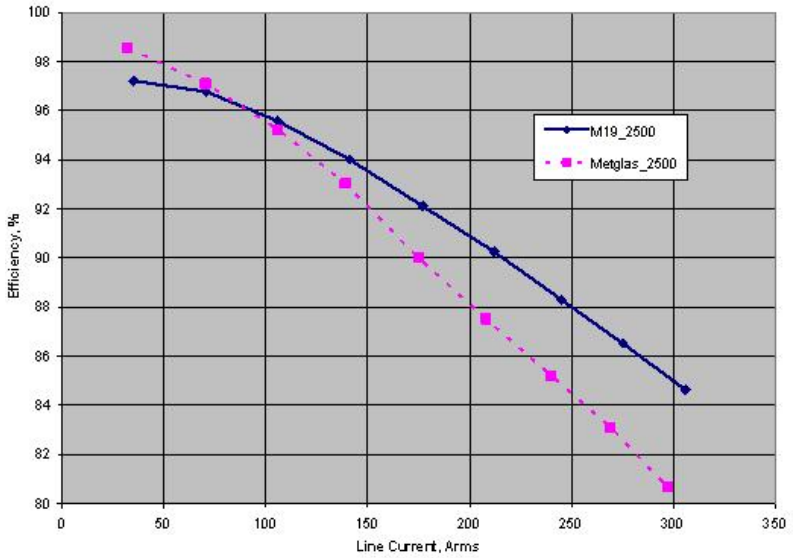

Fig. 1. Efficiency of baseline IPM with M-19 and Metglas 2605SA1 at 2500 RPM.

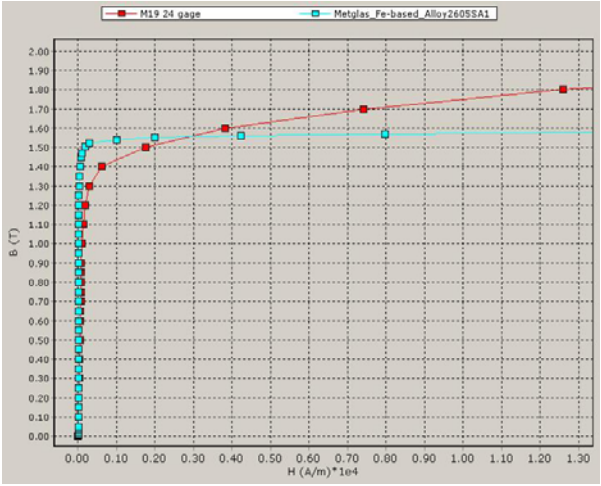

Fig. 2. Magnetization curves of laminated M-19, 24 gauge silicon steel and Metglas 2605SA1.

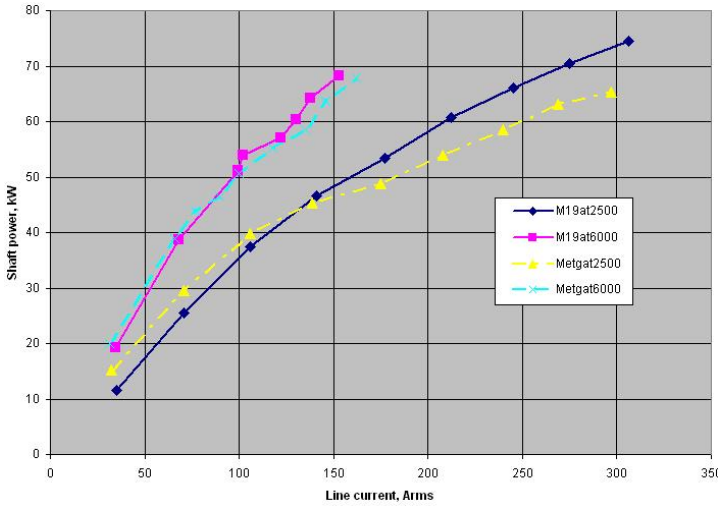

Fig. 3. Shaft power curves of laminated M-19, 24 gauge silicon steel and Metglas 2605SA1.

Increased power delivery from the motor with an M-19 core is enabled by its ability to support more flux linkages. This is illustrated by the more intense orange and red areas for M-19 in Fig. 4a compared with the same regions for Metglas in Fig. 4b. By setting the B(T) scale so that yellow appears at saturation (2.2 T for M-19 and 1.56 T for Metglas), Fig. 5b shows that during operation, the Metglas core is saturated over a much larger region than the M-19 core (Fig 5a). Larger copper losses in the motor with the Metglas core (Fig. 6) were responsible for canceling the benefits of reduced eddy current losses. The increased copper losses were the result of increased field weakening current, Id, which produces no torque but adds to the total current. The increased Id resulted because the saturated saliency ratio for Metglas is below that for M-19 (Fig. 7); and as the direct and quadrature currents, Id and Iq, readjust to produce maximum power, Id must increase more for Metglas to compensate for the reduced saliency ratio. This is shown in Eq. (2).

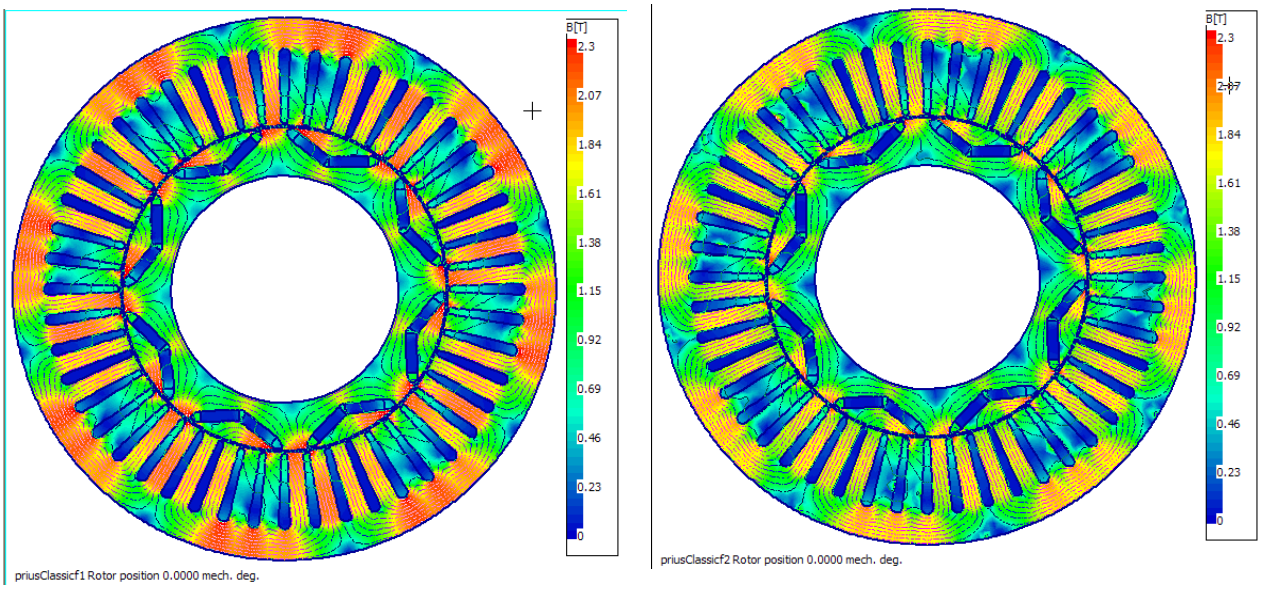

(a) Flux density in laminated M-19, 24 gauge core **(b) Flux density in Metglas 2605SA1 core**

Fig. 4. Increased flux density in M-19 core provides more flux linkages that produce more power in the motor with the M-19 core.

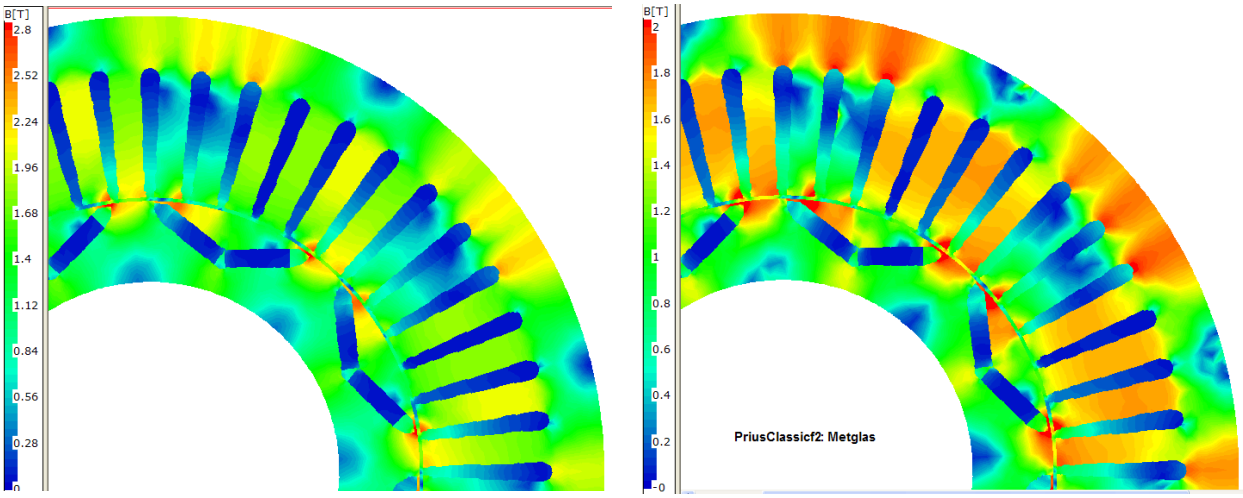

(a) Saturation in laminated M-19, 24 gauge core **(b) Saturation in Metglas 2605SA1 core.**

Fig. 5. Increased saturation in Metglas 2605SA1 core of baseline IPM.

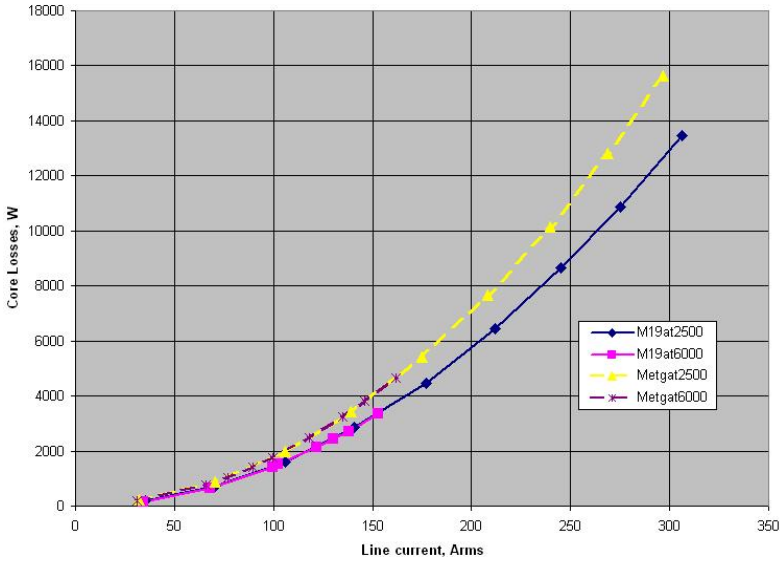

Fig. 6. Increased copper losses in baseline motor with Metglas core.

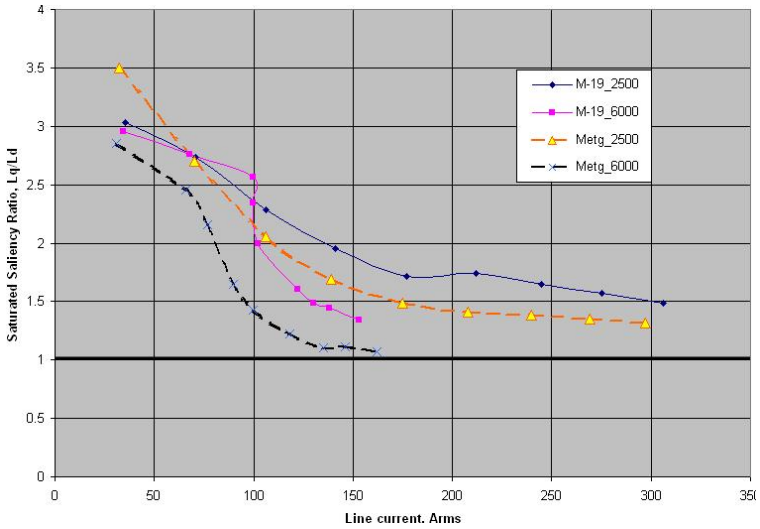

Fig. 7. Reduced saturated saliency ratio for Metglas.

Equation (2) shows the relation between power, saliency ratio, and Id:

$$P = 3p\left[Eq \times Iq - (\rho - 1) \times Xd \times Id \times Iq\right], \qquad (2)$$

where p is the number of pole pairs
Eq is the back-emf, V
Iq is the direct current, which produces torque, A
Id is the direct current, A, which is negative and weakens the magnets' flux density
$Xd = \omega_e L_d$, which is the direct reactance, ohms
$Xq = \omega_e L_q$, which is the quadrature reactance, ohms
ρ is the saliency ratio of the saturated core, which equals Xq/Xd or Lq/Ld

The first term may be considered to be a magnetic power and the second term to be a reluctance power. Inductances are corrected in SPEED's finite element analysis for saturation. Since the Metglas saliency ratio of the inductances falls below the M-19 saliency ratio, the direct current, which is negative, must increase to try to maintain maximum power. This makes the total current larger, thereby increasing the copper losses.

A representative for Metglas in the United States provided three cost estimates for purchases of 50 kg, 100 kg, and 1000 kg quantities. These estimates were $15.75/kg, $12.30/kg, and $9.20/kg respectively. These three points determine the coefficients of an equation to extrapolate the cost of 10,000 lb, or 4536 kg, the quantity for which AK Steel estimated a cost of $0.90/lb ($1.98/kg). The Metglas cost projection equation is

$$\$/kg = 8.85 + 337.58e^{-0.9948*\ln(\text{kg purchased})}, \quad (3)$$

which is $8.93 for 10,000 lb; therefore, material costs for Metglas 2605SA1 are 4.5 times higher than for M-19 laminated silicon steel.

Representatives for Metglas and Hitachi discussed the feasibility of applying Powerlite technology, which Hitachi uses to produce small amounts of material for use in chokes, to produce larger chunks of material for use in stator segments and rotors of radial-gap IPM motors. Their Powerlite production facility on the outskirts of Deli, India, is very labor-intensive because the 0.001 in. thick pieces of tape are layered and bonded; 750 layers must be stacked to produce a ¾ in. thick chunk. There are further problems if the layers have complicated shapes that require punching, because the hard tape has a wearing effect on a punch. A new tool is required for about every 1000 punches, further increasing the production costs. There is now no known way to produce Metglas for use in a radial-gap motor at a reasonable cost. Metglas's challenge was to design a radial-gap motor that can use the tape as produced.

A design for such an axial-gap motor produced by wrapping the tape to form an axial core was proposed by Lipo et al. in 1990 [3]. A Hitachi representative referred us to Light Engineering, which developed a line of axial-gap motors of this type. It markets the M3202L2 SmartTorq Axial-gap PM motor, which can deliver torque and power that meet FreedomCAR targets. Upon request, Light Engineering provided a nonbinding cost estimate of about $6743, excluding cabling, for this motor with its inverter drive in lots of 100,000. The company also sent an efficiency map. It appeared that the motor's efficiencies were insufficient to warrant the additional cost, but further simulations and lab measurements would be necessary if FreedomCAR interest in axial-gap PMs were rekindled.

Conclusion

Because of the problems associated with obtaining bulk Metglas and the high material costs, there is low probability that a radial-gap motor could be built to meet the FreedomCAR cost target. The low saturation flux density of Metglas prevented the baseline motor from achieving improved efficiency, showing the importance of considering the motor design when using amorphous core material.

References

1. Michael E. McHenry, Matthew A. Willard, and David E. Laughlin, "Amorphous and nanocrystalline materials for applications as soft magnets," *Progress in Materials Science* **44,** 291–433 (1999).
2. M. A. Willard et al, "Structure and magnetic properties of $(Fe_{0.5}Co_{0.5})_{88}Zr_7B_4Cu_1$ nanocrystalline alloys," *Journal of Applied Physics* **84**(12) (December 15, 1998).
3. T. A. Lippo, C. C. Jensen, and F. Profumo, *A Low Loss Permanent Magnet Brushless DC Motor Utilizing Tape Wound Amorphous Iron,* WEMPEC Research Report 90-18, July 1990.

4. Power Electronics Research and Technology Development

4.1 Wide Bandgap Materials

Principal Investigator: Madhu Chinthavali
Oak Ridge National Laboratory
National Transportation Research Center
2360 Cherahala Boulevard
Knoxville, TN 37932
Voice: 865-946-1411; Fax: 865-946-1262; E-mail:chinthavalim@ornl.gov

DOE Technology Development Manager: Susan A. Rogers
Voice: 202-586-8997; Fax: 202-586-1600; E-mail: Susan.Rogers@ee.doe.gov

ORNL Program Manager: Mitch Olszewski
Voice: 865-946-1350; Fax: 865-946-1262; E-mail: olszewskim@ornl.gov

---

Objectives

- Keep up to date with state-of-the-art SiC power devices by acquiring, testing, and characterizing new-technology silicon carbide (SiC) power devices.
- Utilize new wide-bandgap (WBG) devices in vehicle power electronics simulations to ascertain system level benefits.
- Study conceptual changes to inverters/ converters and their packaging and thermal management designs that are uniquely possibly through the use of WBG devices.

Approach

- Acquire, test, and characterize new-technology WBG power devices
  - — Static characteristic tests
  - — Dynamic characteristic tests
  - — Behavioral modeling

- As appropriate, utilize characterization results in simulations to determine device benefits for power electronics.

- Determine converter concepts that make the best use of the attributes of WBG-based power devices
  - — Survey literature
  - — Design and develop circuits
  - — Model and simulate novel converter designs and thermal control concepts
  - — Research new packaging techniques

Major Accomplishments

- Acquired several SiC junction field effect transistors (JFETs). Tested, characterized, and modeled SiC JFETs and their body diodes.
- Developed several concepts to take advantage of SiC device attributes and completed three new air-cooled traction drive inverter designs.

Future Direction

- The inverter designs developed in FY 2008 will be evaluated to build an air-cooled inverter prototype based on the results of the thermomechanical analysis.
- An electrical design that includes gate drivers, a device layout, and the component inter-connects will also be analyzed.

Technical Discussion

1. Device Testing

The new WBG devices acquired this year were normally-on SiC JFETs, normally-off SiC JFETs, and a high-temperature-packaged normally-on SiC JFET. These devices were tested, characterized, and modeled. The body diode of a normally-on SiC JFET was also tested. All the devices obtained were experimental samples.

2. Normally-on SiC JFET

Static characteristics

Static characteristics of the 600 V, 5 A SiC JFET received this year are shown in Fig. 1 for different operating temperatures. SiC JFETs have a positive temperature coefficient, which means that, as in SiC Schottky diodes, their conduction losses will be higher at higher temperatures. However, the positive temperature coefficient makes it easier to parallel these devices and reduce the overall on-resistance. The on-resistance of the JFET increases from 0.25 Ω at 25°C to 1.07 Ω at 200°C, as shown in Fig. 2.

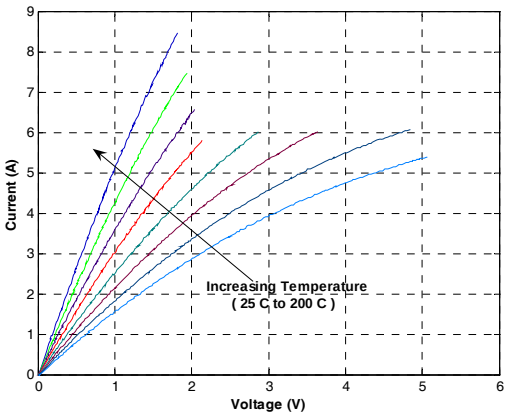

Fig. 1. VI curves of a normally-on SiC JFET at different operating temperatures.

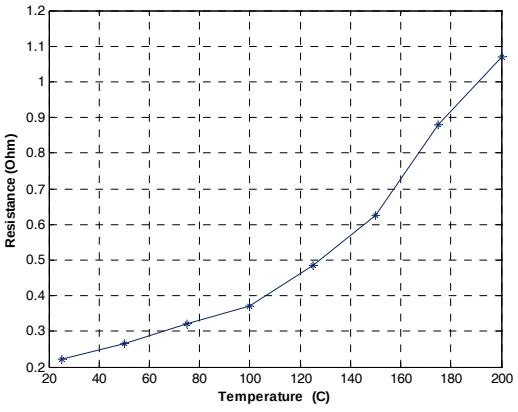

Fig. 2. On-resistance of a normally-on SiC JFET at different temperatures.

Dynamic characteristics

The SiC JFET was tested in a chopper circuit with double pulse switching to observe its dynamic characteristics. The double pulse circuit enables the use of an inductive load instead of a resistive and inductive load together. The current through the inductor builds up during the first pulse, and the peak forward current is adjusted by changing the width of the first pulse. The switch is turned off and turned on for short periods after the first pulse. The turn-on and turn-off energy losses can be obtained during the short pulse intervals.

The turn-on and turn-off energy losses of the JFET during switching are shown in Fig. 3. The turn-on losses do not change significantly with temperature, but the turn-off losses decrease with increasing temperature.

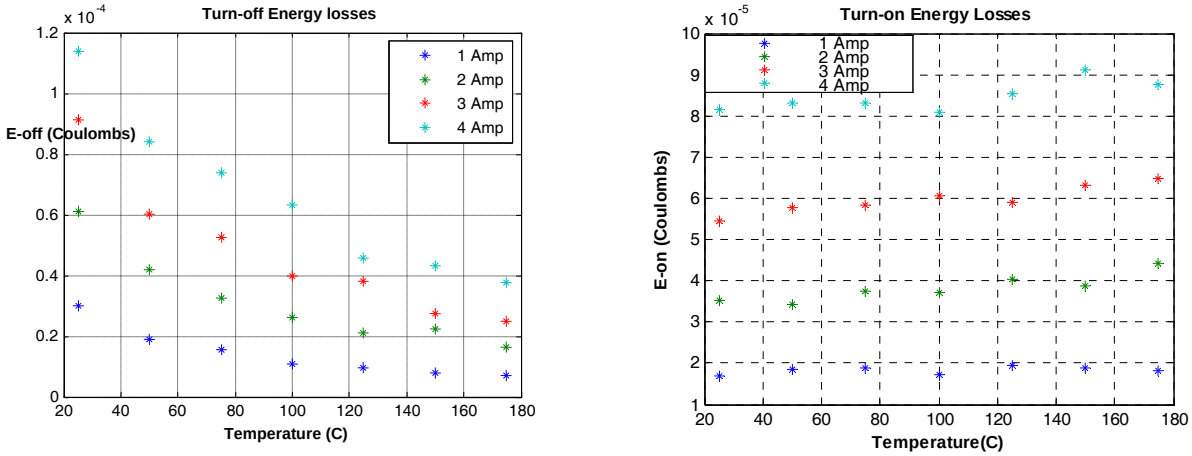

(a) Turn –off energy losses **(b) Turn–on energy losses**

Fig. 3. Switching energy losses of a normally-on SiC JFET for different currents and temperatures.

2. Normally-off SiC JFET

Static characteristics

The static characteristics of an 800 V, 5 A normally-off SiC JFET received this year are shown in Fig. 4 for different operating temperatures. This was the first normally-off SiC JFET tested. Normally-off devices are the preferred type of device in power converters for a fail-safe mode of operation. This could be a revolutionary device, which could have a significant impact on the choice of SiC devices for automotive inverters. Testing of the device determined that the on-resistance of the JFET increases from 0.15 Ω at 25°C to 0.88 Ω at 200°C as shown in Fig. 4.

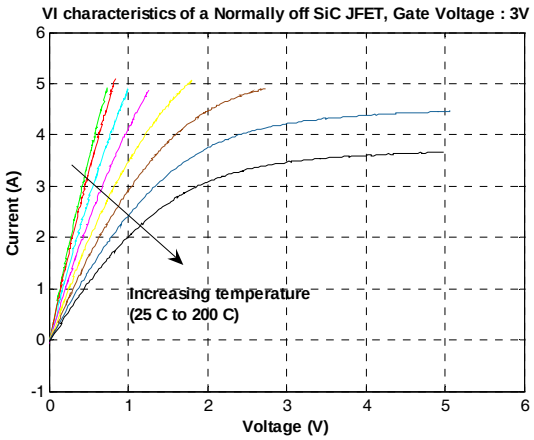

Fig. 4. VI curves of a normally-off SiC JFET at different operating temperatures.

Dynamic characteristics

The turn-on and turn-off energy losses of the JFET during switching are shown in Fig. 5. The turn-on losses do not change significantly with temperature, but the turn-off losses decrease with increasing temperature. The energy losses are not much different from those of the normally-on SiC JFET.

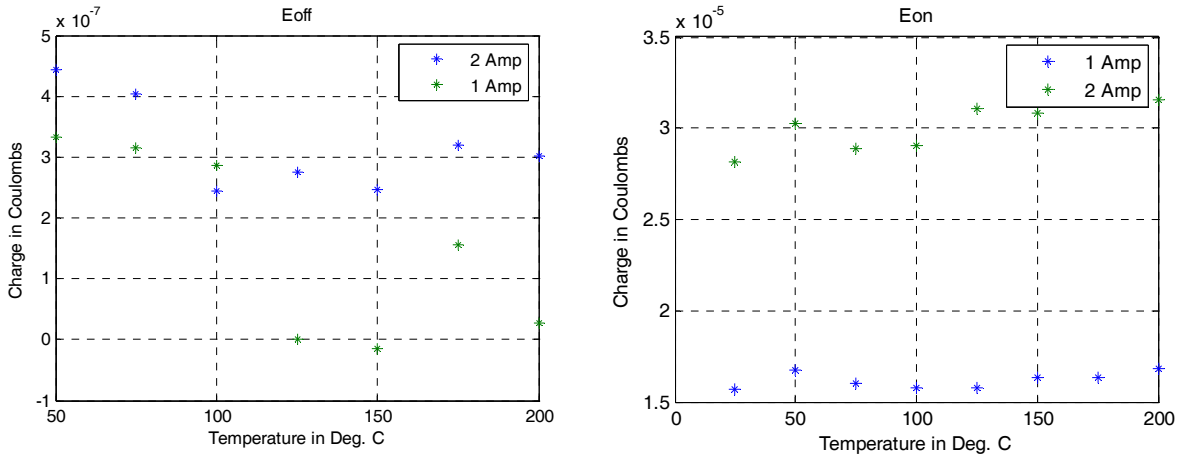

(a) Turn –off energy losses **(b) Turn –on energy losses**

Fig. 5. Switching energy losses of normally-off SiC JFET for different currents and temperatures.

3. High-temperature normally-on SiC JFET

Static characteristics

A high-temperature packaged 600 V, 5 A normally-on SiC JFET prototype device was tested. The tests demonstrated the operation of the SiC JFET at 400°C. On-state resistance increased from 0.25 Ω at 25°C to 2.5 Ω at 400°C. The static characteristics of the JFET are shown in Fig. 6 for different operating temperatures.

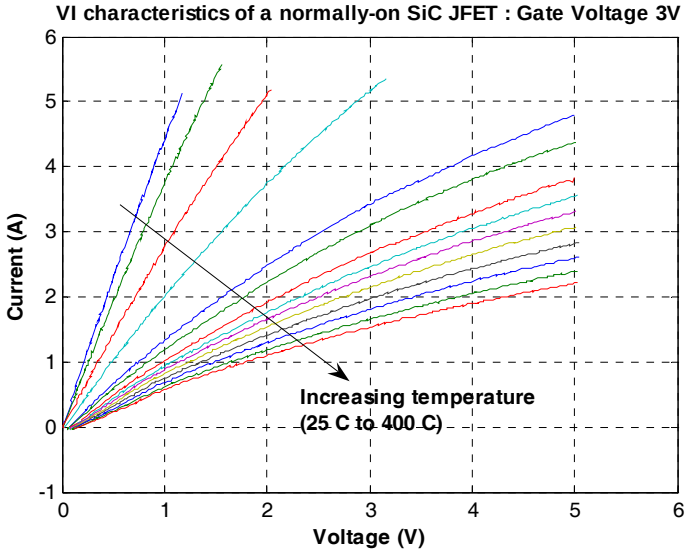

Fig. 6. VI curves for a high-temperature packaged normally -on SiC JFET at different operating temperatures.

4. Body diode of a normally-on SiC JFET

Static characteristics

The body diode in a normally-on JFET can be used as a free-wheeling diode in a voltage source inverter for automotive applications. Using this diode can reduce the number of devices necessary in an inverter by eliminating the anti-parallel diodes. The body diode is available only in normally-on devices with a combined lateral and vertical channel design from SiCED. This particular device is a pn diode formed as a consequence of the specific device design. Static characteristics of the body diode in a 1200 V, 5 A SiC JFET are shown in Fig. 7 for different operating temperatures.

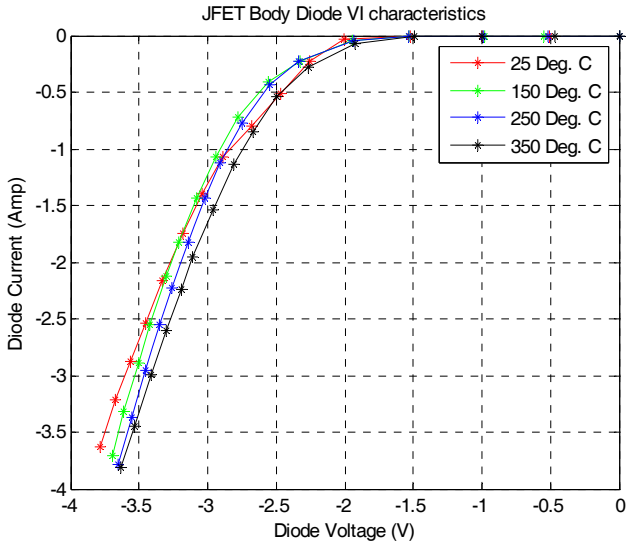

Fig. 7. VI curves of a body diode of a normally-on SiC JFET at different operating temperatures.

Dynamic characteristics

The pn body diode has a longer reverse recovery time than a Schottky diode. This increased recovery time results in switching losses in an inverter. The reverse recovery characteristics of the body diode at different temperatures are shown in Fig. 8. The peak reverse recovery current increases along with temperature. However, the change in current is small, resulting in a minimal increase in reverse recovery losses at higher temperatures.

5. Study of Concepts

Technical areas in which new concepts can be developed were identified during FY 2008. The impact of SiC device attributes on inverters was analyzed, and specific problems were identified that need to be addressed in developing a high-temperature inverter. This analysis resulted in several novel air-cooled SiC-based inverter designs. The main objective of these designs is to enable cooling with air, eliminating the need for the liquid-cooled thermal management systems that are currently used. These designs are expected to increase the power density and decrease the volume and weight for electric-based vehicle traction drive inverters. This design concept will enable the development of an integrated motor/inverter drive system during the next fiscal year.

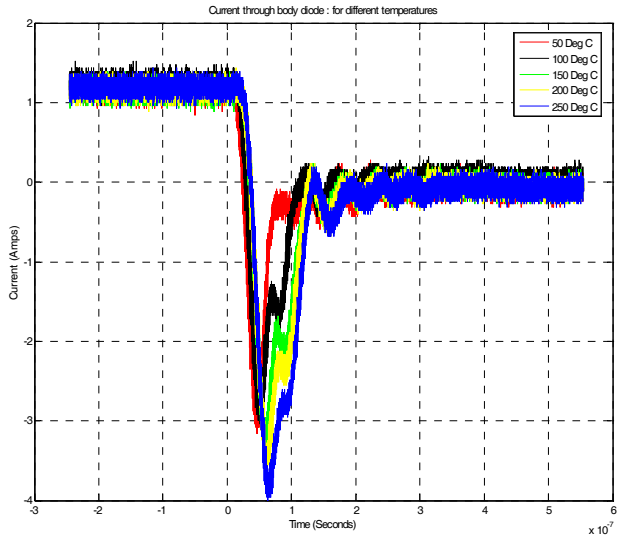

Fig. 8. Reverse recovery characteristics of a body diode in a normally-on SiC JFET.

The selected design will realize the following benefit to achieve high-temperature operation:

- The low-temperature electronics and capacitors (dc-link/filter) will be separated from the high-temperature components, creating both low- and high-temperature zones.

This concept enables the use of low-temperature electronics in close proximity with high-temperature power devices.

- Thermal interface material is eliminated, thereby increasing the thermal efficiency.
- Active cooling of the buss bars will increase the reliability of the inverter.
- The design can be modified for current source, voltage source, or a Z-source inverter.
- Direct-bonded copper material with low thermal conductivity can be used in the thermal design. The design enables the use of cheaper materials.
- The buss bar design will result in fewer problems related to electromagnetic interference.
- The inverter design concept will enable integration with a motor, which will reduce costs through the reduction in the number of connectors and interconnects.
- The number of solder joints will be substantially reduced, increasing reliability and reducing manufacturing costs.
- The capacitor design will enable better cooling of the capacitor and hence increased ripple current handling capability.
- Wire bonds will be eliminated with a novel packaging concept, increasing reliability and reducing manufacturing costs
- Normally-on JFETs can be used if a current-source inverter topology is used.
- The design may allow the elimination of anti-parallel diodes.

Conclusion

Several new SiC JFETs, including a high-temperature packaged SiC JFET, were acquired, tested and, modeled. The body diode in a SiC JFET was tested to evaluate the feasibility of using the diode to

eliminate anti-parallel diodes. Several concepts to take advantage of SiC device attributes were studied and were used to develop air-cooled inverter designs.

Publications

L. M. Tolbert, H. Zhang, B. Ozpineci, and M. Chinthavali, "SiC-based power converters," Materials Research Society Spring Meeting, Symposium D, San Francisco, March 24–27, 2008.

B. Ozpineci, M. Chinthavali, L. M. Tolbert, and H. Zhang, "SiC power electronics research at ORNL," GOMACTech, Las Vegas, March 17–20, 2008.

B. Ozpineci, M. Chinthavali, A. Kashyap, L. M. Tolbert, and A. Mantooth, "A 55 kW three-phase inverter with Si IGBTs and SiC Schottky diodes," I*EEE Transactions on Industry Applications*, **44** (2008).

4.2 An Active Filter Approach to the Reduction of the dc Link Filter

Principal Investigator: Burak Ozpineci
Oak Ridge National Laboratory
National Transportation Research Center
2360 Cherahala Boulevard
Knoxville, TN 37932
Voice: 865-946-1329; Fax: 865-946-1262; E-mail:ozpinecib@ornl.gov

DOE Technology Development Manager: Susan A. Rogers
Voice: 202-586-8997; Fax: 202-586-1600; E-mail: Susan.Rogers@ee.doe.gov

ORNL Program Manager: Mitch Olszewski
Voice: 865-946-1350; Fax: 865-946-1262; E-mail: olszewskim@ornl.gov

---

Objectives

- To replace the bulky dc link capacitor in a traction inverter with a much smaller active power filter (APF) that imitates what a dc link capacitor does.
- The weight and volume of the traction inverter will be reduced while the reliability and lifetime of the inverter will be increased.
- The active filter is expected to weigh half as much as the dc link capacitor and occupy less than half the space.

Approach

- A current source APF with a small capacitor and inductor can be used in the dc link together with semiconductor switches to replace the dc link capacitor.
- The impacts of this approach are reduced size and cost and possibly a more cost-effective solution for high-temperature operation.

Major Accomplishments

- Performance requirements have been established for an active filter.
- An APF has been developed to replace the dc link capacitor.
- A traction drive system has been simulated using both a dc link capacitor model and an APF model replacing the dc link capacitor.
- The practical feasibility of the active filter replacing a dc link capacitor has been assessed. With the current approach, there are efficiency and size concerns that can be solved by using different devices and new designs.

Future Direction

- Develop other circuitry and control algorithms to reduce the APF inductance, inductor current, and switching frequency.
- Develop adaptive controls to automatically update the inductor current depending on the load current.
- Design and build an APF benchtop module. Test the module in a 55 kW inverter, replacing the dc link capacitor.
- Build a 105°C compatible version.

Technical Discussion

Operation principle

The block diagram of the active filter is shown in Fig. 1 connected to the dc link of the traction system. The traction system is composed of a dc source, a three-phase inverter, and a traction motor. The sinusoidal pulse-width modulation (PWM) technique typically used in an inverter introduces high-frequency-current harmonic content in the dc link. Figure 2 shows the typical input current of an inverter. The purpose of the active filter is to absorb ripple current, as a traditional passive filter capacitor does, and leave only the dc component to be drawn from the dc source.

To compensate for the dc link ripple current, a current source active filter topology is used. As shown in Fig. 1, the active filter is composed of an inductor, a full bridge inverter, and a relatively small capacitor for voltage smoothing. The active filter works as a current source inverter without a dc power supply. The inductor current is kept constant and should be larger than the peak value of the ripple current. The filter current injected to the dc link can be positive, negative, or zero depending on the operation mode of the active filter (Fig. 3).

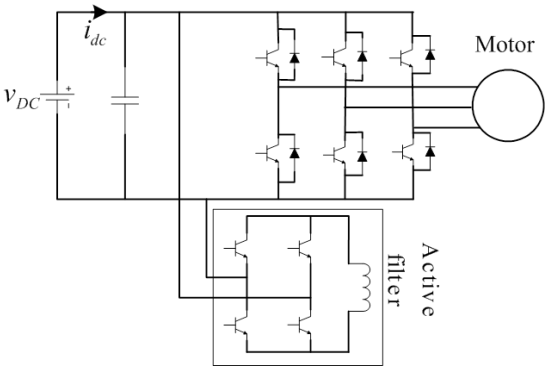

Fig. 1. Traction system with active filter.

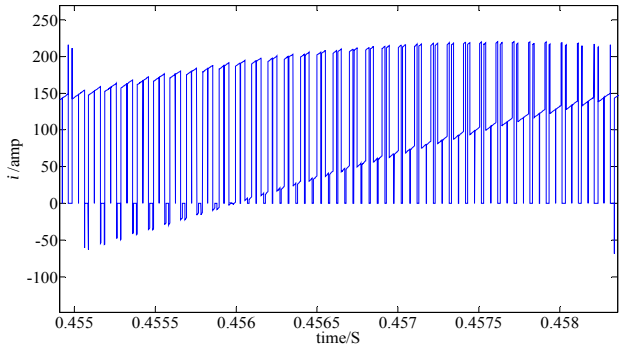

Fig. 2. Input current of inverter.

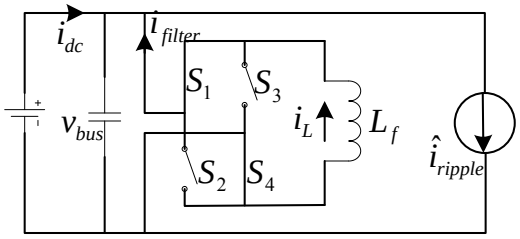

(a) Mode 1

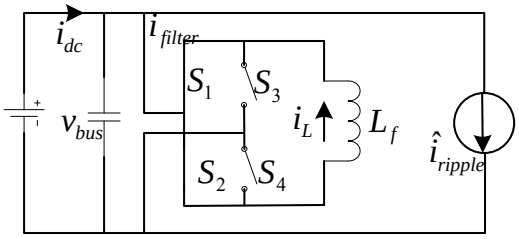

(b) Mode 2

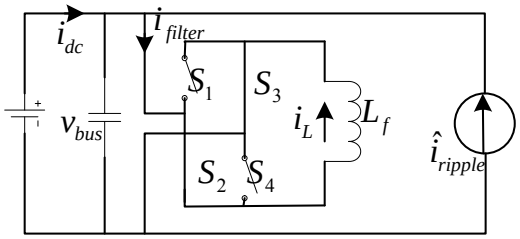

(c) Mode 3

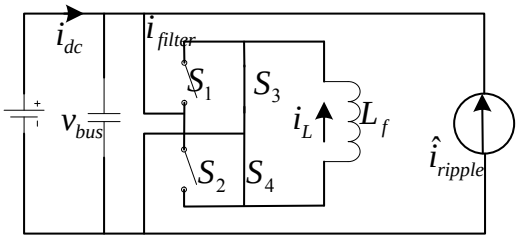

(d) Mode 4

Fig. 3. Equivalent circuit.

To illustrate the operation principle, the equivalent circuit in Fig. 3 is used. In the equivalent circuit, a ripple current source i_{ripple} is used to imitate the effect of the three-phase inverter and the motor. Figure 3 shows the equivalent circuit working in different modes, according to the direction of the filter current. Figure 4 illustrates the operating current and voltage waveforms: the load ripple current, the dc bus voltage, and the injected filter current.

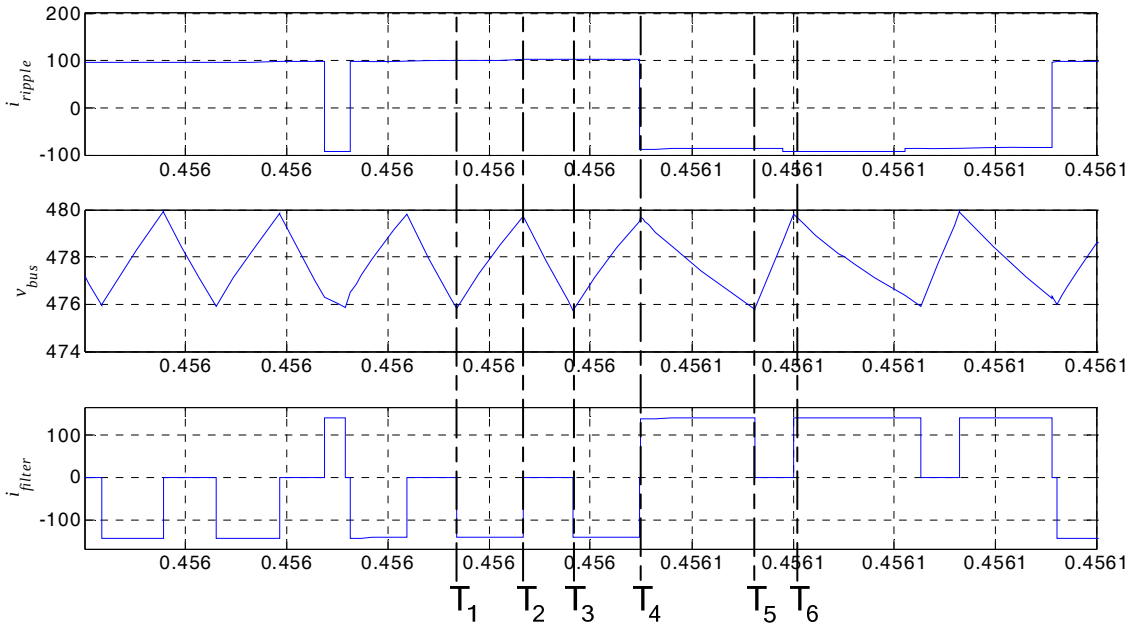

Fig. 4 Waveforms for load ripple current, dc bus voltage, and filter current.

Mode 1: When the ripple current goes into the inverter, which we define as positive, S1 and S4 of the active filter close and the current of the inductor is injected into the dc link; this direction is defined as negative. This mode is also illustrated in Fig. 4 from T_1 to T_2. Since i_{filter} is larger than i_{ripple}, i_{filter} supports i_{ripple} and at the same time charges the capacitor; the voltage, v_{bus}, increases. There is a hysteresis-band for v_{bus}; when it reaches the upper boundary, Mode 2 starts.

Mode 2: In this mode, ripple current is still positive, S1 and S2 close, inductor current i_L freewheels through S1 and S2, and the filter current i_{filter} is zero. The ripple current discharges the capacitor. This mode corresponds to the interval between T_2 and T_3. v_{bus} decreases as a result of the discharge. When it reaches the lower bound, this mode ends.

Mode 3: When the ripple current is negative, S2 and S3 close and filter current i_{filter} is positive. Ripple current i_{ripple} goes into the filter, since the filter current is larger than the ripple current. The current difference $i_L - i_{ripple}$ discharges the capacitor and the dc bus voltage decreases as shown in interval T_4 to T_5 in Fig. 4. When v_{bus} reaches the lower bound, the active filter will change and enter mode 4.

Mode 4: In this mode, S3 and S4 close and the inductor current freewheels. The filter current i_{filter} is zero. Ripple current i_{ripple} charges the capacitor; therefore, the dc bus voltage increases. This mode corresponds to the interval between T_5 and T_6.

From another point of view, the function of this APF is to further increase the frequency of the dc link current so that a small dc link capacitor can filter the ripple current.

Simulation results

According to the operation principle described, a simulation was conducted using Simulink. Some system parameters used in the simulation are listed in Table1. A traction drive system was simulated with a conventional dc link capacitor and with an APF that was designed to match the functions of the dc link capacitor.

Table 1. System parameters

Parameter	Value
dc input voltage	500 V
Power of IM	30 kW
Peak current	200 A
Capacitor	100 μF
Filter inductor	5 mH

Figure 5 shows the filtered and unfiltered dc link currents. Figure 5a is the conventional case with a dc link capacitor and Fig. 5b is the case using the active filter. The dc input current ripple is 10 A in both cases. For the conventional case, the current ripple varies, but the maximum value is around 10 A. Figures 6 and 7 show expanded views of the dc input current and dc bus voltage, respectively. For both cases, the ripple voltage is around 2 V.

For easier comparison, some important system parameters and simulation results are listed in Table 2. As can be seen in the table, only a 100 μF capacitor is needed for the active filter case, compared with a 2,200 μF capacitor in the conventional case to achieve the same filtering results. Although the active filter solution can match the conventional case, note also that four extra insulated-gate bipolar transistors (IGBTs), two extra diodes, and an extra inductor are required for the active filter.

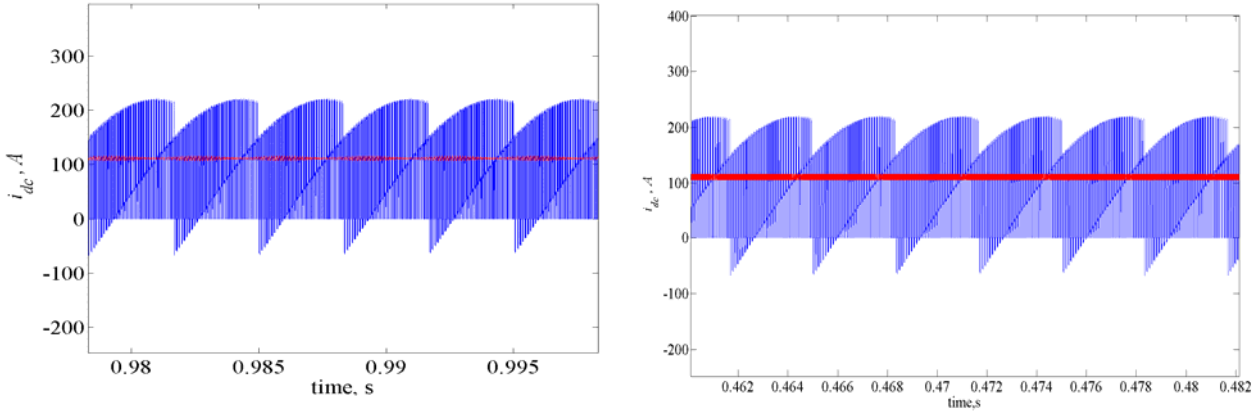

(a) **(b)**

Fig. 5. Inverter input current and dc input current: (a) for capacitor case and (b) for APF case

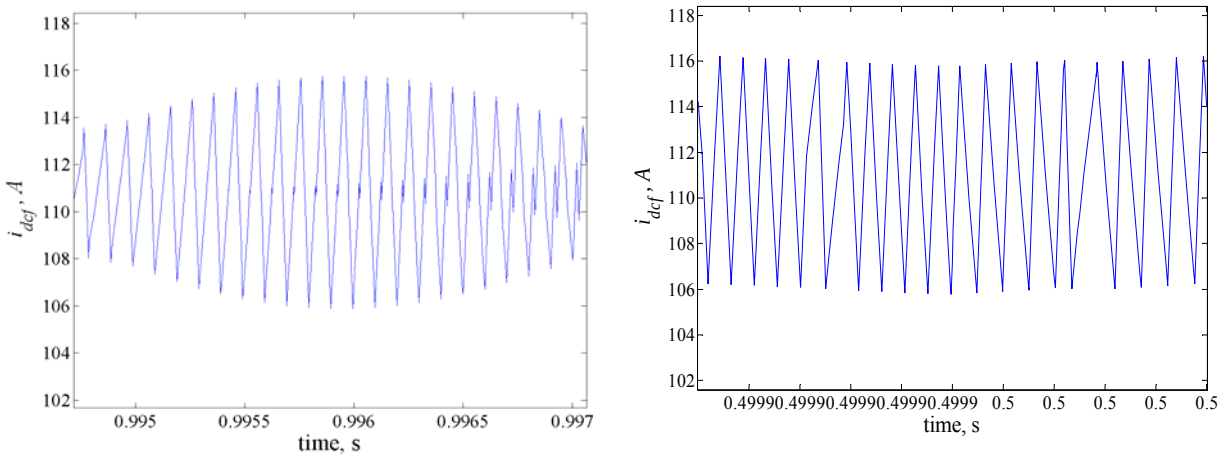

Fig. 6. dc input current

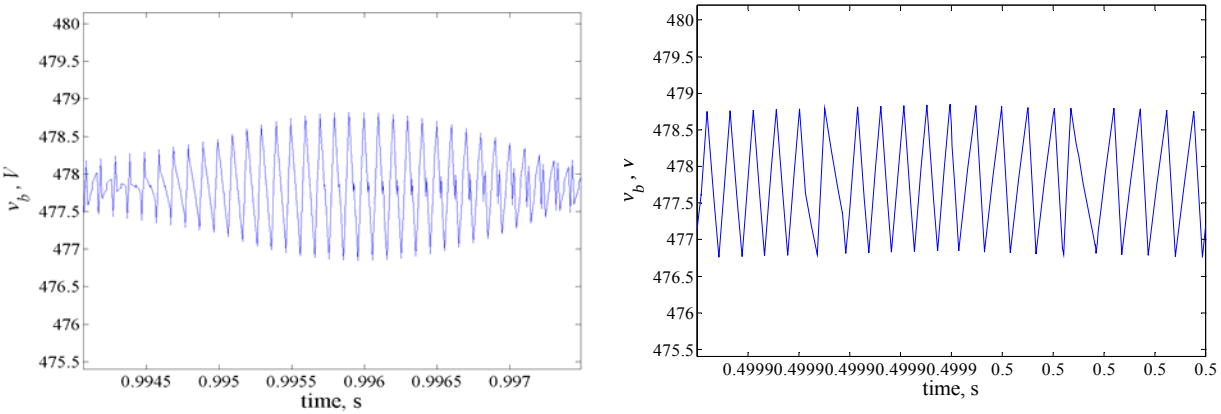

Fig. 7. dc bus voltage

Table 2. Parameter comparison

	Case 1 (capacitor)	Case 2 (APF)
dc link capacitor	2200 μF	100 μF
APF inductor		5 mH
APF frequency		100 kHz
Extra components		4 IGBTs and 2 diodes
APF inductor current		140 A
dc link voltage ripple	2 V	2 V
Input current ripple	10 A	10 A
Current ripple before filtering	220 A	220 A
dc link voltage	500 V	500 V
Output power	30 kW	30 kW

Analysis of parameter dependence

To get better filtering results and reduce the losses associated with the active filter, the performance of the active filter was studied further. Research indicates that the dc bus voltage ripple, with a preset hysteresis band, can affect the dc input current ripple. Figure 8(a) shows the relationship between the two. The current ripple increases along with the increase of the voltage ripple. When the hysteresis band is set to 2 V, the current ripple is 10 A. When the hysteresis band increases to 5 V, the current ripple is 25 A.

The switching losses in power switches are directly proportional to the switching frequency; therefore, to reduce active filter losses, the switching frequency should be lower, too. According to the simulation results, two parameters can affect the active filter frequency: the dc bus voltage ripple hysteresis band and the smoothing capacitor size. An increase in the bus ripple voltage can decrease the switching frequency. However, since the bus ripple voltage is also proportionally related to the current ripple, there are limits on how much it can be increased. A tradeoff is needed. A 2~3 V ripple was assumed for the simulation studies in this project. The capacitor size is inversely proportional to the switching frequency when the capacitor is 1 per-unit (pu), which was 100 μF in this simulation; the maximum active filter switching frequency was 160 kHz. However, when the capacitor size was increased to 2 pu, the switching frequency decreased to 60 kHz.

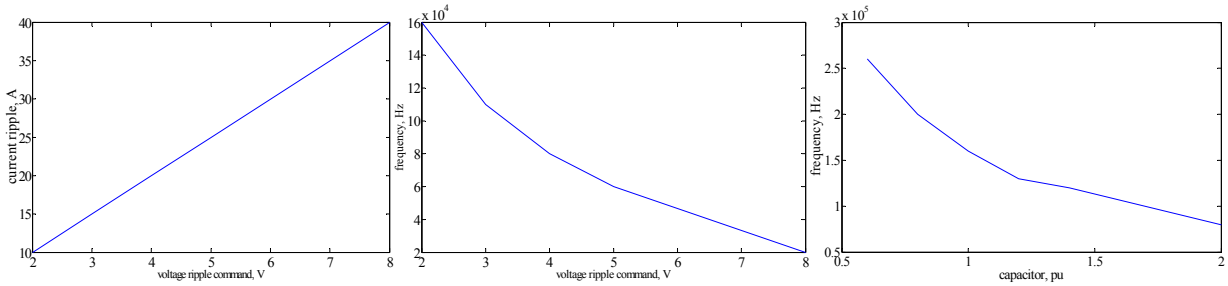

Fig. 8. Parameter dependence.

These parameter dependence relations can be explained by the basic equation

$$\Delta V_{bus} \times C = \Delta Q \quad (1)$$

where ΔV_{bus} is the dc bus voltage ripple, C is the capacitor, and $\Delta Q = I \times \Delta t$ is the change in the capacitor charge. The charging or discharging current I is affected by ΔV_{bus} or C. Therefore, if C is not changed, Δt which is the charge or discharge time, is proportional to ΔV_{bus}, and the average switching frequency is inversely proportional to the voltage ripple. If ΔV_{bus} is kept constant, then the switching frequency is inversely proportional to the capacitor value.

The active filter inductor affects the filtering of the low-frequency components. Figure 9 shows the comparison for 5 mH and 1 mH inductance cases. The upper waveforms (from left to right) are the i_{dc}, v_{bus}, and i_L waveforms with a 5 mH inductor; the lower ones are the corresponding waveforms with 1mH inductance. With a lower inductance, all the current and voltage waveforms show increased low-frequency ripple. The frequency of oscillation is three times the inverter line frequency. This is because the inductance is too small to absorb the low-frequency energy fluctuation generated by the three-phase inverter.

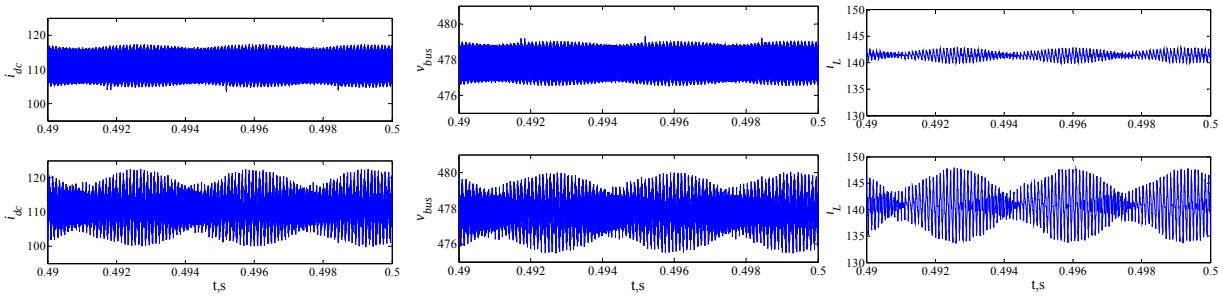

Fig. 9. Effects of filter inductance.

The inductor current should always be designed to be higher than the peak ripple current, since in operation mode 1, the inductor current supports the ripple current and charges the capacitor. However, this inductor current cannot be too large, because it charges or discharges the capacitor. If the charge or discharge is very fast, it will increase the active filter switching frequency.

Conclusion

An APF was developed to replace a dc link capacitor. The simulation of the active filter showed that it functioned as expected, filtering the current ripple in the dc link. The assessment of the simulation and design results can be summarized as follows:

- The APF switching frequency is inversely proportional to the smoothing capacitor size and the dc link voltage ripple hysteresis band limits.
- The dc link voltage ripple hysteresis band limits are directly proportional to the amount of dc current ripple.
- Barriers for practical application and possible solutions include the following:
  - Device losses can be reduced by
    - Using fewer switches and diodes or using a different topology.
    - Reducing the inductor current.
    - Reducing switching frequency.
  - Inductance value and associated inductor size:
    - Inductance value determines how stiff the filter dc current is.
    - Low inductance causes low-frequency voltage ripple. An optimum inductance value is required.

References

1. Bhim Singh, et al., "A review of active filters for power quality improvement," *IEEE Transactions on Industrial Electronics*, **46**(5), 960–972 (October 1999).
2. Fang Z. Peng, "Harmonic sources and filtering approaches," *IEEE Industry Applications Magazine*, 18–25 (July/August 2001).
3. Bimal K. Bose, et al., "Electrolytic capacitor elimination in power electronic system by high frequency active filter," presented at IEEE Industry Applications Society Annual Meeting.

4.3 Advanced Converter Systems for High-Temperature Hybrid Electric Vehicle Environments

Principal Investigator: Leon M. Tolbert
Oak Ridge National Laboratory
National Transportation Research Center
2360 Cherahala Boulevard
Knoxville, TN 37932
Voice: 865-946-1332; Fax: 865-946-1262; E-mail:tolbertlm@ornl.gov

DOE Technology Development Manager: Susan A. Rogers
Voice: 202-586-8997; Fax: 202-586-1600; E-mail: Susan.Rogers@ee.doe.gov

ORNL Program Manager: Mitch Olszewski
Voice: 865-946-1350; Fax: 865-946-1262; E-mail: olszewskim@ornl.gov

---

Objectives

- Develop a high-efficiency bidirectional dc-dc power converter.
- Incorporate high-temperature power devices and capacitors with a high-temperature packaging technology and gate drives that will enable the converters to operate in high-ambient-temperature conditions.

Approach

- Utilize new high-temperature silicon carbide (SiC) power electronics devices with high-temperature capacitors and new high-temperature packaging concepts.
- Develop and incorporate an integrated, silicon-on-insulator (SOI) high-temperature gate drive into the design of the module.

Major Accomplishments

- An SOI gate drive chip with dimensions of 2.2 mm^2 was fabricated and tested at temperatures of up to 225°C.
- A 55 kW, 200 V/600 V multilevel dc-dc converter was fabricated and tested at low temperatures. Efficiency was in the 96 – 98% range.
- High-temperature packaging of SiC junction gate field effect transistors (JFETs) was demonstrated and tested at up to 175°C.

Future Direction

- This project ended September 30, 2008.
- A new project to concentrate on the gate drive design will start October 1, 2008. It will use the results of this project to build a highly integrated SOI gate drive chip that also incorporates protection features.
- High-temperature packaging of SiC power electronic devices will continue under the wide-bandgap project.

Technical Discussion

3X dc–dc Converter Development

The 3X dc–dc converter employs the topology shown in Fig. 1. With proper control, it can provide three different input/output voltage ratios, e.g., 1, 2, or 3 in steady state. Because of its bi-directional nature, the converter can act as a voltage multiplier or a divider based on the definition of source and load.

30 kW Prototype

A 30 kW prototype was fabricated and tested. The film capacitors are mounted on the insulated gate bipolar transistor (IGBT) modules via a 9-layer printed circuit board. Underneath the capacitor board is the gate drive circuit. Control and power supply circuits share the same board with the gate drive circuit. For the controller, the complex logic for duty ratio and frequency control was implemented in one complex programmable logic device (CPLD), Xilinx part number XC9572XLPC44. In addition, a novel clamping circuit represented in Fig. 2 was developed to address the voltage spikes caused by the diode reverse recovery.

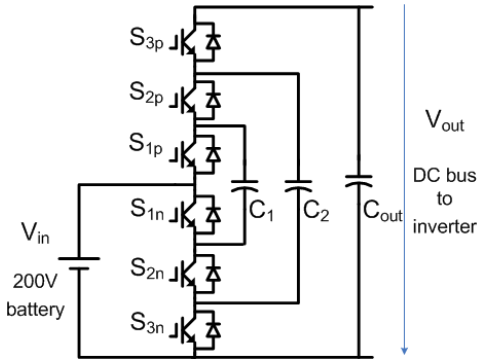

Fig. 1. 3X dc–dc converter topology.

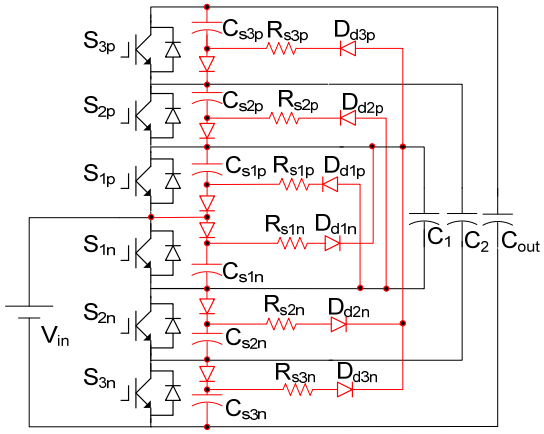

Fig. 2. Topology of the clamping circuit.

System specification and parameters for the 30 kW prototype is as follows:

1. The input voltage range at the low-voltage battery side is 100~200 V. The maximum input voltage under a no-load condition is 200 V.
2. Output power: 30 kW output at the nominal operation voltage of 180 V.
3. Power switching devices: three 250 V, 600 A Powerex CM600DU5F IGBT modules.

Some typical experimental results during steady state operation are shown in Figs. 3 to 6. The capacitors for C_1 and C_2 in Fig. 1 are 500 µF and 160 µF film capacitors. The output capacitor C_{out} consists of a 20 uF capacitor from the 3X dc–dc converter, a 390 uF capacitive load and 0.09 Ω resistor to simulate an inverter load. In the boost mode steady state test, a 1 kHz buck converter is used as an electronic load, which generates 1 kHz load current ripple as seen in Fig. 3(a). The output voltage of the converter is very stable despite the load current ripple. Figure 4 indicates the effectiveness of the clamping circuit. Without the clamping circuit, the converter, restricted by the rated voltage of the IGBT, could handle only around

10 kW output power at 170 V. Figure 5 shows the input and output voltage and current waveforms in 3X buck mode. The efficiency measured by the Yokogawa power meter WT1600 is shown in Fig. 6. The efficiency at 30 kW output in 3X boost mode is 96.8% with a 178 V input voltage and 6.9 kHz switching frequency.

During the transitions when the output voltage ratio changes (such as 2X to 3X or vice versa), the capacitor voltage differences can lead to high transient current through the devices and capacitors. Therefore, a variable pulse width modulation (PWM) duty ratio with high switching frequency is used during transition from one mode to another. Furthermore, a small air-core inductor (3.4 uH) is added when parasitic inductance is not enough for the large voltage difference, and when the adopted devices cannot achieve sufficiently high switching frequency. The converter performance during voltage ratio change transition is shown in Fig. 7. In all cases the transient current is well limited. The periodic peak current in Fig. 7 (a) and (c) is caused by the discrete increment of the duty cycle generated by the CPLD.

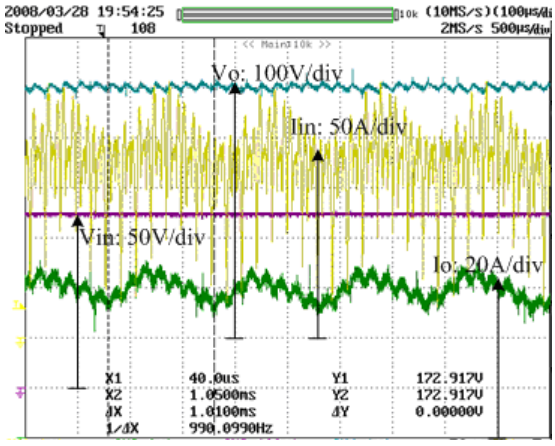

(a) Input and output waveforms

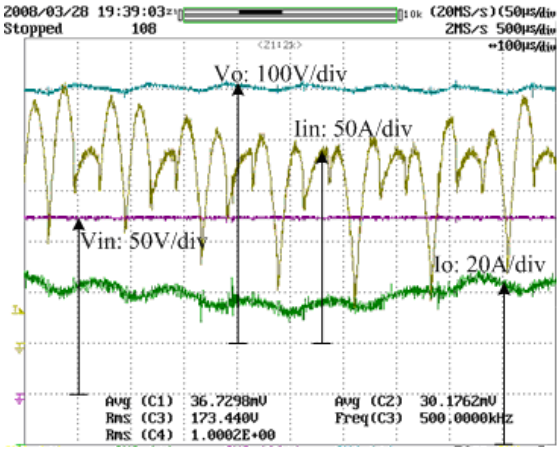

(b) Zoom-in detail

Fig. 3. Input and output voltage and current waveforms of 30 kW output in 3X boost mode.

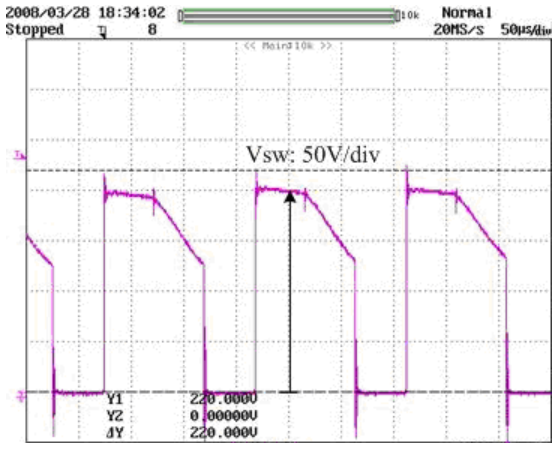

Fig. 4. Highest spike across switch in 30 kW boost mode.

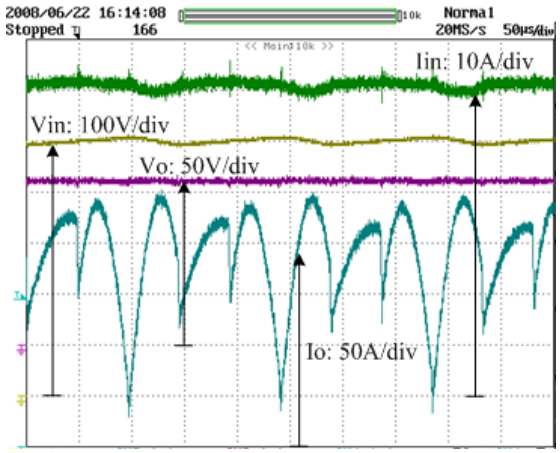

Fig. 5. Input and output voltage and current waveforms for 30 kW output in 3X buck mode.

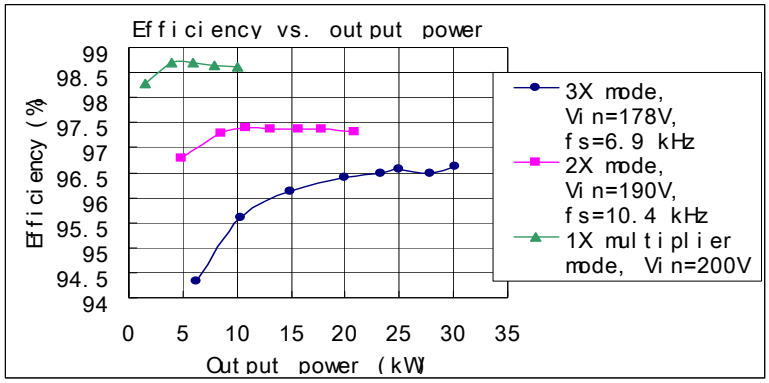

Fig. 6. Efficiency testing results of nX boost mode.

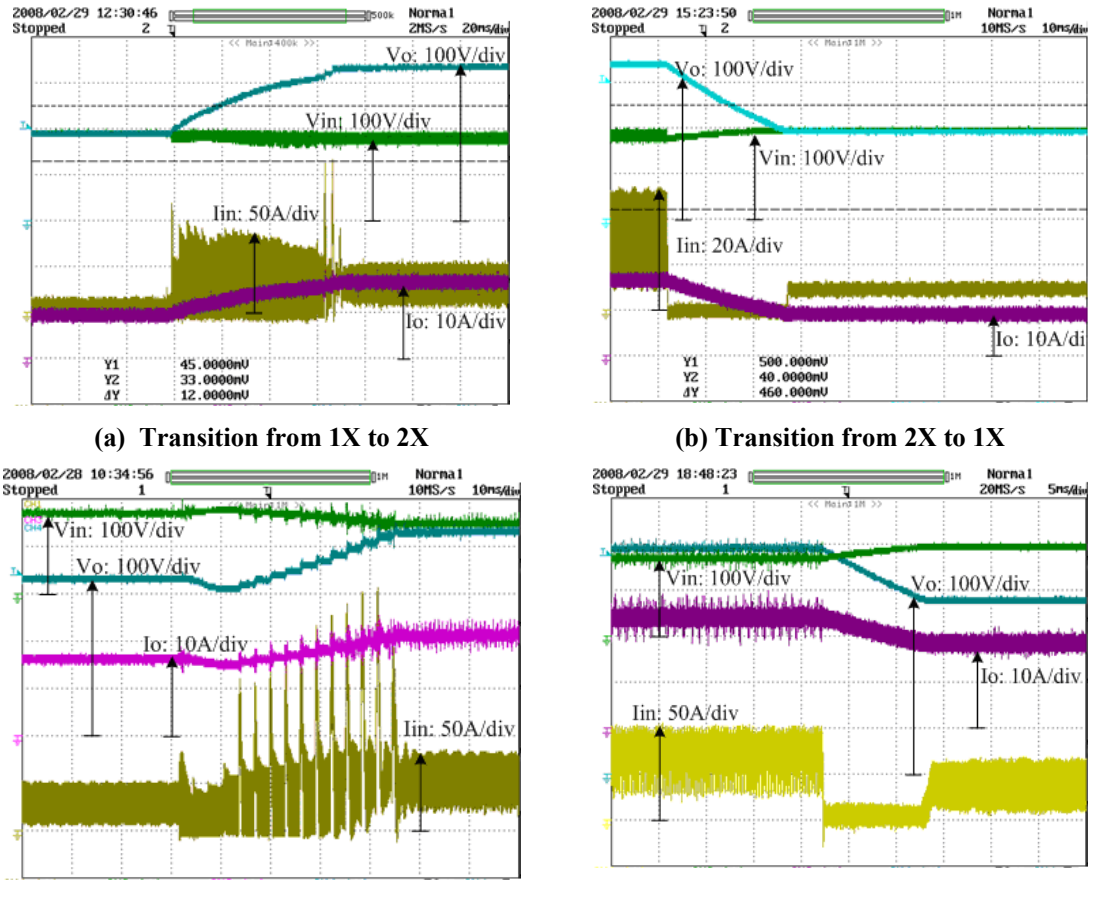

(a) Transition from 1X to 2X

(b) Transition from 2X to 1X

(c) Transition from 2X to 3X

(d) Transition from 3X to 2X

Fig. 7. Experimental results of transient performance test.

55 kW Prototype

A second-generation prototype was built with a wider operating voltage range and higher output power capability. In this prototype, the film capacitors were connected to the intelligent power module by bus bars, as shown in Fig. 8.

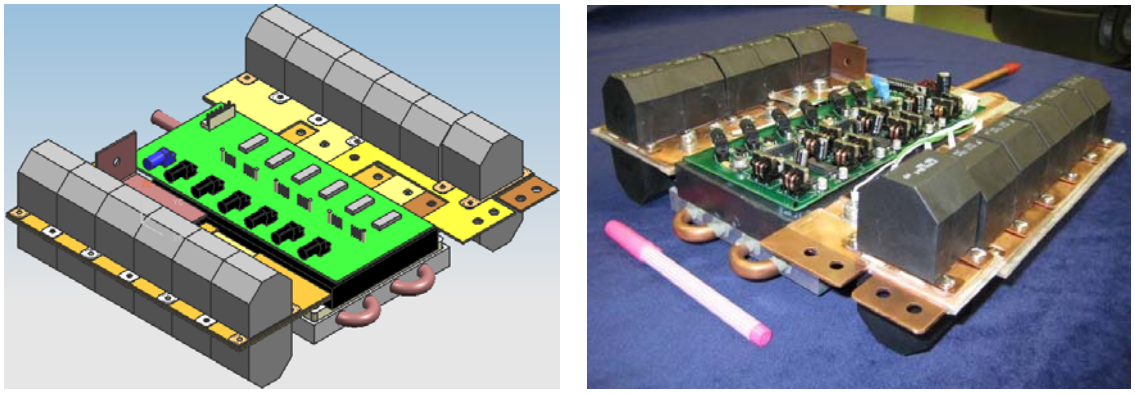

(a) 3-dimensional model **(b) 55 kW prototype.**

Fig. 8. 55 kW prototype.

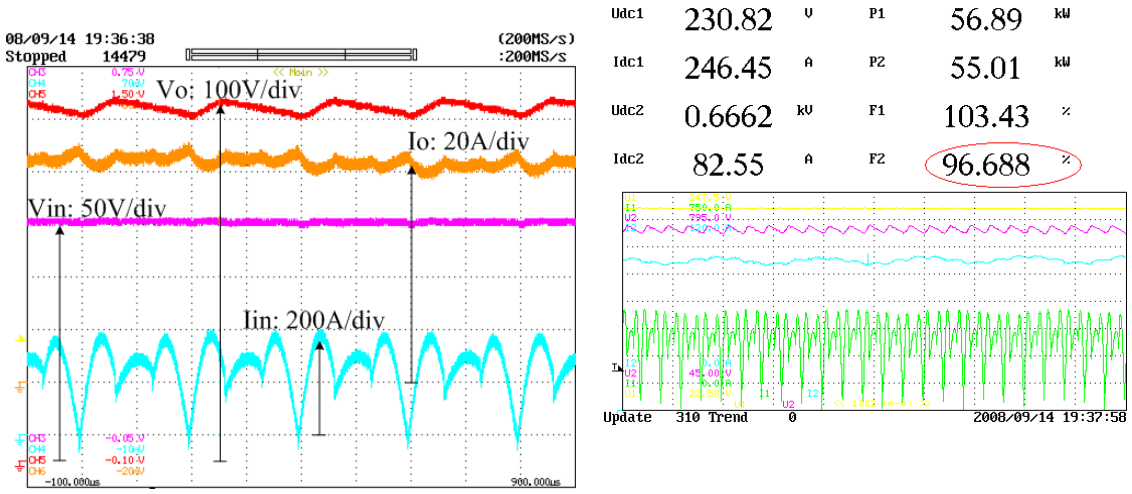

(a) Input and output waveforms **(b) Efficiency data**

Fig. 9. Experimental results at 55 kW output power for second-generation prototype.

The operation condition is specified as follows:

1. Battery side input voltage range: 100~230 V
2. Output power: 30 kW continuous power and 55 kW peak power for 18 s
3. Devices: one 6-pack
4. 600 V, 600 A intelligent power module, Powerex PM600CLA060

The nX boost mode steady state operation was tested on the 55 kW prototype. The waveforms and efficiency at rated power are shown in Fig. 9. The capacitance of C_1 in Fig. 1 is 500 uF, and C_2 is 240 uF. The lumped output capacitor C_{out} in the test is 430 uF. At 5 kHz switching frequency, the measured efficiency is 97.3% at 30 kW continuous power and 96.7% at 55 kW peak power. The optimum switching frequency for this prototype has yet to be determined. For this topology, a higher switching frequency does not necessarily lead to the lower efficiency. At higher frequency, the input current ripple will be lower so that the capacitor charging/discharging loss and the equivalent series resistance (ESR) conduction loss will be reduced. This reduction in loss might be greater than the increase in switching loss at higher switching frequency.

High-temperature gate drive integrated circuit

Figure 10 shows the schematic of the second-generation integrated, high-temperature gate driver circuit designed and fabricated using the Bipolar-complementary metal-oxide semiconductor (CMOS)-double diffused metal-oxide semiconductor (DMOS), or BCD, on-SOI process from Atmel. Compared with the first generation, this version has the additional circuitry of a dead zone generator, a pulse shaper, and an on-chip voltage regulator. A 1.25 nF bootstrap capacitor was also made on-chip. Sizes of the high-voltage negative-channel metal oxide semiconductors (NMOSs) in the half-bridge output stage were increased further to boost the current drive of the circuit. The purpose of these additions and modifications was to achieve higher reliability and to make the driver circuit more integrated.

The high-side and low-side buffers drive the gates of the high-side and low-side high voltage laterally diffused MOSs (M_H and M_L) in the half-bridge output stage, respectively. The bootstrap capacitor (C_B) based charge pump establishes a voltage above the available highest rail voltage (V_{DDH}), which works as a floating battery for the level shifter, SR latch, and high-side buffer. The level shifter converts the incoming digital input signal from the low-side voltage level (V_{DD}) to the high-side voltage level (V_{DDH}). The latch controller generates the appropriate timing pulses (S and R) for the level shifter. *SET* and *RESET* signals from the level shifter controls the SR latch, whose output is passed through the high-side buffer before being applied to the gate of the high-side transistor.

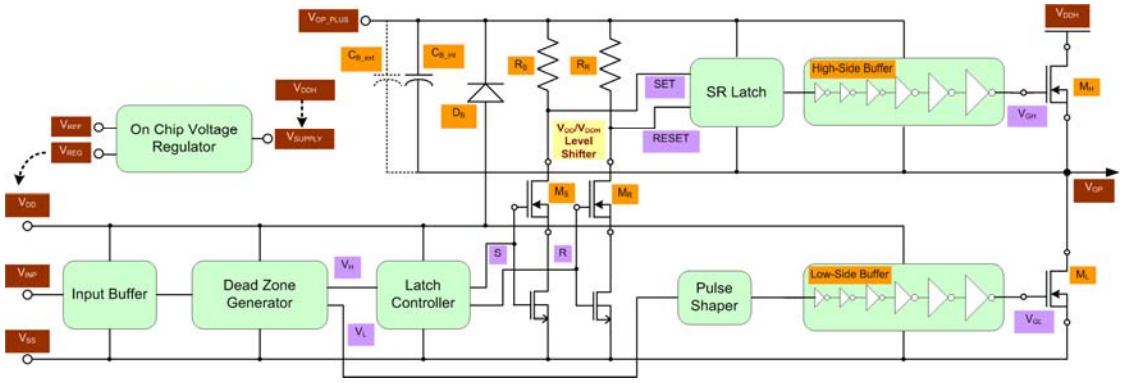

Fig. 10. Schematic of the high-voltage, high-temperature integrated circuit gate driver.

The newly added dead zone generator generates two non-overlapping copies (V_H and V_L) of the incoming logic level input signal. The dead time provided between these two copies ensures the complementary turning ON and OFF of the transistors in the output stage. Since the pulse trains generated by this circuit pass through different circuit paths, an additional pulse shaper circuit is also introduced to further modify the low-side gate signal to ensure complementary switching of the M_H and M_L transistors. Figure 11 shows the schematic of the dead zone generator that uses a circuit topology similar to that of a complementary clock generator with the addition of delay components.

The high-voltage, high-temperature gate driver integrated circuit (IC) was fabricated using 0.8 micron, 3-metal, and 2-poly bipolar complementary MOS and double-diffused MOS (BCD) in an SOI process from Atmel. Figure 12 shows the fabricated chip's microphotograph compared with a dime. This circuit occupies an area of 5 mm^2 (2,240 µm × 2,240 µm) including an on-chip bootstrap capacitor, a voltage regulator, bonding pads, and electrostatic discharge protections. The two high-voltage NMOS devices of the half-bridge output stage occupy a major portion of the chip area. They are sized (W/L = 28,000 µm/1.6 µm) to provide large peak current to obtain shorter rise and fall times. Each of these NMOS transistors comprises seven hundred 45 V NMOS devices (each with W = 40 µm) connected in parallel.

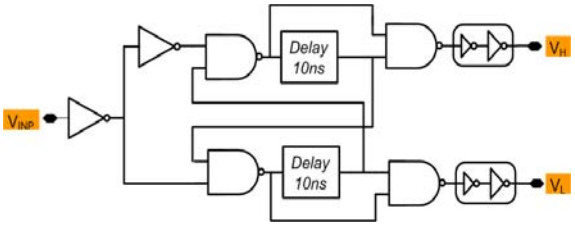

Fig. 11. Dead zone generator circuit.

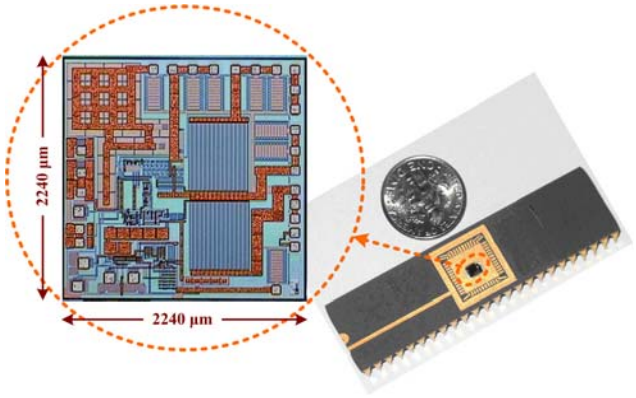

Fig. 12. Microphotograph of the gate driver integrated circuit.

Multiple pad connections are used for the power supply and output nodes to minimize the bond wire's parasitic inductances. All critical metal interconnects are made thick to avoid electromigration, which is a potential failure mechanism at higher temperatures.

High-temperature packaging of the bare dies was developed by both Atmel and Promex; 48-pin dual in-line ceramic packages were used for high-temperature testing. A double-layer PCB was designed to mount the chip and power supply filter networks. These boards were fabricated by Sierra Proto using polyimide material, which can withstand temperatures higher than 200°C. Figure 13 shows one of the test boards used for high-temperature testing of the prototype circuit. High-melting-point solder was used to connect all the components to the PCB. All the connection wires to the PCB used during testing have insulation made of Teflon so that they can safely operate at 200°C. Tantalum capacitors from Kemet (rated for 175°C and 50 V) were used in the test board for power supply filtering. For more reliable testing of the gate driver circuit, capacitors with even higher voltage and temperature ratings are needed.

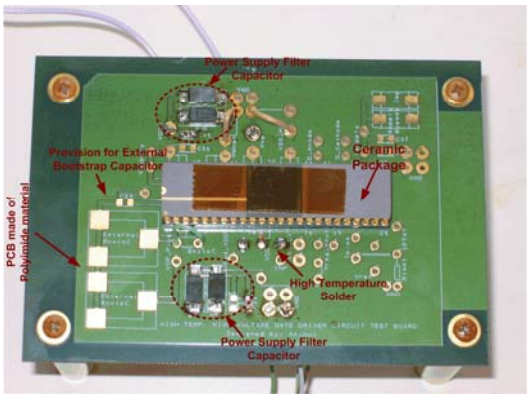

Fig. 13. High temperature test board.

A SiC power metal-oxide semiconductor field-effect transistor (MOSFET) prototype, developed by Cree, was tested with this gate driver chip. An 80 Ω load was used with the SiC MOSFET in a common-source configuration, and the bus voltage was set at 320 V. A 4 A peak load current was passing through the MOSFET when it was turned ON by the gate driver circuit. The test board was placed inside the temperature chamber and the SiC MOSFET kept outside the chamber, as it was not packaged for high-temperature applications. Starting from room temperature, the chip was tested at up to 200°C. Switching frequency was set at 20 kHz and the duty cycle was 10%.

Figure 14 shows the gate voltage (pink), gate drive current (green), and MOSFET drain terminal voltage (blue) and load current (cyan) waveforms at 200°C. The temperature of the chamber was raised from room temperature to 200°C in five steps (85°, 125°, 150°, 175° and 200°C). Figure 14 also shows the time-scale magnified version of the MOSFET switching edges. The ringing effect observed in the wave shapes was due to the added parasitic inductances of the connecting wires that ran from inside the

temperature chamber to the outside. Table 1 records the 10 to 90% rise-time and 90 to 10% fall-time for both the gate drive voltage signal and MOSFET drain voltage at each temperature level. These readings showed that this high-temperature gate driver circuit maintains a fairly constant driving strength over the entire test temperature range.

Table 1. Rise-time and fall-time at different ambient temperatures

Ambient temperature (°C)	Drain voltage (V_{DS})		Gate voltage (V_{GS})	
	t_{rise} (ns)	t_{fall} (ns)	t_{rise} (ns)	t_{fall} (ns)
25	24.1	40.9	42.3	55.6
85	20.9	39.3	42.8	55.6
125	24.8	41.2	43.5	61.1
150	23.5	39.2	43.9	63.7
175	25.2	41.9	43.7	65.5
200	25.1	41.5	43.5	63.3

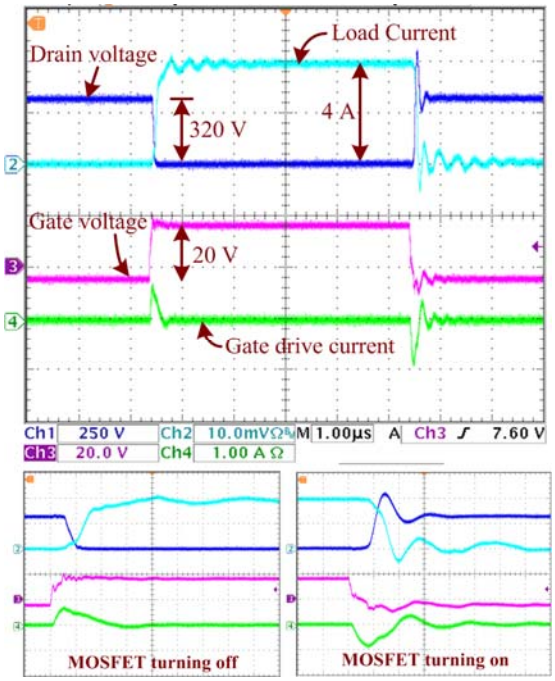

Fig. 14. Prototype circuit's test results at 200°C when driving SiC MOSFET.

This gate driver circuit was also tested with a SiC normally-on JFET from SemiSouth. The prototype gate driver circuit was used to generate a 35 V peak-to-peak (–31.6 V to 3.4 V) gate signal to control the JFET, which was connected to a 160 V bus through a 40 Ω load resistor. Figure 15 shows this test result at room temperature. This driver IC was also tested at up to 200°C with the JFET with the bus voltage set to a relatively low voltage (50 V) and the load resistor at 10 Ω. In both MOSFET and JFET testing, the duty cycle of the logic signal and hence the gate drive signal were also varied from 1 to 99%.

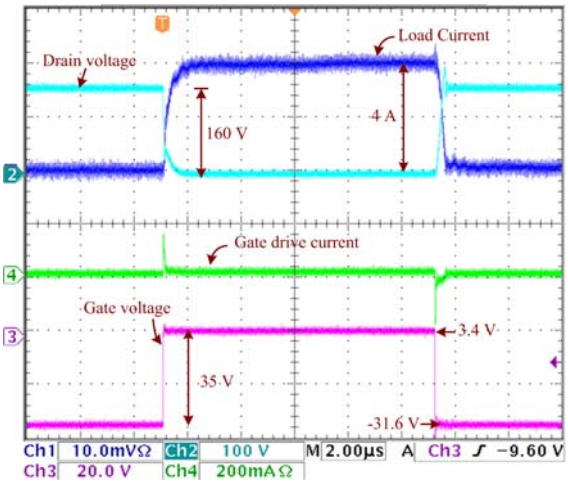

Fig. 15. Prototype circuit's test results at room temperature when driving SiC normally ON JFET.

In this prototype an on-chip voltage regulator (first generation) was included to generate the low bias voltage (V_{DD}) from the high supply voltage (V_{DDH}) to the chip. Depending on the required gate voltage of the SiC power switch that this driver is driving, the V_{DDH} can be set to any value between 15 and 30 V. Hence this regulator needs to work over a wide range of input voltage in addition to maintaining a stable output voltage over a wide temperature range (−50 to 200°C).

A schematic of the low-dropout type of voltage regulator topology used in this work is shown in Fig. 16. This circuit has two distinct building blocks. The first is a bandgap reference (BGR) circuit that generates a constant reference voltage over a wide temperature variation. The second is a single-stage differential amplifier that forms a negative feedback loop with a positive-channel metal-oxide semiconductor (PMOS) pass transistor. A compensation circuit has been added to improve the phase margin of the voltage regulator. The temperature-compensated reference voltage generated by the BGR circuit is used as the reference voltage for the differential input amplifier. The temperature coefficient (TC) of the BGR is minimized by proper weighting of the positive TC of the thermal voltage with the negative TC of the diode forward voltage in the circuit.

Figure 17 shows the regulator output voltage in response to a 15 and 30 V input signal while 4.16 mA peak current is supplied to the load. Figure 17 (inset) also shows the reference voltage generated by the BGR circuit in this test condition. The regulator worked at up to 150°C without any heat sink or cooling. Although the BGR circuit, while tested independently, generated fairly constant voltage up to 200°C, the regulator failed above 150°C. The current driving capability of the regulator circuit needs to be increased to use it with the gate driver circuit. The regulator circuit also needs to be revised and improved to make it work with the gate driver circuit at ambient temperatures of 200°C or more.

A second generation of the high–voltage, high-temperature IC gate driver has been fabricated in the SOI process. This circuit has been tested at high temperatures (≥ 200°C) for several cycles without any cooling. So far no failure or any significant performance deterioration has been observed. This driver circuit has been successfully tested with a SiC MOSFET from Cree and a SiC normally-on JFET from SemiSouth. The duty cycle of the gate drive signal was also varied from 1 to 99%. The bandgap voltage reference (BGR) circuit part of the voltage regulator generated a near constant reference voltage up to 200°C.

However, the complete voltage regulator circuit could not generate 5 V above 150°C. (Note that the voltage regulator circuit was a first generation circuit on the second generation chip—the first generation chip did not have a voltage regulator circuit).
Knowledge learned from this design will be used to design a newer version of the regulator circuit.

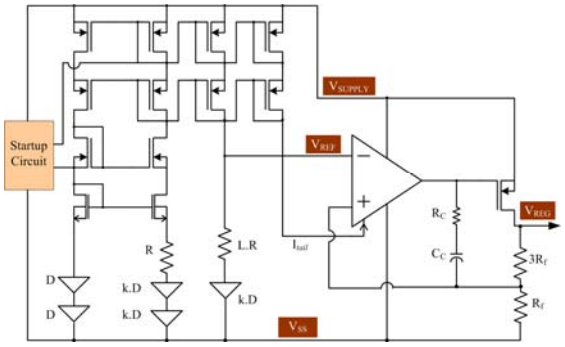

Fig. 16. Schematic of the first-generation on-chip voltage regulator circuit.

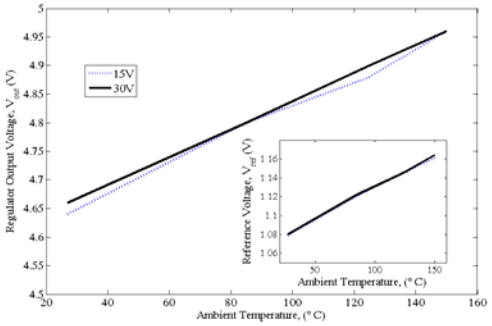

Fig. 17. Regulator test result (up to 150°C) with 4.26 mA peak load current.

This SOI-based driver IC can be used for both SiC MOSFETs and JFETs and in any power electronics modules in which ambient temperature is higher than 125°C, which is the typical maximum operating range of bulk Si-based gate drivers. The SOI-based high temperature-gate driver IC will extend to the system level the advantages of high-temperature capabilities provided by wide-bandgap power devices such as SiC-based power FETs.

Some of the features of the integrated SOI gate drive are:

- Built using the advantages of BCD on SOI processes
- High source and sink current capability: peak 2.3 A @ 27°C and 1.7 A @ 200°C ambient
- Gate drive supply range from 10 to 40 V p-p
- High operating temperature: 200°C ambient without any cooling mechanism
- High capacitive load drive capability: 10 nF in <100ns @ 200°C
- Integrated bootstrap diode and capacitor
- Low supply current
- Built-in dead-time control function
- Output in phase with the input

High-temperature packaging

Several SiC JFET samples packaged for operation in ambient temperatures of up to 175°C ambient were obtained from SiCED (Germany), tested, and characterized. The SiCED SiC JFET had a voltage rating of 1200 V and an on resistance of 150 mΩ@1A.

The devices were placed in an environmental chamber to raise the ambient temperature from 25°C up to 175°C in 25°C increments. The static characteristics of the SiC JFET are shown in Fig. 18. The on-state resistance of the SiC JFET increased with temperature, while the transfer characteristic changed only slightly for the temperatures used in the tests.

The switching energy losses at different temperatures and current levels are shown in Fig. 19; they increased with current and did not change much with temperature. A custom gate drive PCB for double

pulse switching was designed, fabricated, and populated. The commercial gate driver IC HCNW3120 was used to drive the SiC JFET. The gate voltage was 0 V for "turn on" and −15 V for "turn off".
Figure 19 shows that the switching loss in the SiC JFET is almost independent of temperature for the 25 to 175°C region. It also shows that the transfer characteristic (gate voltage requirement) is nearly independent of temperature. However, the on-state resistance does increase with temperature, but this will allow the devices to be paralleled.

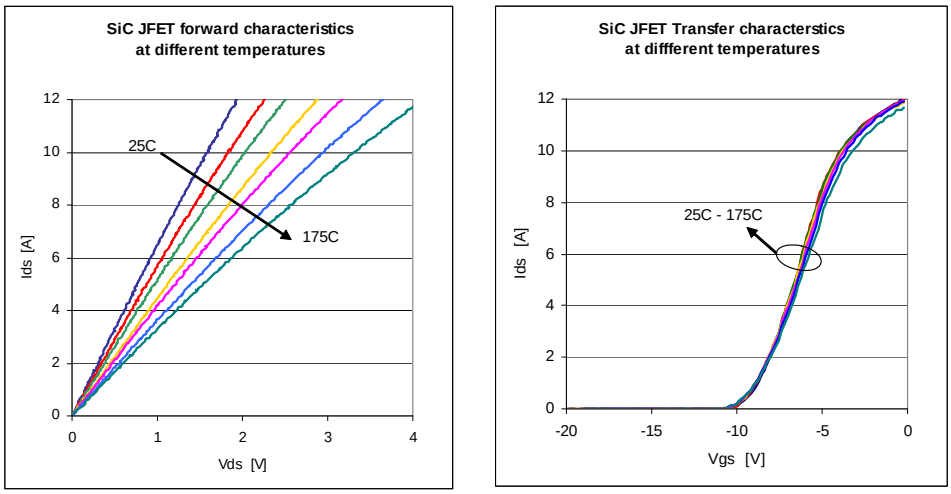

(a) Forward characteristics (I-V curve) **(b) Transfer characteristics**

Fig. 18. Static characteristics of the SiC JFET (SiCED, 1200 V, 150 mΩ).

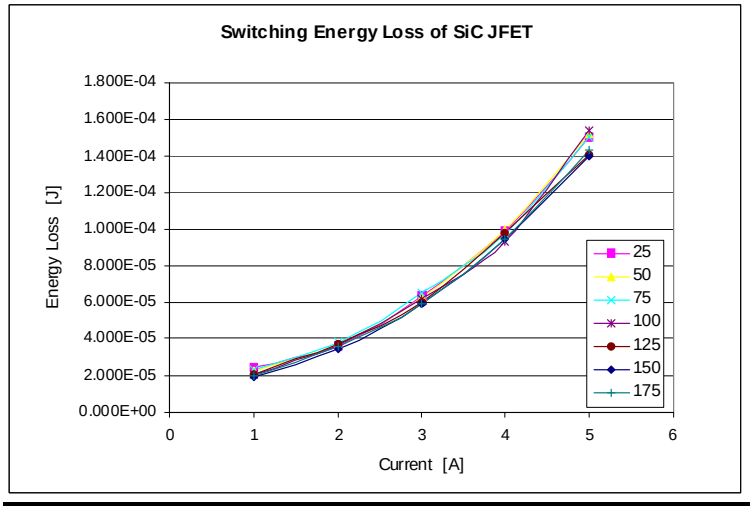

Fig. 19. Switching loss of the SiC JFET vs. current at different temperatures.

Conclusion

This challenging project involves the development and demonstration of several novel technologies in order to achieve a converter that can operate at high ambient temperatures. Novel magnet-less or small magnetic dc-dc converter topologies will result in reduced volume and weight compared with

conventional topologies. The multilevel design of these converters will also allow segregation of the battery pack into multiple modules. This will allow replacement of only a portion of the battery pack in case of failure. It may also result in an increase in reliability and availability of the battery power, as the converter designs will allow for a damaged or failed battery module or power electronics module to be bypassed.

A high-temperature gate drive has been fabricated in SOI and tested at high temperatures. This design shows great promise for allowing the gate drive to be located near high-temperature power electronics with no cooling. SiC JFETS show switching loss and transfer characteristics to be independent of temperature and the ability to operate at high ambient temperatures. Slow progress in SiC switching transistors (JFETs) and high-temperature capacitors has hampered this project, but it has nonetheless demonstrated several valuable technologies for future hybrid electric vehicles. Gains made from this project will likely impact other power electronics projects that need high-temperature packaging, gate drives, or modular conceptual designs.

Publications

1. M. A Huque, S. K. Islam, B. J. Blalock, C. Su, R. Vijayaraghavan, and L. M. Tolbert, "Silicon-on-insulator based high-temperature electronics for automotive applications," in *IEEE International Symposium on Industrial Electronics*, Cambridge, England, June 30–July 2, 2008.
2. M. A Huque, B. J. Blalock, C. Su, R. Vijayaraghavan, S. K. Islam, and L. M. Tolbert, "SOI-based integrated circuits for high-temperature applications," in *IMAPS International Conference on High Temperature Electronics*, Albuquerque, New Mexico, May 12–15, 2008.
3. M. Shen, F. Z. Peng, and L. M. Tolbert, "Multilevel DC-DC power conversion system with multiple DC sources," *IEEE Transactions on Power Electronics* **23**(1), 420–426 (January 2008).
4. F. Khan and L. M. Tolbert, "A multilevel modular capacitor clamped DC-DC converter," *IEEE Transactions on Industry Applications* **43**, 1628–1638 (November/December 2007).
5. F. H. Khan and L. M. Tolbert, "Generating isolated outputs in a multilevel modular capacitor clamped DC-DC converter (MMCCC) for hybrid electric and fuel cell automotives," pp. 967–973 in *IEEE Power Electronics Specialists Conference*, Rhodes, Greece, June 15–19, 2008.
6. F. H. Khan and L. M. Tolbert, "A universal multilevel DC-DC converter with variable conversion ratio and high component utilization," pp. 17–23 in *IEEE Applied Power Electronics Conference*, Austin, Texas, February 24–28, 2008.
7. L. M. Tolbert, H. Zhang, M. S. Chinthavali, and B. Ozpineci, "SiC-based power converters for high temperature applications," *Materials Science Forum* **556–557**, 965–970 (2007).

4.4 Current Source Inverter

Principal Investigator: Gui-Jia Su
Oak Ridge National Laboratory
National Transportation Research Center
2360 Cherahala Boulevard
Knoxville, TN 37932
Voice: 865-946-1330; Fax: 865-946-1262; E-mail: sugj@ornl.gov

DOE Technology Development Manager: Susan A. Rogers
Voice: 202-586-8997; Fax: 202-586-1600; E-mail: Susan.Rogers@ee.doe.gov

ORNL Program Manager: Mitch Olszewski
Voice: 865-946-1350; Fax: 865-946-1262; E-mail: olszewskim@ornl.gov

---

Objectives

- Overall project objectives
  - Eliminate the drawbacks of the voltage source inverter (VSI) by switching to a current-source–based topology.
  - Reduce inverter cost and volume by 25% compared with the Toyota Prius inverter.
  - Improve inverter and motor lifetime.
  - Increase motor efficiency (10% loss reduction).
  - Increase constant-power speed range.
  - Reduce the cost and size of batteries in plug-in hybrid electric vehicles (HEVs).
  - Enable silicon carbide (SiC) -based inverters to operate in elevated-temperature environments.
- Objectives for FY 2008 effort
  - Design, fabricate and test a 55 kW prototype with a voltage boost ratio of 3, a reduction in motor voltage harmonic distortion and bearing leakage current of 90%, and a reduction in capacitor requirements from 2,000 to 200 μF.

Approach

- Finalize the inverter design developed in FY 2007.
- Fabricate a prototype of a 55 kW current source inverter (CSI) based on the design specifications.
- Develop digital signal processing (DSP) code to implement the control algorithms.
- Test and evaluate the prototype against the technical performance goals.

Major Accomplishments

- A 55 kW prototype was designed, fabricated and successfully tested.
- Total capacitance was reduced to 195 μF.
- Test results confirmed a voltage boost ratio of up to 3.47.
- An output voltage total harmonic distortion factor lower than 12.5% was achieved.
- Measured motor leakage current at each motor terminal voltage was as low as 1.146 mA/V.

Future Direction

- Design, fabricate, and test a 55 kW prototype that can operate with a 105°C coolant.

Technical Discussion

Background

Current electric and hybrid electric vehicles (EVs/HEVs) use inverters that operate off a voltage source. They are called VSIs (Fig. 1a) because the most readily available and efficient energy storage devices, batteries, are inherently voltage sources. The VSI, however, possesses several drawbacks that make it difficult for it to meet FreedomCAR goals for volume, lifetime, and cost for an inverter operating with a high-temperature (105°C) coolant. A VSI requires a very-high-performance dc bus capacitor to maintain a near-ideal voltage source. Also, currently available capacitors that can meet the demanding requirements are costly and bulky, taking up one-third of the inverter volume and cost. The reliability of the inverter is also limited by the capacitors and further hampered by the possible shoot-throughs of the phase legs making up a VSI (S_1-S_2, S_3-S_4, and S_5-S_6 in Fig. 1a). In addition, steep rising and falling edges of the output voltage in the form of pulse trains generate high electromagnetic-interference (EMI) noises, impose high stress on the motor insulation, and produce high-frequency losses in the copper windings and iron cores of the motor, as well as generate bearing-leakage currents that erode the bearings over time.

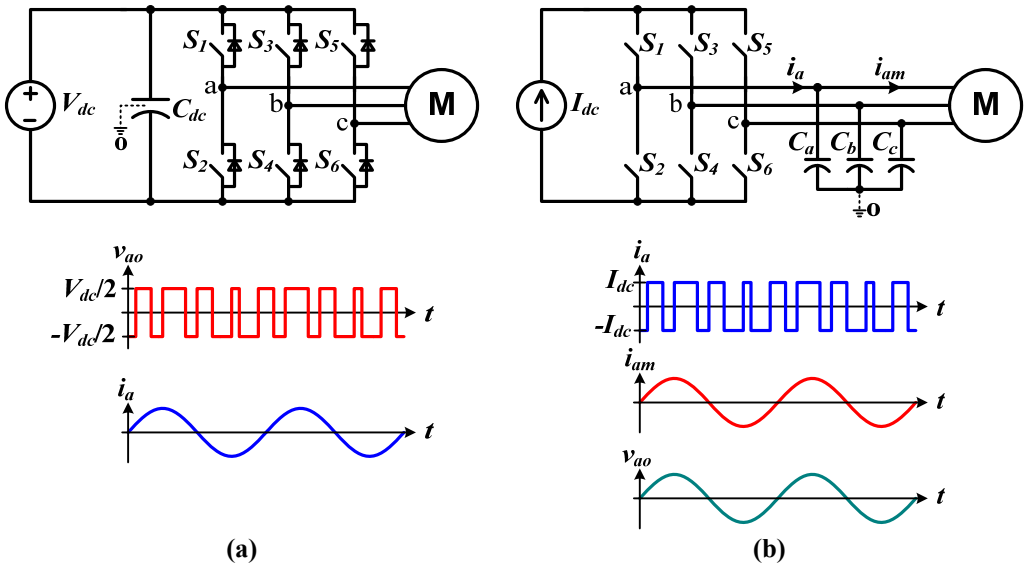

Fig. 1. Schematics of the two types of inverters and typical output voltage and current waveforms: (a) the voltage source inverter and (b) the current source inverter.

As the maximum operating junction temperature of the latest silicon insulated gate bipolar transistors (IGBTs) increases, the capacitor, in fact, presents the most difficult hurdle to operating a VSI in automotive high-temperature environments. The function of the dc bus capacitor is twofold: (1) to maintain a near-ideal voltage source and (2) to absorb the ripple current generated by the switching actions of the inverter.

The root mean square value of the ripple current is proportional to the motor current with a maximum ratio of 50~60%, depending on the pulse-width modulation (PWM) scheme. Currently, two types of dielectrics, polymer film and ceramics, are being pursued for use in high-temperature environments. The polymer-film capacitor is the choice of capacitor technology for HEVs currently on the market because of its benign failure mode and adequate ripple-current handling capability at a lower coolant temperature (about 70°C); however, its ripple-current handling capability rapidly diminishes as the temperature increases. As a result, a significantly larger capacitor would be required in the higher operating temperature environment. On the other hand, although ceramic capacitors can still provide adequate

ripple-current capability even at higher temperatures, their tendency to produce catastrophic failures and their higher cost have made them unacceptable for HEV applications.

In addition, for the VSI to operate from a low-voltage battery, a bidirectional dc-dc converter is needed. Figure 2 shows a widely used inverter topology with such a converter, where two additional IGBTs and an inductor are used for interface with a low-voltage battery.

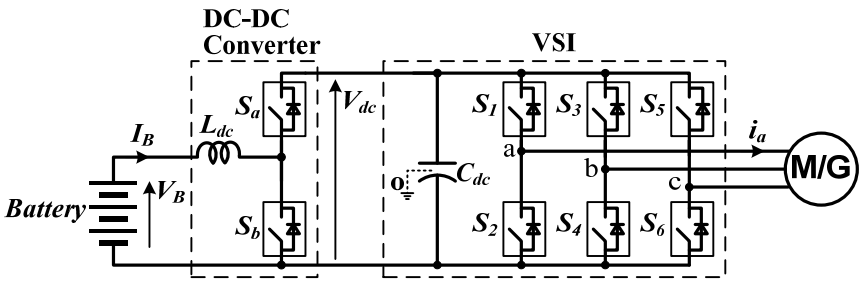

Fig. 2. A voltage source inverter with a bidirectional dc-dc converter for interfacing with a low-voltage battery.

All these problems can be eliminated or significantly reduced by the use of another type of inverter, the current source inverter (CSI) (Fig. 1b). The CSI requires no dc bus capacitors and uses only three alternating-current (ac) filter capacitors of a much smaller capacitance. The total capacitance of the ac filter capacitors is estimated at approximately one-fifth that of the dc bus capacitance in the VSI. In addition, the CSI offers many other advantages important for EV applications: (1) it does not need antiparallel diodes in the switches, (2) it can tolerate phase-leg shoot-throughs, (3) it provides sinusoid-shaped voltage output to the motor, and (4) it can boost the output voltage to a higher level than the source voltage to enable the motor to operate at higher speeds. These advantages could translate into a significant reduction in inverter cost and volume with increased reliability, a much higher constant-power speed range, and improved motor efficiency and lifetime.

Two factors, however, have so far prevented the application of CSIs in HEVs. The first is the difficulty of incorporating batteries into a CSI as energy-storage devices; the second is the limited availability of power switches that can block voltages in both forward and reverse directions. IGBTs with reverse-blocking capability are being offered as engineering samples, and the technology is rapidly reaching the maturity needed for commercial production. This research aims to remove the remaining hurdles and bring the advantageous CSI to HEV applications by offering a new inverter topology based on the CSI but with a novel scheme to incorporate energy-storage devices. By significantly reducing the amount of capacitance required, the CSI-based inverter with silicon IGBTs will be able to substantially decrease the requirements for cooling systems and, further, could enable air-cooled power inverters in the future when SiC-based switches become commercially viable.

The overall objective of the research is to design, fabricate, test, and evaluate a 55 kW inverter prototype based on the novel CSI topology to replace the VSI for EV and HEV applications. Three major tasks will be carried out over a 3-year period: (1) modeling and simulation, (2) design and fabrication of a 55 kW prototype, and (3) testing and evaluation. In FY 2007, computer modeling and simulation was conducted to down-select an optimal interfacing circuit, followed by production of a conceptual design of a 55 kW inverter system. Building on the FY 2007 activities, a 55 kW prototype was be designed, fabricated, and tested in FY 2008 to provide data for performance analysis.

Description of the proposed current source inverter

Figure 3 shows a schematic of the proposed CSI with a battery-interfacing circuit. The interfacing

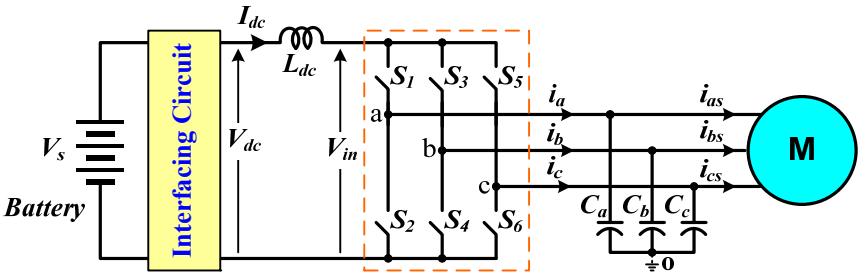

Fig. 3. Schematic of the proposed current source based inverter.

circuit—with the help of the dc choke, L_{dc}—transforms the voltage source of the battery into a current source to the inverter bridge by providing the capability to control and maintain a constant dc bus current, I_{dc}. More important, the interfacing circuit also enables the inverter to charge the battery during dynamic breaking without the need for reversing the direction of the dc bus current.

Whereas the VSI produces a voltage pulse train, the CSI generates a current pulse train in each phase output by turning on and off the switches, S_1-S_6, in the bridge according to a PWM strategy. The pulsed phase currents are then filtered by a simple filter network of the three capacitors, C_a, C_b, and C_c, leaving near sinusoidal currents as well as sinusoidal voltages to the electrical motor. The sinusoidal voltages are desirable for the motor because they eliminate problems with the VSI output voltages. These include pulse trains with steep rising and falling edges, which generate high EMI noises imposing high stresses on the motor insulation, and producing high-frequency losses in the copper windings and iron cores of the motor as well as generating bearing-leakage currents.

An ac generator driven by an internal combustion engine could also be incorporated into the inverter system for hybrid vehicles.

Generally, modulation schemes can be categorized into two main groups: carrier-based and space vector schemes. Because of the duality between the VSI and CSI, it is possible to translate the modulation schemes between the two types of inverters. Switching tables of the VSI and the CSI are given in Table 1 and Table 2, respectively. The space vector diagrams are given in Fig. 4.

Table 1. Switching table of the VSI

	Top devices			Bottom devices			Phase voltages		
	S_1	S_3	S_5	S_2	S_4	S_6	V_{ao}	V_{bo}	V_{co}
V_0	0	0	0	1	1	1	0	0	0
V_1	1	0	0	0	1	1	V_{dc}	0	0
V_2	1	1	0	0	0	1	V_{dc}	V_{dc}	0
V_3	0	1	0	1	0	1	0	V_{dc}	0
V_4	0	1	1	1	0	0	0	V_{dc}	V_{dc}
V_5	0	0	1	1	1	0	0	0	V_{dc}
V_6	1	0	1	0	1	0	V_{dc}	0	V_{dc}
V_7	1	1	1	0	0	0	V_{dc}	V_{dc}	V_{dc}

Table 2. Switching table of the CSI

	Top devices			Bottom devices			Phase currents		
	S_1	**S_3**	**S_5**	**S_2**	**S_4**	**S_6**	i_a	i_b	i_c
I_1	1	0	0	0	0	1	I_{dc}	0	$-I_{dc}$
I_2	0	1	0	0	0	1	0	I_{dc}	$-I_{dc}$
I_3	0	1	0	1	0	0	$-I_{dc}$	I_{dc}	0
I_4	0	0	1	1	0	0	$-I_{dc}$	0	I_{dc}
I_5	0	0	1	0	1	0	0	$-I_{dc}$	I_{dc}
I_6	1	0	0	0	1	0	I_{dc}	$-I_{dc}$	0
I_7	1	0	0	1	0	0	0	0	0
I_8	0	1	0	0	1	0	0	0	0
I_9	0	0	1	0	0	1	0	0	0

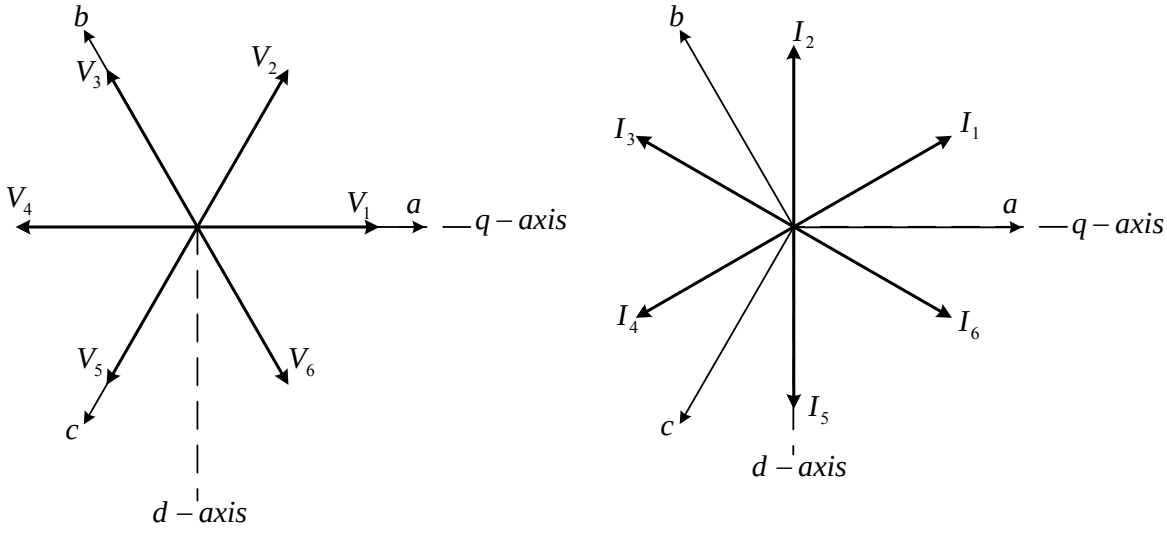

Fig. 4. Space vector diagrams for the VSI (left) and CSI (right).

The voltage vector of the VSI is mapped to the current vector of the CSI according to the following rules:

$$\begin{aligned} &V_1 \to I_6 \qquad V_2 \to I_1 \\ &V_3 \to I_2 \qquad V_4 \to I_3 \\ &V_5 \to I_4 \qquad V_6 \to I_5 \end{aligned} \tag{1}$$

The switching functions of the CSI can then be mapped from that of the VSI by

$$\begin{aligned} &S_{1i} = S_{1v} \cdot S_{6v} + S_{0i} \qquad S_{3i} = S_{3v} \cdot S_{2v} + S_{0i} \\ &S_{5i} = S_{5v} \cdot S_{4v} + S_{0i} \qquad S_{2i} = S_{2v} \cdot S_{5v} + S_{0i} \\ &S_{4i} = S_{4v} \cdot S_{1v} + S_{0i} \qquad S_{6i} = S_{6v} \cdot S_{3v} + S_{0i} \end{aligned} \tag{2}$$

where the subscript "*v*" represents the switching function of the VSI and the subscript "*i*" represents that of the CSI; S_{0i} represents the zero sequence states of the CSI, I_7, I_8 and I_9. The zero sequence signals are there to balance the on time intervals for the switches and will not affect the fundamental component; however, they can be used to minimize the switching losses. Table 3 gives the optimal zero sequence for each switching state.

Table 3. Optimal zero sequence

Current active vector	Next active vector	Sector	Optimal zero sequence
I_6	I_1	I	I_7
I_1	I_2	II	I_9
I_2	I_3	III	I_8
I_3	I_4	IV	I_7
I_4	I_5	V	I_9
I_5	I_6	VI	I_8

It should be noted that because of the phase angle difference between the voltage vectors and the current vectors, the direct mapping of the space vectors of the VSI to those of the CSI produces a 30° phase shift between the output current and the reference current.

The triangle carrier-based modulation produces two active zones, each composed of two active states arranged with different sequences. Zero states are located at both the beginning and the end of each active zone. The sawtooth carrier-based modulation, on the other hand, removes the zero state between the two active zones and combines the two active zones into one. Therefore, the latter may further reduce the amount of device switching over a switching cycle.

Space vector PWM is another attractive method for digital control because of its inherent advantage of enabling direct calculations in the *qd* reference frame and straightforward implementation in digital controllers. The space vector modulation methodology of a VSI can also be adapted to a CSI. The goal is to optimally use the three variables—two active vectors "a" and "b" and a zero vector—to generate the desired current vector. The process of implementation can be divided into three steps: (1) transformation of the commands from the abc stationary reference frame to the q-d stationary reference frame, (2) calculation of the time intervals of the vectors "a" and "b", and (3) generation of modulation signals based on the time intervals. Table 4 gives the normalized time interval for the two active and zero vectors for each sector.

The carrier-based PWM scheme can be realized by direct mapping from VSI counterparts and is thus simple and easy to implement with analog circuits. The active state intervals are calculated indirectly, and the sequence and ordering of the active states are implicit for the carrier-based PWM schemes; however, with the space vector PWM algorithm, the sequence, the ordering, and the period of the active states are all explicitly computed. Moreover, the sequence of the active states and null state can be arranged arbitrarily as long as the total time period for each switching cycle meets the desired value. The space vector PWM algorithm is therefore good for digital control and will be used in prototype development.

Table 4. Normalized time intervals for the two active and zero vectors for each sector

Sector	First active vector (t_α)	Second active vector (t_β)	Zero vector (t_0)
I	$-\frac{i_c}{I_{dc}}$	$-\frac{i_b}{I_{dc}}$	$1-\frac{i_a}{I_{dc}}$
II	$\frac{i_b}{I_{dc}}$	$\frac{i_a}{I_{dc}}$	$1+\frac{i_c}{I_{dc}}$
III	$-\frac{i_a}{I_{dc}}$	$-\frac{i_c}{I_{dc}}$	$1-\frac{i_b}{I_{dc}}$
IV	$\frac{i_c}{I_{dc}}$	$\frac{i_b}{I_{dc}}$	$1+\frac{i_a}{I_{dc}}$
V	$-\frac{i_b}{I_{dc}}$	$-\frac{i_a}{I_{dc}}$	$1-\frac{i_c}{I_{dc}}$
VI	$\frac{i_a}{I_{dc}}$	$\frac{i_c}{I_{dc}}$	$1+\frac{i_b}{I_{dc}}$

Modeling and control of the current source inverter

Assume the interface circuit generates the output voltage, V_{dc}, proportional to the input voltage, V_s, i.e.,

$$V_{dc} = M_{dc} \cdot V_s , \tag{3}$$

where M_{dc} is a control signal. The CSI switch network can be modeled by

$$i_a = S_1 \cdot I_{dc} - S_2 \cdot I_{dc}, \quad i_b = S_3 \cdot I_{dc} - S_4 \cdot I_{dc}, \quad i_c = S_5 \cdot I_{dc} - S_6 \cdot I_{dc} . \tag{4}$$

The ac filter capacitors and dc link inductor can be described by Eqs. (5) and (6), respectively.

$$Cdv_{ao} / dt = i_a - i_{as}, \quad Cdv_{bo} / dt = i_b - i_{bs}, \quad Cdv_{co} / dt = i_c - i_{cs} ; \tag{5}$$

$$L_{dc} pI_{dc} = V_{dc} - V_{in} . \tag{6}$$

The input voltage, V_{in} can be calculated from the switching functions and the ac capacitor voltages as

$$V_{in} = v_{ao}(S_1 - S_2) + v_{bo}(S_3 - S_4) + v_{co}(S_5 - S_6) . \tag{7}$$

The equivalent circuit of the CSI, which is essentially a boost converter, is shown in Fig. 5, in which the switching device *G* represents the switches of the CSI while the RL load represents a motor.

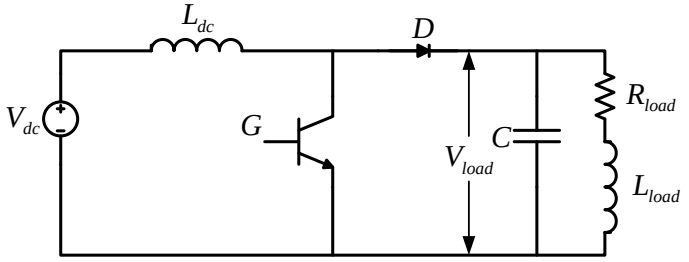

Fig. 5. Equivalent circuit of the CSI for voltage boosting.

The input and output voltages of the boost converter are related by

$$\frac{V_{load}}{V_{dc}} = \frac{1}{1 - D_{on}}, \quad (8)$$

where D_{on} is the duty ratio of the switching device G. The duty ratio is equal to the shoot-through ratio and can be found for balanced three-phase stator currents by

$$D_{on} = 1 - \frac{3}{\pi} M, \quad (9)$$

where M is the modulation index for the CSI. Equation (8) can be expressed as

$$V_{load} = \frac{\pi}{3M} V_{dc}. \quad (10)$$

It is now apparent from Eq. (10) that the load voltage increases when the magnitude of the modulation index decreases. When the desired output currents are given, the multiplication of the dc link current and the modulation signals is fixed. Hence, if the modulation signals decrease, the dc link current needs to be increased to track the desired output phase current.

Prototype and experimental results

A conceptual design of a 55 kW current source inverter was carried out in FY 2007 based on the simulation study. The design was finalized in FY 2008 and a prototype was fabricated according to the design specifications. Since the CSI requires IGBTs that can block voltages in both forward and reverse directions, and since those IGBTs were not available at the required voltage and current ratings, we designed custom modules comprised of an IGBT and a diode connected in series. We contracted with a power device manufacturer to produce the quantities needed for prototype development. Figure 6 shows photos of the prototype. The total amount of capacitance is 195 μF, compared with the 2000 μF required in a typical 55 kW VSI.

The prototype was tested with a resistive load to measure the voltage boost factor and output voltage harmonic distortion. Figure 7 plots the measured voltage boost ratio vs inverter duty cycle. The boost ratio increases as the duty cycle decreases. The measured ratio at a duty cycle of 0.35 is 3.47. Figures 8 and 9 illustrate waveforms in boost mode at voltage ratios of 2.67 and 1.35, respectively. With the help of the interfacing circuit, the CSI can also operate in buck mode to decrease the output voltage. Figure 10 shows waveforms in the buck mode at a voltage ratio of 0.67. Table 5 gives measured output voltage total harmonic distortion factor (THD) at several load power points.

The prototype was then tested with an induction motor to assess the motor bearing leakage current. Figure 11 shows test waveforms acquired during testing. The measured leakage current is 0.319A, resulting in a line-to-line motor terminal voltage value of 1.146 mA/V.

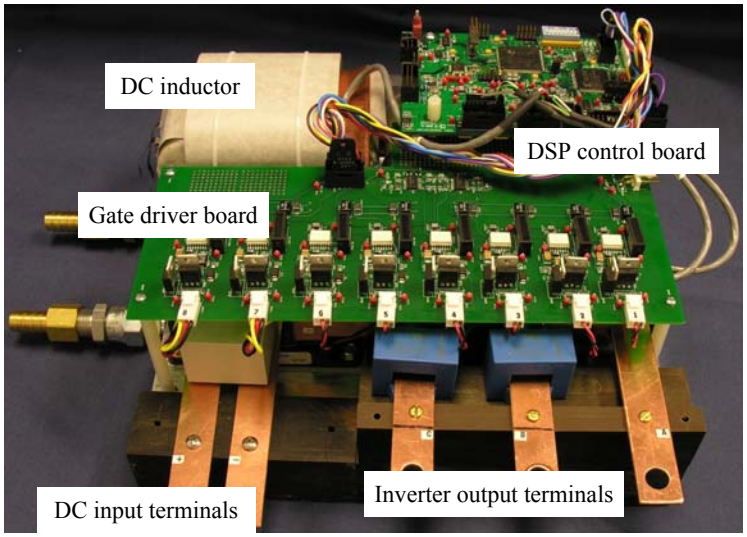

(a) Front view

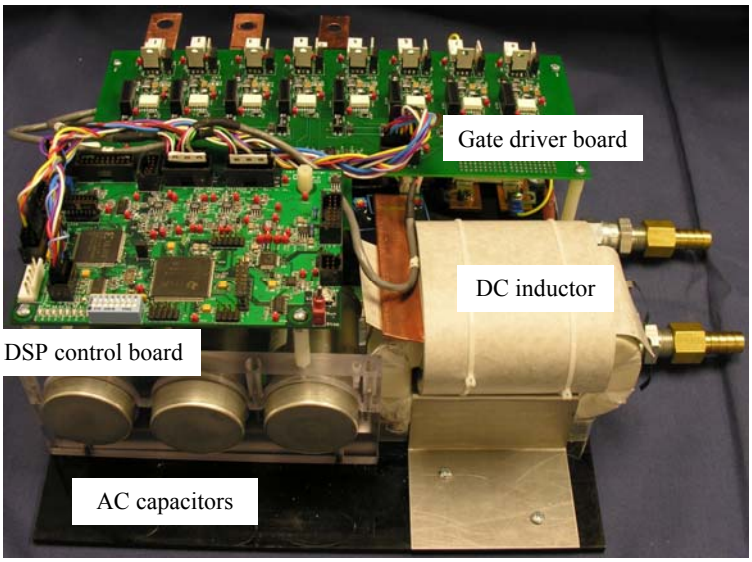

(b) Rear view

Fig. 6. A photo of the 55 kW prototype. Heat sink footprint: 8 in. width × 11 in. depth.

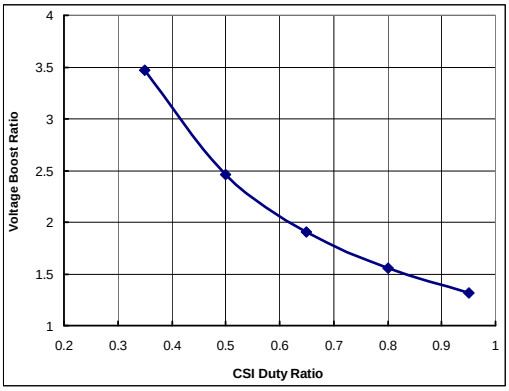

Fig. 7. Measured voltage boost ratio vs inverter duty cycle.

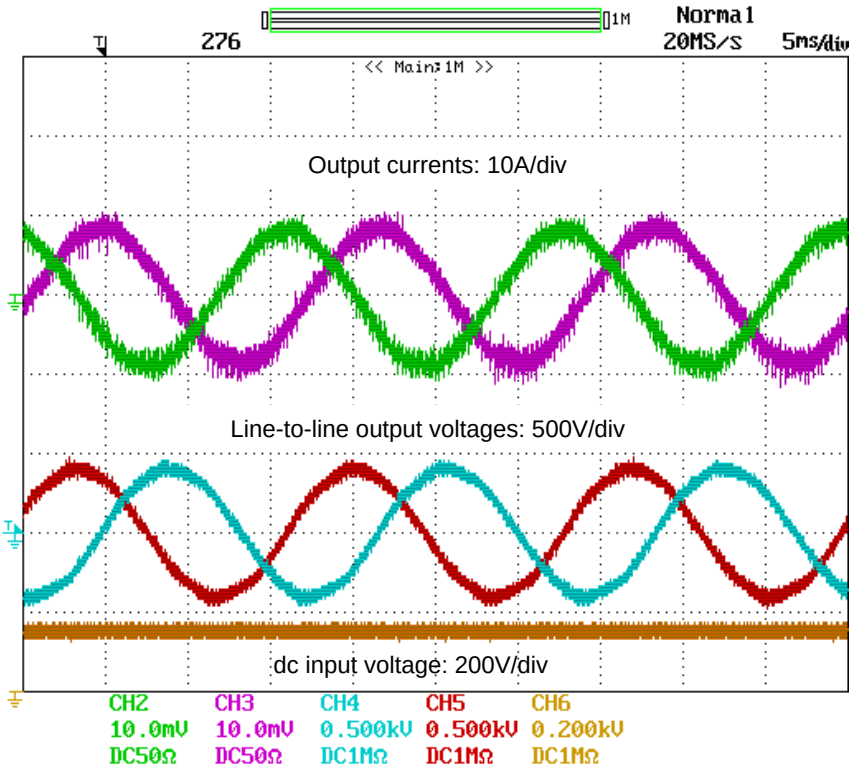

Fig. 8. Waveforms in boost mode at a voltage ratio of 2.67.

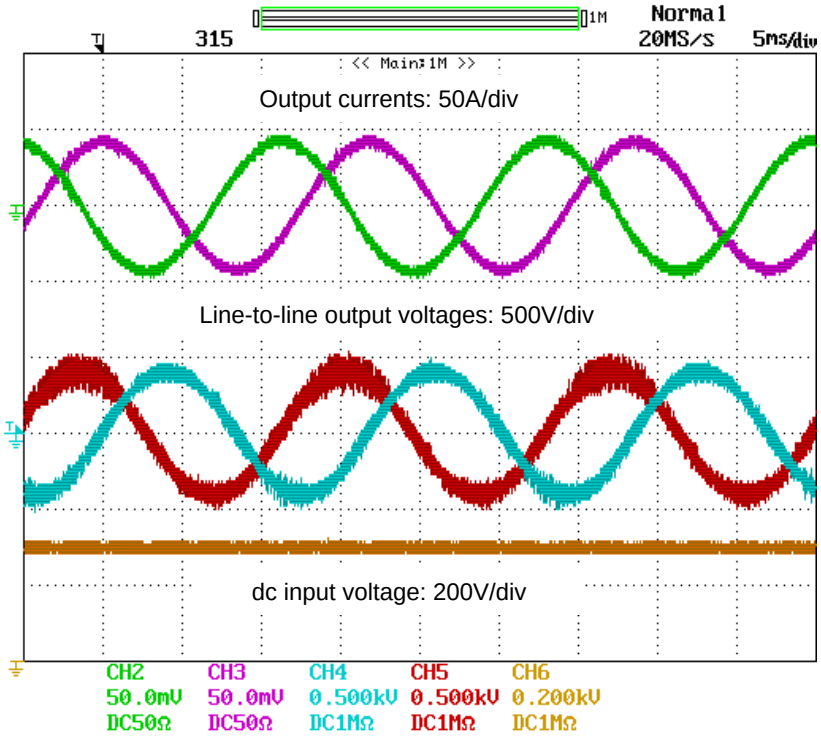

Fig. 9. Waveforms in boost mode at a voltage ratio of 1.35.

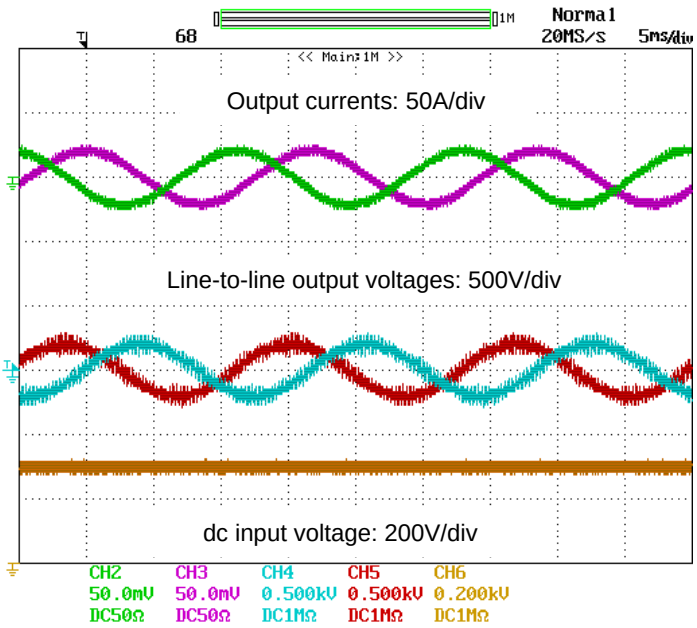

Fig. 10. Waveforms in buck mode at a voltage ratio of 0.67.

Table 5. Measured output voltage distortion factor

Load Power [kW]	Voltage THD [%]
11.31	12.20%
14.78	10.80%
20.24	11.55%

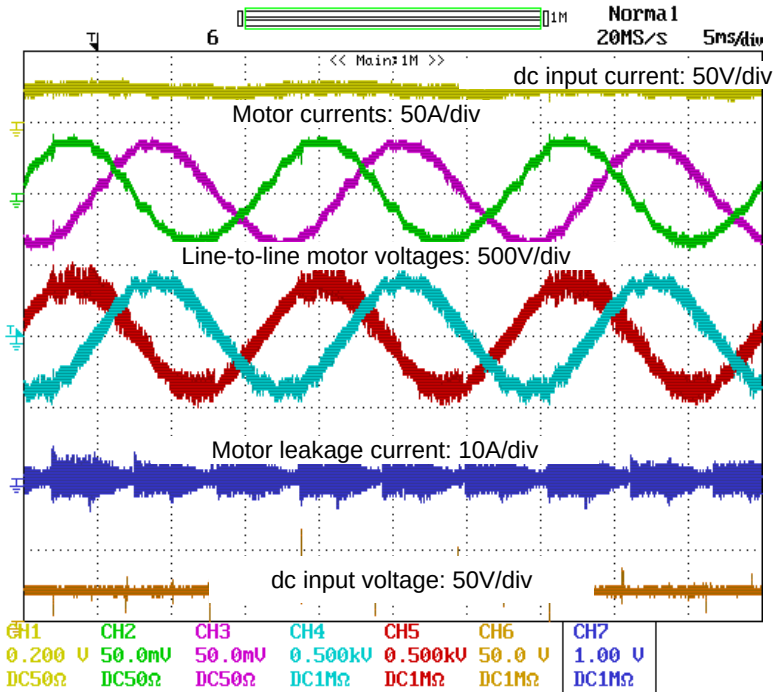

Fig. 11. Test waveforms for measuring motor bearing leakage current, 0.319A.

Conclusion

A high-performance motor drive using a current-source–based inverter has been proposed for HEV applications. The CSI offers many advantages, including (1) high reliability as a result of eliminating dc bus capacitors and the ability to endure phase-leg shoot-through, (2) improved motor efficiency and lifetime as a result of sinusoid-shaped voltage and current to the motor, (3) an increased constant-power speed range owing to the voltage boosting capability, and (4) reduced requirements for battery storage capacity in plug-in HEVs.

A 55 kW CSI was designed, fabricated, and tested. Test results confirmed the following:

- Total capacitance can be reduced to 195 μF from 2000 μF in a VSI.
- Voltage boost ratio can be achieved up to 3.47.
- Output voltage total harmonic distortion factor of less than 12.5%.
- Motor leakage current per motor terminal voltage of: 1.146 mA/V.

References

8. B. Wu, G. R. Slemon, and S. B. Dewan, "PWM-CIS induction motor drive with phase angle control," *IEEE Transactions on Industry Applications* **27**(5), 970–976 (September/October 1991).
9. B. Wu, S. B. Dewan, and G. R. Slemon, "PWM-CIS inverter for induction motor drives," *IEEE Transactions on Industry Applications* **28**(1), 64–71 (January/February 1992).
10. G. Joos, G. Moschopoulos, and P. D. Ziogas, "A high performance current source inverter," *IEEE Transactions on Power Electronics* **8**(4), 571–579 (October 1993).
11. M. Takei, Y. Harada, and K. Ueno, "600V-IGBT with reverse blocking capability," pp.413–416 in *Proceedings of IEEE ISPSD'2001*, 2001.
12. E. R. Motto, J. F. Donlon, M. Tabata, H. Takahashi, Y. Yu, and G. Majumdar, "Application characteristics of an experimental RB-IGBT (reverse blocking IGBT) module," pp. 1504–1544 in *Proceedings of IEEE IAS 2004 Annual Meeting*, 2004.

Patents

Gui-Jia Su, "Power Conversion Apparatus and Method," Provisional application LNG 64117.PV.

4.5 Using the Traction Drive Power Electronics System to Provide Plug-in Capability for Hybrid Electric Vehicles (HEVs)

Principal Investigator: Gui-Jia Su
Oak Ridge National Laboratory
National Transportation Research Center
2360 Cherahala Boulevard
Knoxville, TN 37932
Voice: 865-946-1330; Fax: 865-946-1262; E-mail: sugj@ornl.gov

DOE Technology Development Manager: Susan A. Rogers
Voice: 202-586-8997; Fax: 202-586-1600; E-mail: Susan.Rogers@ee.doe.gov

ORNL Program Manager: Mitch Olszewski
Voice: 865-946-1350; Fax: 865-946-1262; E-mail: olszewskim@ornl.gov

---

Objectives

- Overall project objectives
  - Reduce cost and volume by 90% compared with stand-alone battery chargers.
  - Provide rapid charging capability for use at high-power charging stations.
  - Enable plug-in hybrid electric vehicles (PHEVs) as mobile power generators.
  - Investigate hardware and software requirements for implementing smart charging and vehicle-to-grid capabilities.
- Objectives for FY 2008 effort
  - Design, fabricate, and test an HEV power electronics system prototype comprised of a 55 kW motor inverter and a 30 kW generator inverter to evaluate its battery charging capability.
  - Characterize charging performance in terms of efficiency, power factor, and grid current harmonic distortion factor.

Approach

- Finalize the design developed in FY 2007.
- Fabricate a prototype of a 55 kW motor inverter and a 30 kW generator inverter based on the design specifications.
- Develop digital signal processing code to implement the battery charging control algorithms for both slow and rapid charging.
- Test and evaluate the prototype's charging capability and performance.

Major Accomplishments

- Designed, fabricated, and successfully tested an HEV power electronics system prototype consisting of a 55 kW motor inverter and a 30 kW generator inverter for operation as a battery charger.
- Attained a maximum efficiency of >95% with a 120 V input and >98% with a 240 V input.
- Attained a grid current harmonic distortion factor at rated power of <9% at 120 V input and < 7% at 240 V input

Future Direction

- Modify the prototype to implement and demonstrate mobile power generator capability.
- Assess thermal control requirements for mobile generation and rapid charging operations.
- Implement smart charging capabilities.

Technical Discussion

Background

PHEVs are emerging as a pre–fuel cell technology that offers greater potential than hybrid vehicles currently on the market to reduce oil consumption and carbon dioxide emissions. In PHEVs, the energy storage capacity of the battery needs to be increased significantly to enable a driving distance of at least 40 miles in an all-electric mode, the distance needed to substantially reduce oil consumption for daily commuting. A charger is also required to replenish the battery after it is depleted, typically done overnight to leverage energy costs by taking advantage of off-peak electricity rates.

Stand-alone battery chargers, however, impose an extra cost on already expensive HEVs and have other limitations. A typical stand-alone battery charger for PHEVs consists of a diode rectifier and a unidirectional dc-dc converter (i.e., it can only charge the battery) that uses power semiconductor switches, diodes, inductors, and capacitors, as shown in Fig. 1. A charger with a low charging capability of 1~3 kW can cost almost 30% as much as the electric traction system for a mid-size PHEV-20 car ($690) [1]. The limited charging capability results in a long charging time (6~8 hours), which could negatively impact the acceptance of PHEVs.

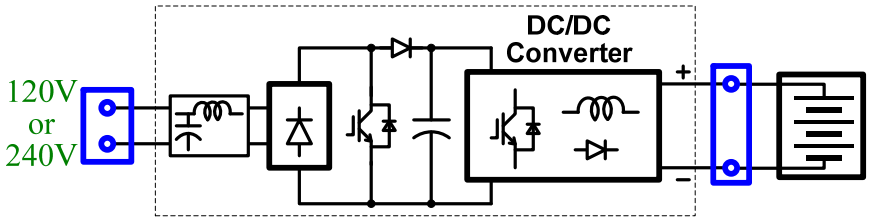

Fig. 1. A schematic showing major components in a stand-alone battery charger.

To minimize the cost of the charger, this project is investigating the use of the power electronics and motors already aboard the vehicle to fulfill the charging requirements. It is expected that, compared with a stand-alone battery charger, the proposed approach will impose virtually no additional cost or will significantly reduce the cost, depending on the configuration of the onboard traction drive system. The proposed approach is to integrate the battery charging function into the traction drive system and eliminate or minimize the number of additional components. Because traction power inverters have a greater current-carrying capability, the integrated charger can reduce the charging time significantly. Another benefit of this approach is that it enables PHEVs to function as mobile generators at little or no additional cost. Another objective is to investigate hardware and software requirements for implementing smart charging and vehicle-to-grid capabilities.

Description of the reduced-part dc-dc converter

Figure 2 shows topologies for using the onboard electrical drive system to provide plug-in charging and mobile generation capabilities for HEVs. The onboard electrical drive system may consist of one or more electrical motor drive units, all connected to a common dc bus. Each motor drive unit typically employs a three-phase inverter/converter (INV/CONV) and a three-phase motor/generator (MG) with a Y-connection with a neutral point (N_{MG}). At least one drive unit is coupled to the engine shaft through a mechanical transmission device. The basic idea is to use the MGs as inductors by connecting their neutral points to an external charging source to charge the battery, or to external loads to supply power to them. The external charging source can be a dc or single-phase or multiphase ac power supply, depending on the number of onboard drive units. Figure 2a illustrates an arrangement for a series HEV in which two

INV/CONVs and two MGs are employed. For such vehicles, virtually no additional components except some wiring and connectors are required. An ac filter capacitor may also be needed to meet grid interface

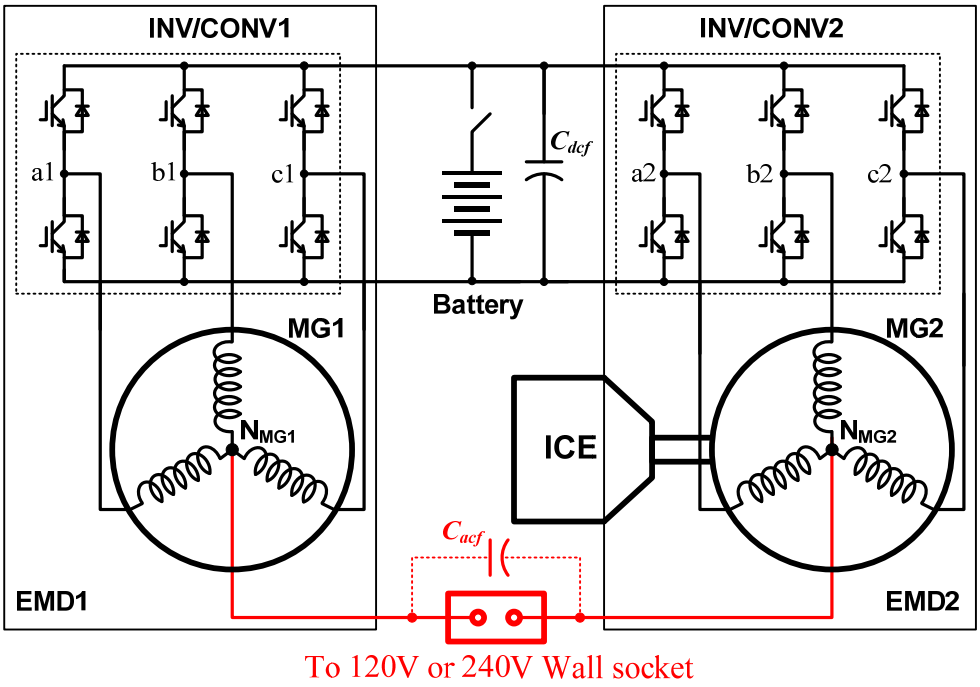

(a) For HEVs using two inverters and motors

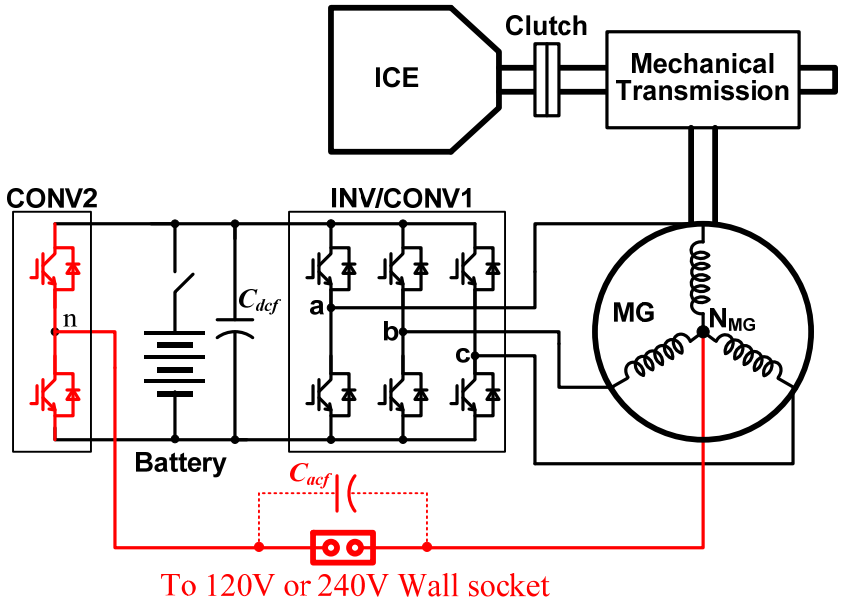

(b) For HEVs using a single inverter and motor

Fig. 2. Topologies for using the onboard electrical drive system to provide plug-in charging and mobile generation capabilities for HEVs. (Red denotes added components).

power quality requirements. For parallel HEVs, in which only one INV/CONV and MG are used, two switches must be added, as shown in Fig. 2b.

All the switch legs in each INV/CONV collectively function as a single switch leg and the MG as an inductor. Together, the drive units form a single-phase or multiphase converter, operating in the charging mode, to regulate the dc bus voltage. In the generation mode, the drive units form a single-phase or multiphase inverter to supply external loads. In this mode, the MG of the drive unit coupled to the engine shaft is driven by an engine to generate power to supply the dc bus and ultimately the external loads. Or power can be drawn from the battery for short operating intervals.

Figure 3 shows an equivalent circuit of Fig. 2a during operation in charging mode. All three switch legs (a1, b1, c1 and a2, b2, c2) in INV/CONV1 and INV/CONV2 collectively function as a single switch leg and the MGs function as two impedance networks—their stator zero sequence impedance networks (ZSIN1 and ZSIN2). Each ZSIN consists of three branches and each branch comprises the stator winding phase resistance (R_{ms1} or R_{ms2}) and the stator phase leakage inductance (l_{m0s1} or l_{m0s2}). Together, the two drive units form a single-phase converter to regulate the battery voltage, V_{bat}, or the charging current, I_{bat}. Normally, the single-phase converter is controlled so as to maintain a unity power factor by keeping the source current, i_s, in phase with the source voltage, v_s. An additional benefit of operating the three-phase converters as single leg converters is the reduction in harmonic current components resulting from interleaving the gating signals of the three legs.

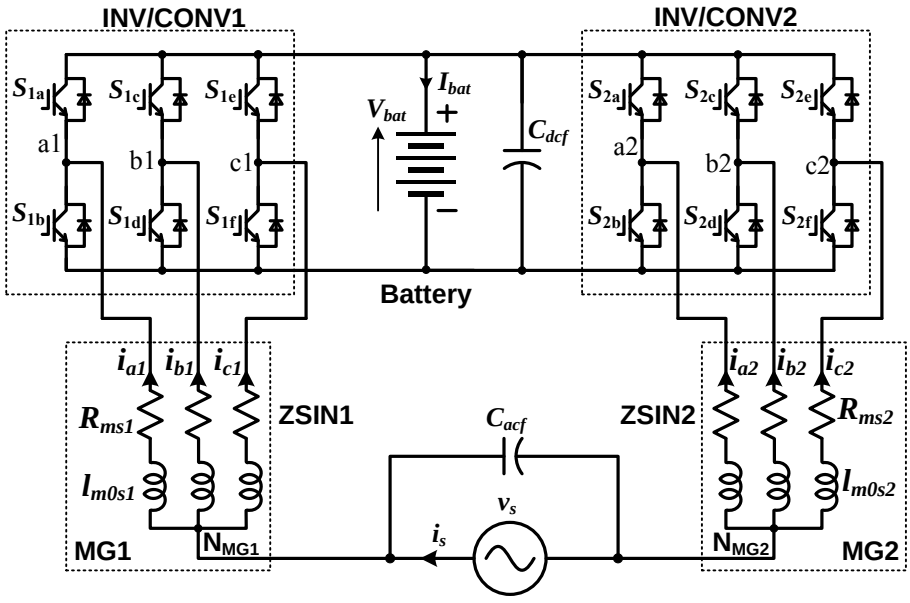

Fig. 3. An equivalent circuit for battery charging mode.

Figure 4 shows equivalent circuits of Fig. 2a during operation in mobile generation mode. There are two available power sources, the battery and the engine. Figure 4a illustrates the case in which the battery is the source. In this case, all three switch legs in each of the two INV/CONVs collectively function as a single switch leg and the MGs as two impedance networks. Together the two drive units form a single-phase inverter to regulate the load voltage, v_{Load}.

Figure 4(b) illustrates the case in which power is generated by the MG2 driven by the engine. In this case, the three switch legs in INV/CONV1 collectively function as the first single switch leg of a single-phase

inverter and the MG1 functions as an impedance network. INV/CONV2 has dual functions. It first operates as a three-phase converter to regulate the dc bus voltage, V_{dc}, by drawing power from the generator; at the same time, its three phase legs collectively form the second switch leg of the single-phase inverter to regulate the load voltage, v_{Load}.

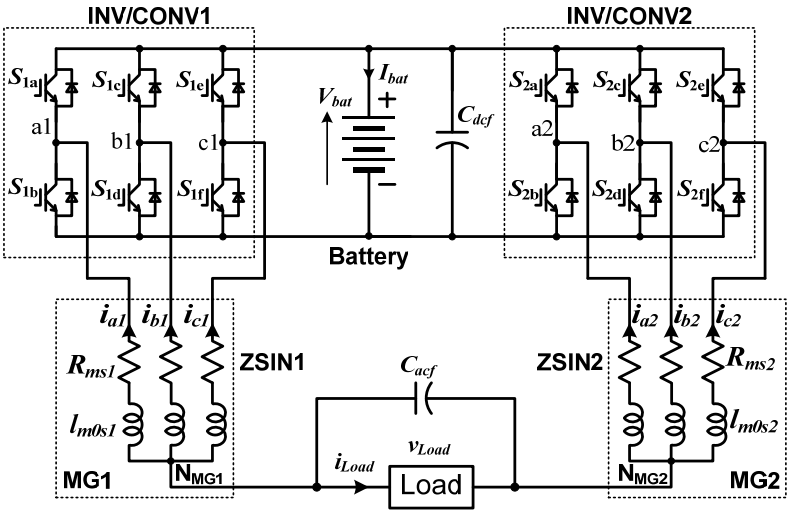

(a) Using the battery as the power source

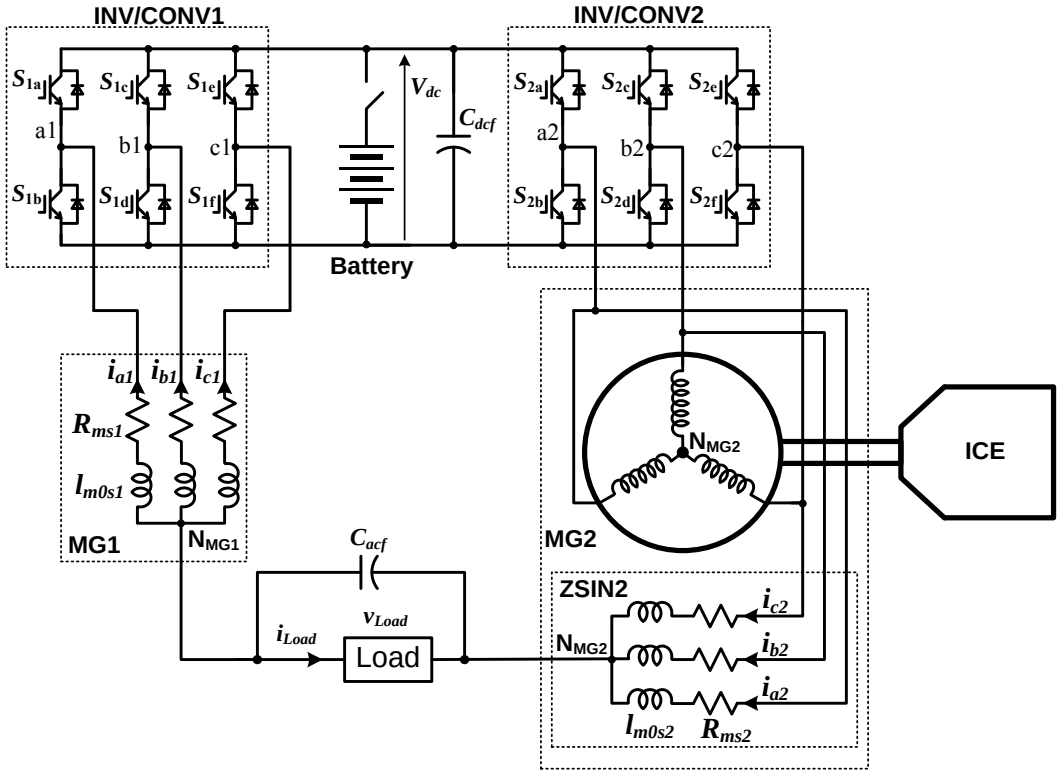

(b) Using the motor MG2 driven by the engine as the power source

Fig. 4. Equivalent circuits for mobile generator mode.

Prototype fabrication and testing

Based on the simulation results, a conceptual design of a drive inverter system consisting of a 55 kW and a 30 kW inverter with plug-in charging and mobile generation capabilities was completed in FY 2007. The design was finalized and a prototype was fabricated. Figure 5 is a photo of the prototype. The 55 kW inverter was implemented with a six-pack insulated gate bipolar transistor (IGBT) module rated at 600 V and 600 A, part number PM600CLA060 from Powerex; and the 30 kW inverter was implemented with a six-pack IGBT module rated at 600 V and 300 A, part number PM300CLA060 from the same vendor. The bus capacitor bank is constructed using four film capacitors, part numbers UP33BC0375, rated at 600 Vdc and 375 μF. These components are mounted on a 12 × 7 in. cold plate.

A 10.9 kW induction motor and a permanent magnet motor rated at 8.2 kW were used in the testing. Table 1 gives their zero sequence resistances. The resistance values of Toyota Camry motors are also given for comparison. Notice the combined resistance of the two test motors is more than 5 times larger than that of the Camry motor owing to the large resistance of the induction motor. This had a significant impact on efficiency.

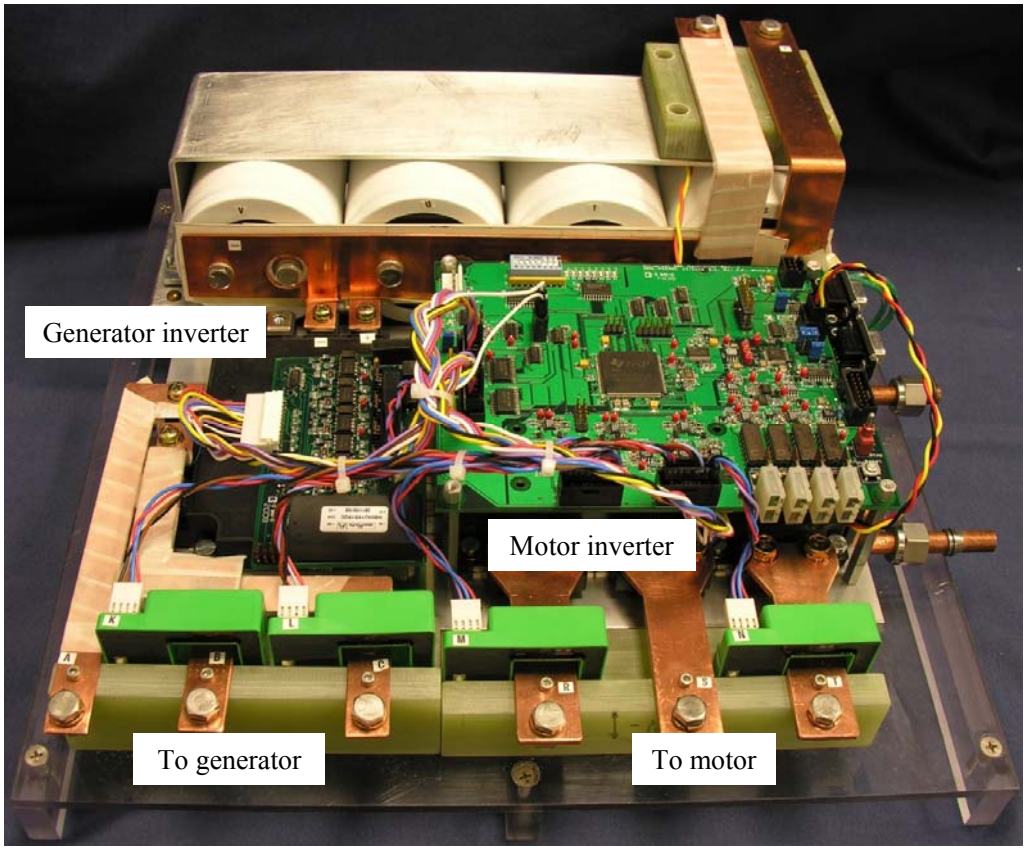

Fig. 5. A photo of a prototype consisting of a 55 kW motor inverter and a 30 kW generator inverter with plug-in charging capability. The heat sink footprint is 12 in. width by 7 in. depth.

Table 1. Motor zero sequence resistance

Test motor 1	165.74 mΩ	Camry generator	21.58 mΩ
Test motor 2	23.8 mΩ	Camry motor	10.75 mΩ
Combined	189.54 mΩ	Combined	32.32 mΩ

The prototype was tested with 120 V and 240 V input sources for varying dc charging power. Figure 6 illustrates test results showing operating waveforms in the charging mode at 12.4 kW from a 240 V source. Figure 7 shows waveforms operating at 2.13 kW from a 120 V source. In both cases, the charger was operating at a near-unity power factor, as indicated by the fact that the source currents were in phase with the source voltages.

Figure 8 plots measured efficiency against dc charging power. The maximum efficiency was 92.6% with a 120 V input and 97.0% with a 240 V input. The large resistance of the test motors significantly lowered the efficiency numbers as the output power increased. For comparison purposes estimated charging efficiencies for the Toyota Camry motor are also shown. The Camry estimations are 95.3% with a 120V input and 98.2% with a 240 V input. Although the prototype was designed to provide a maximum charging power of greater than 20 kW, the tests were limited to 14.5 kW by the 240 V source capability.

Figure 9 plots measured power factor and Fig. 10 plots measured total harmonic distortion (THD) of the grid current against dc charging power. The power factor is over 99% over a wide range of dc charging power. Grid current THD at rated power is less than 9% with a 120 V input and less than 7% with a 240 V input.

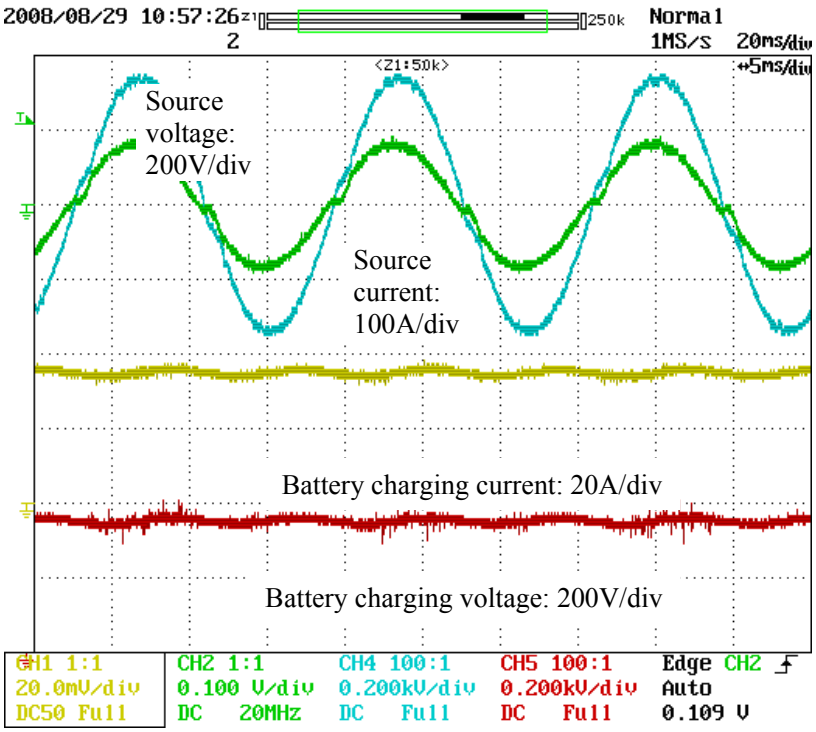

Fig. 6. Test results showing operation in charging mode at 12.4 kW from a 240 V source.

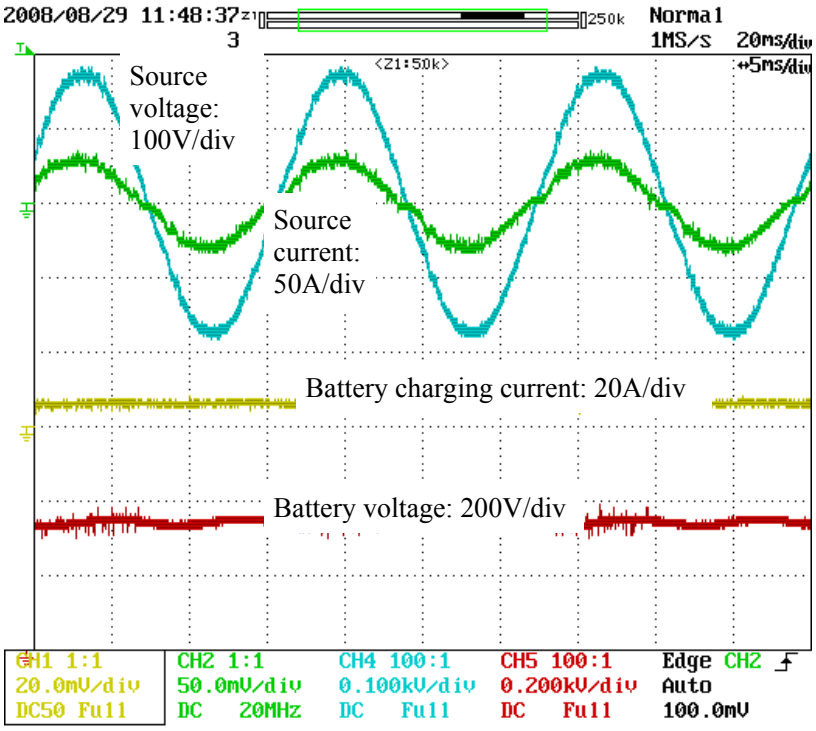

Fig. 7. Test results showing operation in charging mode at 2.13 kW from a 120 V source.

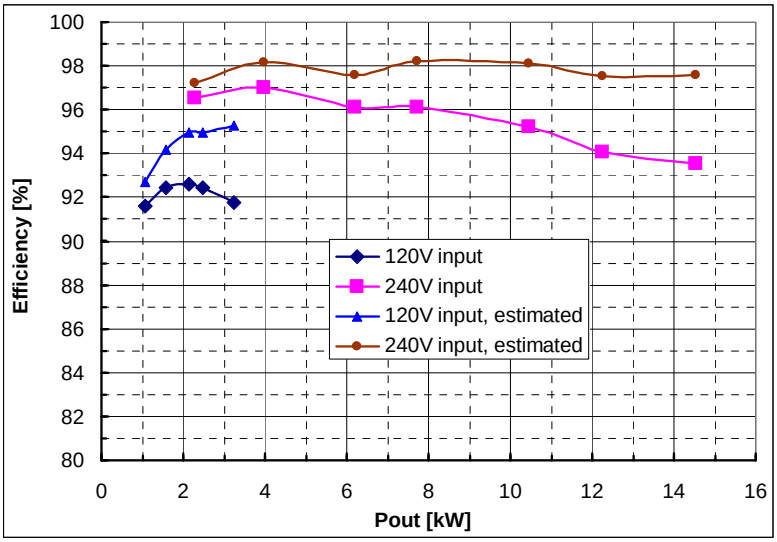

Fig. 8. Measured and estimated efficiency.

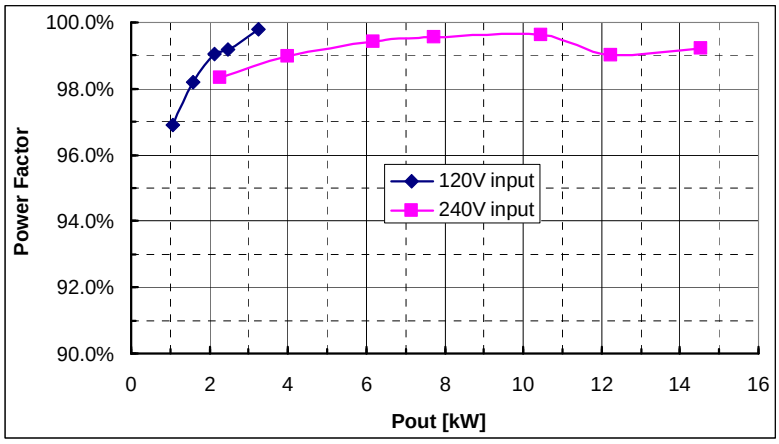

Fig. 9. Measured power factor.

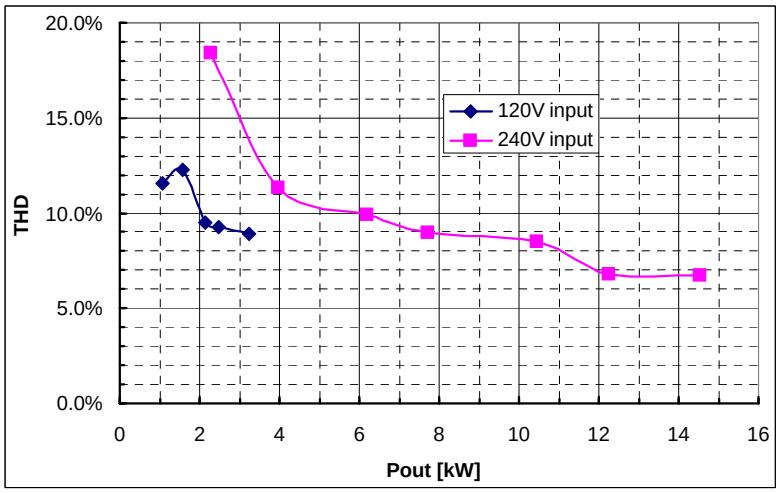

Fig. 10. Measured total harmonic distortion (THD) of the grid current.

Conclusion

This project explored ways of using the onboard electrical drive system in different HEV configurations to provide plug-in charging capability. The proposed charging schemes offers many benefits, including (1) significantly reducing the cost and volume of battery chargers in PHEVs, (2) providing rapid charging capability, and (3) enabling the use of PHEVs as mobile generators. Detailed circuit simulations were carried out, and the simulation results proved the concepts and validated the rapid charging capability.

An HEV power electronics system prototype made up of a 55 kW motor inverter and a 30 kW generator inverter was designed, fabricated, and successfully tested for operation as a battery charger. Test results confirmed high efficiency, high power factor, and low harmonic distortion:

- Maximum efficiency: >95% with a 120 V input and >98% with a 240 V input
- Grid current harmonic distortion factor at rated power: < 9% with a 120 V input and < 7% with a 240 V input

References

1. *Advanced Batteries for Electric-Drive Vehicles*, Report 1009299, Electric Power Research Institute, May 2004.

Patents

Gui-Jia Su, "Electric Vehicle System for Charging and Supplying Electrical Power," Patent No. US2008/0094013A1, pending.

5. Systems Research and Technology Development

5.1 Benchmarking of Competitive Technologies

Principal Investigator: Tim Burress
Oak Ridge National Laboratory
National Transportation Research Center
2360 Cherahala Boulevard
Knoxville, TN 37932
Voice: 865-946-1216; Fax: 865-946-1262; E-mail: burressta@ornl.gov

DOE Technology Development Manager: Susan A. Rogers
Voice: 202-586-8997; Fax: 202-586-1600; E-mail: Susan.Rogers@ee.doe.gov

ORNL Program Manager: Mitch Olszewski
Voice: 865-946-1350; Fax: 865-946-1262; E-mail: olszewskim@ornl.gov

---

Objectives

- Determine the status of nondomestic hybrid electric vehicle (HEV) technologies through assessment of design, packaging, fabrication, and performance during comprehensive evaluations
  - — Compare results with those from other HEV technologies
  - — Distribute findings in the open literature
- Support FreedomCAR program planning and assist in guiding research efforts
  - — Confirm the validity of the program technology targets
  - — Provide insight for program direction
- Produce a technical basis that aids in modeling/designing
- Foster collaborations with the Electrical and Electronics Technical Team (EETT) and Vehicle Systems Analysis Technical Team (VSATT)
  - — Identify unique motor/inverter/converter/drive-train technologies
  - — Ascertain what additional testing is needed to support research and development

Approach

- Choose a vehicle subsystem
  - — Evaluate the potential benchmarking value of various HEVs
  - — Consult with original equipment manufacturers as to which system is most beneficial
- Tear down a power converter unit (PCU) and an electronically-controlled continuously variable transmission (ECVT)
  - — Determine volume, weight, specific power, and power density
  - — Assess design and packaging improvements
  - — Test magnets and capacitors
- Prepare components for experimental evaluation
  - — Develop interface and control algorithm
  - — Design and fabricate hardware necessary to conduct tests
  - — Instrument subsystems with measurement devices
- Evaluate hybrid subsystems
  - — Determine peak and continuous operation capabilities
  - — Evaluate efficiencies of subsystems
  - — Analyze thermal data to determine assorted characteristics

Major Accomplishments

- Selected the 2008 Lexus LS600h system to benchmark based on anticipated automotive manufacturer interest due to the novel double-sided cooling technique that accompanies the most powerful HEV drivetrain currently on the market.
- Conducted design/packaging studies of the LS600h PCU and ECVT, revealing significant improvements over Toyota Prius and Camry designs.
- Bypassed the LS600h PCU motor inverter controls to allow full control over testing conditions.
- Disassembled and evaluated key components within the PCU/ECVT.
- Assessed mass, volume, power density, and specific power of various PCU/ECVT components.
- Evaluated efficiency, performance, and continuous operational capabilities of the LS600h subsystems.
- Communicated effectively with EETT and VSATT to aid in discerning project direction, test plan, and test results.

Future Direction

- Discussions will be conducted with EETT and VSATT to determine the appropriate system to study in FY 2009.
- Approaches similar to those of previous benchmarking studies will be taken while working to meet the universal need for standardized testing conditions.

Technical Discussion

The subsystems of the 2008 Lexus LS600h Synergy Drive were obtained in order to conduct thorough studies of design, packaging, efficiency, performance, and operational characteristics. The LS600h hybrid drive system is similar to those of the Toyota Prius and hybrid Camry in terms of overall function. However, there are significant differences between the designs in both the PCU and ECVT subsystems. The primary discrepancy between the LS600h PCU and previous PCU designs is the introduction of a double-sided cooling technique that incorporates a power electronics module with cooling plates for both the collector and emitter sides of the insulated gate bipolar transistor (IGBT), as opposed to a cooling plate for only the collector side of the IGBT. The double-sided cooling method greatly increases the capability to remove heat from the IGBTs and diodes and thereby reduces the constraints placed upon these high-power semiconductors.

The LS600h ECVT has an elongated transmission housing to supplement all-wheel drive capability in contrast to the front-wheel-drive transaxle configurations previously benchmarked. Consequently, the primary interior permanent magnet motor of the LS600h has a smaller diameter but is more elongated than its front-wheel-drive counterparts. This geometrical reformation is suited to the constraints associated with the undercarriage location of the ECVT. Published specifications indicate that the primary drive motor is rated at 165 kW, can produce 300 Nm up to 5,250 rpm, and has a maximum motor speed of 10,230 rpm. The motor is connected to the primary drive shaft through a gear ratio much like that of the Camry; however, the gear ratio of the Lexus can be selected to be high or low by means of a Ravigneaux gear system with a clutch and brake system.

An important product of the benchmarking efforts is not only validation of specifications published by the manufacturer, but also a detailed understanding of requirements and characteristics corresponding with operation points throughout the entire operation range, including peak regions. For example, the LS600h motor can produce 300Nm only for very short periods of time, and the extent of the time varies with parameters such as speed and ambient temperature. These requirements and characteristics are essential in making comparisons with other drive system designs and are particularly useful for comparisons of motor/power converter design, motor modeling, and thermal modeling. The results from these efforts are detailed in [1].

Teardown—power converter unit

The PCU shown in Fig. 1 includes a cooling infrastructure for the double-sided power modules, boost converter, motor inverter, generator inverter, and their associated components such as capacitors, drivers, and controllers. Although the overall function and appearance of the LS600h PCU is similar to that of the Camry PCU, there is a significant difference between the two in terms of architecture. As shown in Ref [1], the Camry PCU has a separate compartment for the boost converter. To accommodate the move to the double-sided cooling technique, all power electronics are located adjacent to one another in the LS600h PCU. Additionally, the control and driver electronics for the boost converter and inverters are grouped together on the same boards, as opposed to the Camry design. The bus architecture and cooling infrastructure have also been significantly redesigned. There are many subtle differences between the Camry and Lexus PCU, such as a larger dc link capacitor, and boost converter inductor, and the side housing for motor and generator connectivity.

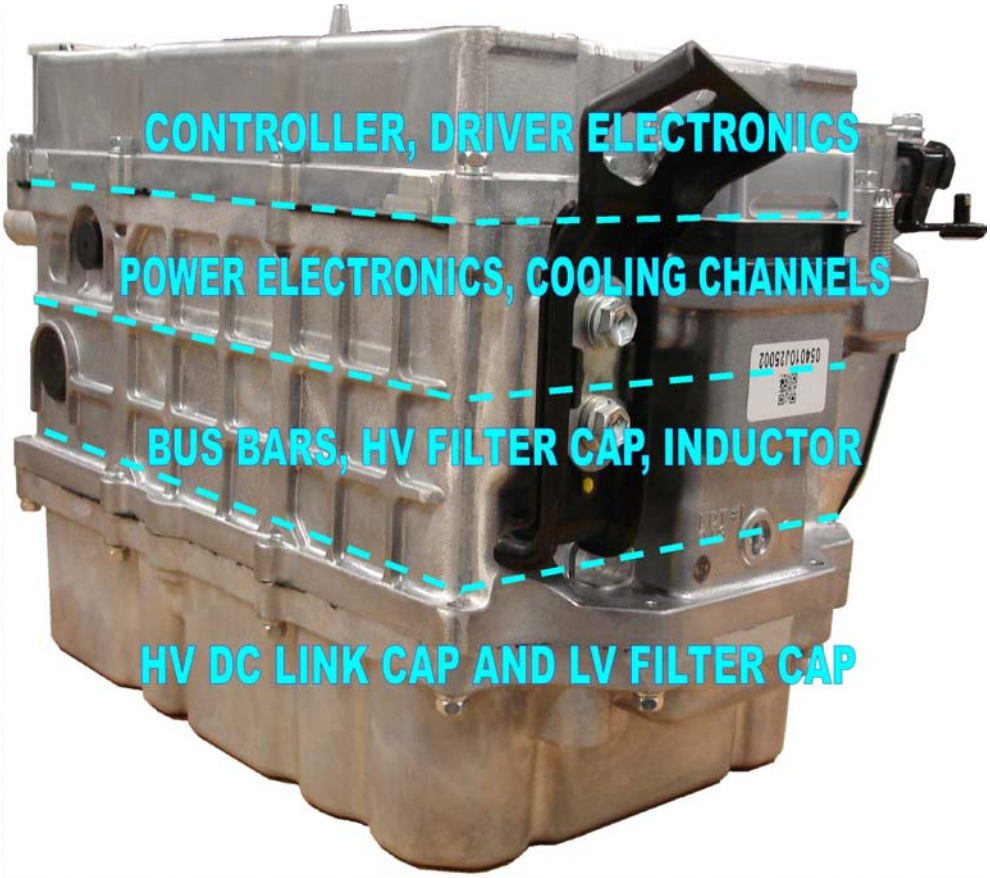

Fig. 1. The LS600h power converter unit.

The PCU was completely disassembled; its primary components are indicated in Fig. 2. Shown in the upper portion of Fig. 2 is the entire PCU with two ~288 V connectors as well as the control and driver boards. A battery voltage of ~288 V is applied to the boost converter input and is also fed to the secondary ~288 V connector through a fusible link in order to supply energy to the air-conditioning compressor inverter. Under the lid covering the driver and controller circuits, the topologies appear to be generally similar to that of the Camry, yet further analysis reveals several design changes.

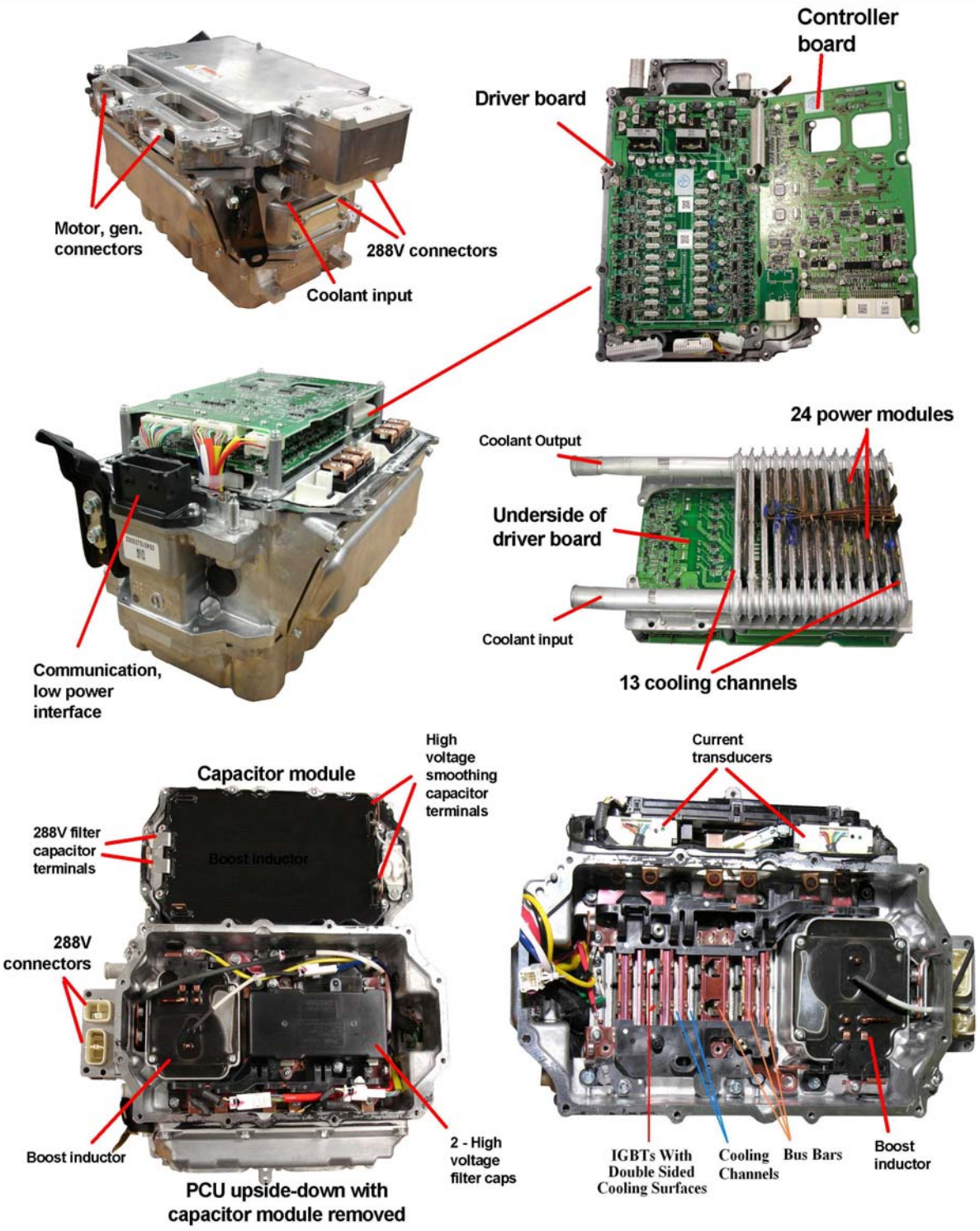

Fig. 2. LS600h PCU teardown.

In the lower-left portion of Fig. 2, the PCU sits upside-down with the capacitor module removed and placed adjacent to the PCU. The size of the capacitor module has increased significantly compared with the Camry, as it now houses both the low-voltage filter capacitor and the high-voltage smoothing capacitor. Capacitance values increased for the high-voltage capacitor from 2.098 to 2.61 mF and

decreased for the low-voltage capacitor from 378 to 365 μF in moving to the Lexus design. Terminals of the low-voltage capacitor section of the module connect to terminals at the boost converter input, which is supplied directly from the 288 V battery. The high-voltage capacitor terminals connect directly to the dc link, which reaches up to 650 V and is shared by the motor and generator inverters. A bus bar inside the capacitor module serves as the common to the low and high sides of the boost converter. Just as in the in the Camry PCU, a 54 kΩ resistor is used and is located next to and attaches directly to the high-voltage terminals, thereby bleeding off the dc-link during inactivity. Located in the middle compartment next to the boost converter inductor are two additional high-voltage filter capacitors, which are combined into a small capacitor module. After the small capacitor module is removed, the bus bars, power modules, and cooling channels are visible, as shown in the lower-right hand corner of Fig. 2.

Shown in the middle portion of Fig. 2 is the entire PCU cooling infrastructure for the 24 double-sided power electronics modules. Just as in previous designs, an ethylene glycol and water mixture is circulated through the PCU and ECVT to a radiator that is on a separate loop from the internal combustion engine. However, the LS600h cooling system does not incorporate a conventional heat sink but instead uses 13 cooling channels to straddle the 12 sets of upper and lower power electronics modules. With a total of 24 modules, 12 are used in the motor inverter, 6 in the generator inverter, and 6 in the boost converter. Each module contains a diode and an IGBT with five drive/sensing pins as well as collector and emitter bus bars protruding from the module, as indicated in the upper-left segment of Fig. 3.

The LS600h power module detailed in Fig. 3 incorporates a collector plate/bus and an emitter plate/bus, both of which transfer heat to the nearest cooling channel through thermal grease, and an insulator. A black high-density, high-temperature plastic retains and supports all components of the power module. The IGBT collector and diode cathode are soldered directly to the collector plate, and the IGBT emitter and diode anode are soldered to spacers, which are soldered to the emitter plate. With the PCU sitting upright, collector and emitter bus bars extend downward to the converter/inverter bus bars, while the drive/sense pins extend upward to the driver board. A large metal strip applies pressure to the entire stack of modules and cooling channels to ensure mating surfaces are complementary to heat transfer. Although the output power rating of the motor inverter is increased considerably from that of the Camry, the number of IGBTs and diodes used for the motor inverter decreased from 18 to 12, as the semiconductor ratings are greatly affected by the capabilities of the thermal management system.

Teardown—ECVT

The overall functionality of the 2008 LS600h ECVT, shown in Fig. 4, is similar to that of the Camry and Prius, yet there are significant differences between the subsystem designs. All systems use the sun gear of a planetary gear set to receive input from the generator with a hollow rotor shaft, through which a shaft connected to the internal combustion engine passes and connects to the planetary carrier. The ring of the planetary gear is connected directly to the motor output in the Prius and to the motor through a high-speed reduction gear in the Camry. The Prius and Camry planetary rings drive the differential output through a series of drive gears. Similar to the Camry design, the LS600h ring gear connects to the motor output through a gear system. However, the LS600h uses a Ravigneaux gear configuration to facilitate a high and low gear selection through a clutch, brake, and pressure plate mechanism similar to what is found in many conventional automatic transmissions. A Ravigneaux gear system consists of two planetary gear sets, and its operation can be manipulated depending on which clutch set has pressure applied to it, thereby locking the ring of the corresponding planetary gear set to the chassis. A long shaft passes through the center of the drive motor rotor and connects the power split planetary ring to the output of the Ravigneux gear system, and the two are unified into one spline. This spline mates with the input of the transfer case, which also uses a small planetary gear to distribute power to the front and rear wheels appropriately.

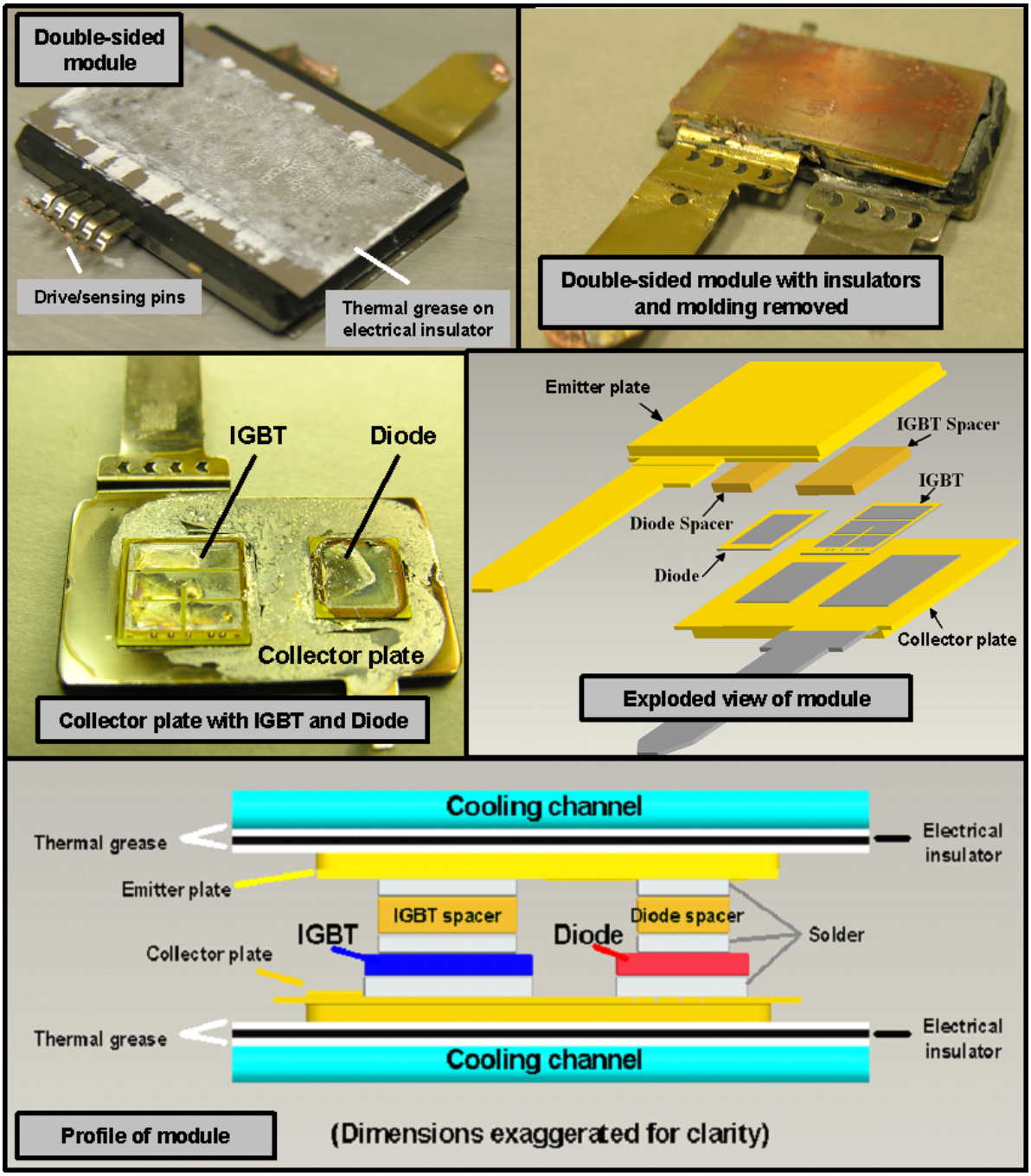

Fig. 3. LS600h power module with double-sided cooling.

One of the most noticeable features of the electric machines in Fig. 4 is the elongated shape of the motor rotor. Figure 5 provides details of the LS600h motor design, as well as a comparison of the motor stator laminations of the LS600h and 2007 Camry. Table 1 lists various LS600h and Camry motor parameters. The outer diameters of the LS600h motor and Camry motor stator laminations are 7.88 and 10.395 in., respectively. Stator lamination stack lengths for the LS600h and Camry motor are 5.33 and 2.4 in., respectively. Although the lamination outer diameter of the LS600h is only 76% that of the Camry, the lamination stack is more than twice the length. The entire stator mass is relatively the same, but the LS600h rotor is about 6.5 lbs heavier than the Camry rotor.

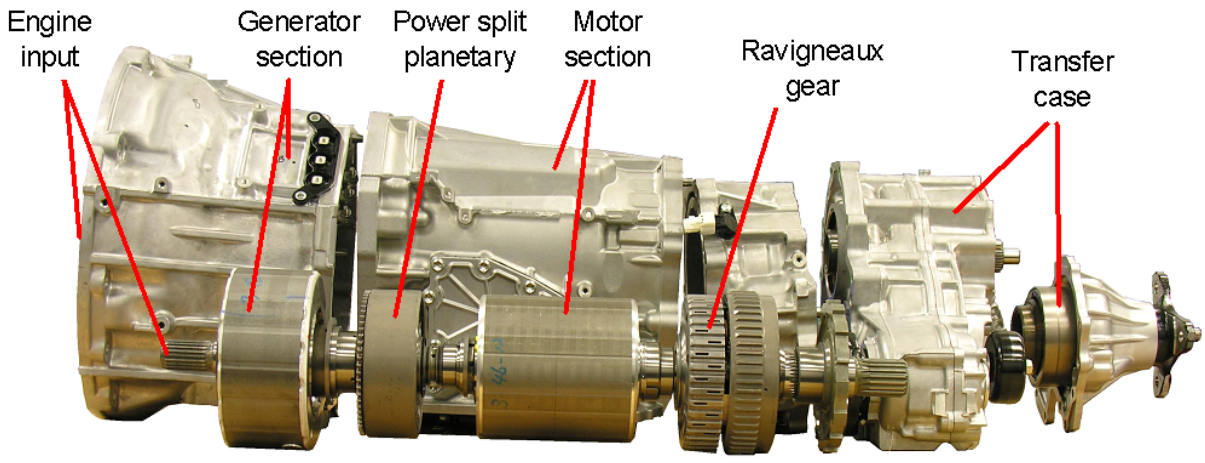

Fig. 4. Various sections of 2008 Lexus LS600h ECVT.

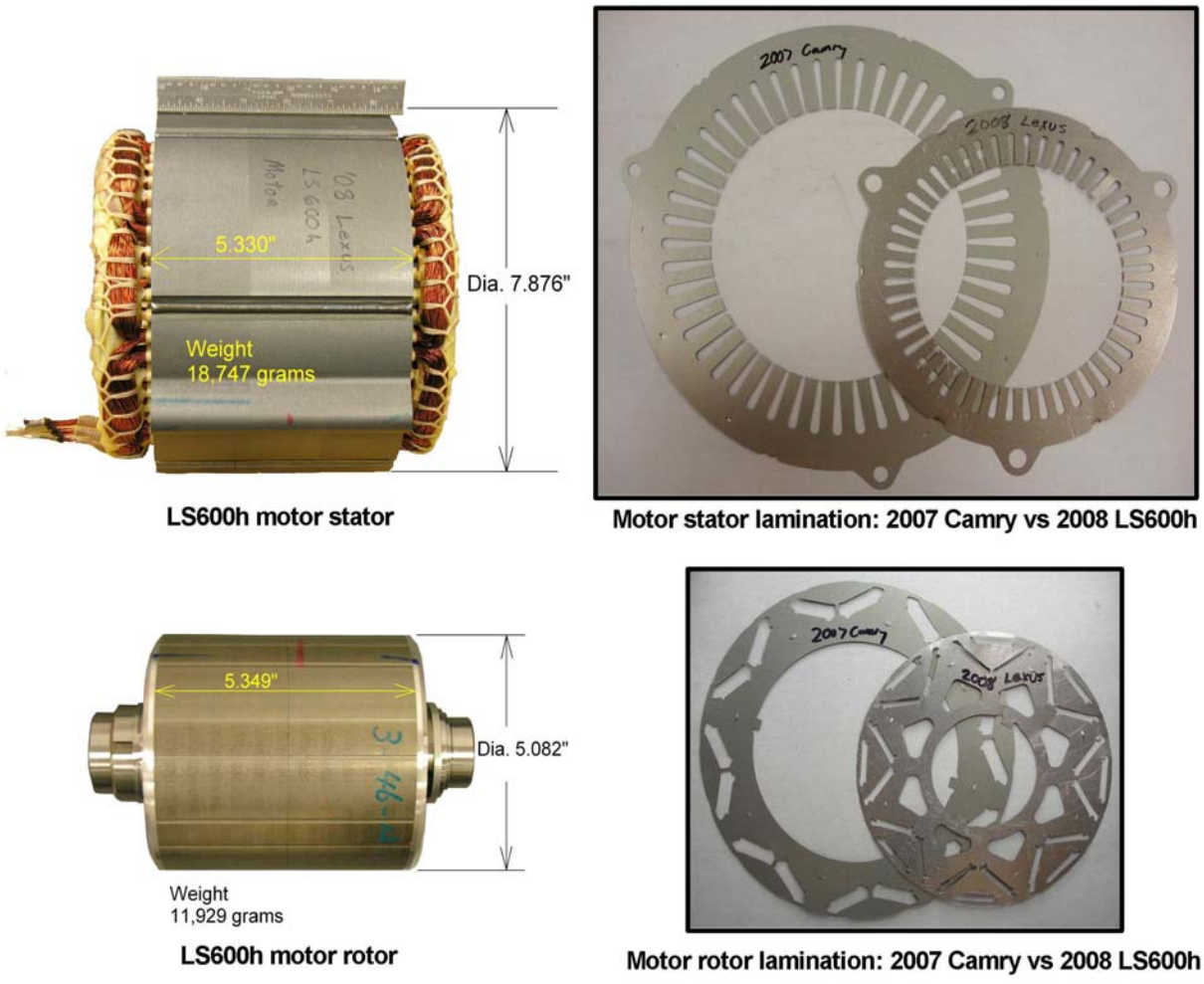

Fig. 5. LS600h vs Camry: motor stator (upper) and motor rotor (lower).

Table 1. Comparison of 2008 LS600h and 2007 Camry motor parameters

	LS600h	Camry
Motor stator outer diameter	7.88 in.	10.395 in.
Motor stator stack length	5.33 in.	2.4 in.
Motor stator mass	41.3 lb	39.7 kg
Motor rotor mass	26.2 lb	19.8 lb
Magnet mass	2.97 lb	2.05 lb
Copper mass	7.92 lb	12.5 lb
Peak air-gap flux measurement	8.53 kG	8.2 kG

A closer look at the LS600h and Camry rotor laminations in Fig. 5 reveals that the LS600h magnet slots are much thinner, and there is also an additional slot. Beginning with the 2004 Prius, all Toyota permanent magnet motors have had the "inverted V" magnet orientation. Although the additional magnet in the LS600h adds to the peak magnet strength, as verified in air-gap flux measurements, the location of the magnet effectively hinders the reluctance torque component. The length of each magnet was increased from 2.387 to 2.62 in. and the thickness reduced from 0.26 to 0.12 in. Two sets of these magnets are installed into the LS600h rotor, giving a total of 48 magnets. Overall, the magnet mass increased from ~2 to ~3 lb. It is possible that the low maximum-speed rating of 10,230 rpm is due to the mechanical stresses associated with the retention of the additional extra magnet. It is not set as deeply into the lamination as the "inverted V" magnets. Although the elongated design has a higher magnet mass, the amount of copper used in the stator was reduced from 12.5 to 7.92 lb, even though the peak power capability was increased considerably. Although the motor underwent significant design changes, the LS600h generator stator laminations have the same outer diameter and inner diameter as the stator laminations of the Camry motor and generator.

Table 2 provides a comparison of the specific power and power density of three HEV systems, the Prius, Camry, and LS600h. The results indicate that the peak power density and peak specific power of the inverter improved by ~50% from the Camry to the LS600h. Note that peak power capabilities were used in these calculations, and the use of continuous ratings may yield closer results for the motor assessments. However, it is difficult to generalize continuous power ratings as they are based upon a variety of conditions, such as coolant temperature, stator temperature limit, and motor speed. Nonetheless, the double-sided cooling technique has an apparent advantage over previous designs.

Table 2. Comparison of specific power and power densities for various HEV components

Component and parameter	Lexus (110 kW)	Camry (70 kW)	Prius (50 kW)
Motor			
Peak power density, kW/L	6.6	5.9	3.3
Peak specific power, kW/kg	2.5	1.7	1.11
Inverter (excluding generator inverter and buck/boost converter)			
Peak power density, kW/L	17.1	11.7	5.7
Peak specific power, kW/kg	14.8	9.3	5.7

Experimental evaluation

Various evaluations were conducted of the PCU and ECVT to determine operational characteristics such as efficiency, continuous capability, and performance. Initial tests include measurement of back-emf (electromotive force) voltage, no-load losses, and locked rotor torque. These tests provide parameters and characteristics of the motor that are useful for approximating its capabilities. Secondary evaluations include efficiency, performance, and continuous analyses of the subsystems. Before any tests could be conducted, the ECVT was modified to provide access to the motor shaft. The only shafts externally accessible are the engine input and Ravigneaux gear output shafts. Although the Ravigneaux gear is indirectly connected to the motor, power measurements through these gears would not be accurate enough to make precise motor efficiency calculations. A shaft was designed and fabricated in order to provide external access to the motor rotor. The fabricated shaft was fed directly to a speed and torque transducer. The other side of the torque transducer was coupled to a speed reduction gear box. The gear box is capable of handling speeds of up to 18,000 rpm, and the dynamometer can operate at power levels of up to 400 hp. All hardware on the high-speed portion of the shaft was designed to have face-mount couplings, which provide extra safety since the shafts are shorter and are not exposed. Additionally, shaft alignment issues are avoided with this approach.

Extensive efforts were made to ensure that the ECVT modification did not impact cooling or lubrication characteristics by inadvertently hindering or enhancing oil flow. The system depends greatly on proper oil circulation for heat conduction and lubrication. Oil is circulated with a mechanically driven trochoid oil pump and an electrically driven trochoid oil pump. Consideration of proper shaft support was also an important part of the process to ensure that no bearings were overloaded. A heat exchanger located off the side of the ECVT is in series with the inverter. Thermocouples were strategically placed to monitor stator, inner/outer case, and oil temperatures both near and far from the heat exchanger.

Additional instrumentation was added to the ECVT and PCU and a data acquisition system was developed to collect thermal, mechanical, and electrical data such as coolant temperatures, heat sink temperatures, torque, speed, currents, and voltages. These data were collected, fed into an immense spreadsheet, and saved for future use. An optimal control scheme was developed to ensure the most efficient operation of the motor throughout the entire operation range. The controller used speed, position, and current feedback to regulate the output conditions supplied by the inverter. The original equipment manufacturer motor inverter controls were bypassed to allow full control over the inverter, enabling uninhibited testing of the system over various operation conditions.

Back- emf tests were conducted by spinning the permanent magnet synchronous motor rotor with a secondary motor as the voltages across the open motor leads were measured. These tests provided information about the air gap flux due to the permanent magnets, as the induced back-emf voltage is proportional to speed and permanent magnet flux. Locked rotor torques were measured as a positive dc current was fed to phase “a” and returned through phases “b” and “c” connected in parallel, and the rotor position was swept through an entire electrical cycle. The torque measurements for stator currents of 50, 100, 150, and 200 A are shown in Fig. 6. To avoid extreme stator temperatures and possible stator damage, measurements were taken only during the peak torque region for the higher dc currents of 250, 300, 350, and 400 A. Compared with the Camry, the LS600h has a considerably lower torque per current ratio for currents of up to about 250 A. Beyond this dc current level, Camry locked rotor test results revealed substantial effects of saturation; the LS600h did not sustain such detriments and had a much higher torque per current ratio at currents near 400 A. Although the LS600h motor has a smaller diameter, its increased stack length leads to a greater air-gap surface area than that of the Camry. Therefore, even though fewer turns can be fit into the small slots and thereby the torque per current ratio decreases, the larger surface area is less susceptible to saturation.

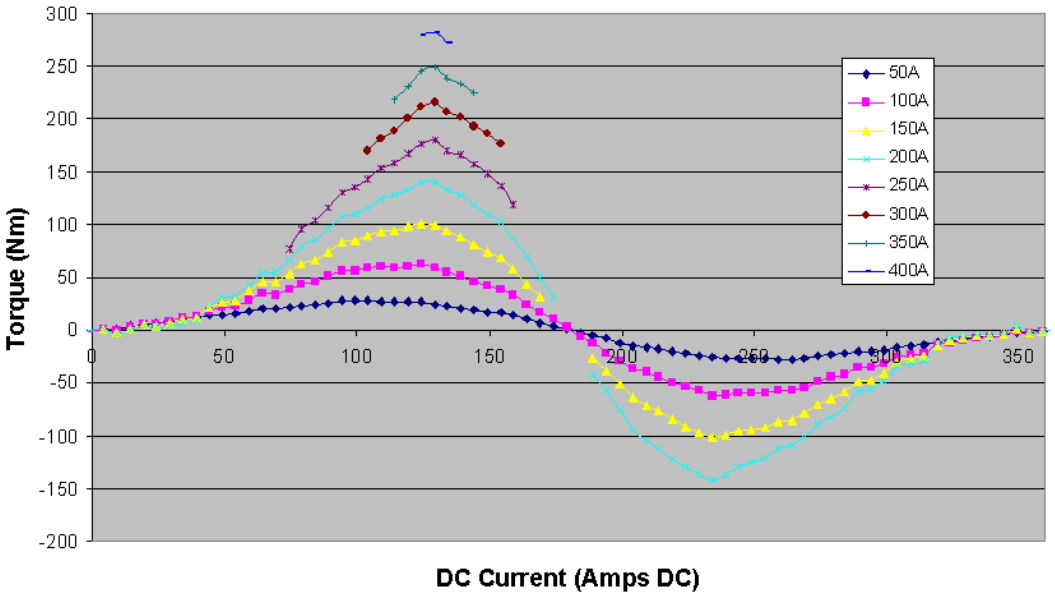

Fig. 6. 2008 Lexus LS600h locked rotor test results.

Efficiency measurements of the motor and inverter were taken over the entire operation range of the motor. The efficiency contour map in Fig. 7 represents the steady state efficiency characteristics of the motor for efficiencies above 50%. Compared with the efficiency map of the Camry, the advantages of the Lexus motor become apparent. The peak efficiency of 95% as well as efficiencies above 88% are spread out over a much a larger area of the operation region. Note that for much of the high-torque regions, a coolant temperature of ~0°C was used to permit extensive testing in this region. Otherwise, the torque levels nearing 300 Nm could be maintained only for extremely short periods of time before reaching stator temperature limits. Although the published peak power was verified with ~0°C coolant, operation could not be held at this power level for an 18 second duty. Further testing revealed that the motor is capable of producing 110 kW for 18 seconds before reaching a stator temperature of 180°C. However, in practice, the stator temperature limit is likely set to be much lower, and normal stator temperatures are near 100°C. Thus, only a very short duration of high-current operation is possible in most cases. Note that it appears the motor is capable of operating above its rated speed, as the torque was not reduced significantly at 10,000 rpm. However, the speed limitation was likely due to the mechanical stress of retaining the additional magnet.

Continuous tests were conducted at 25kW and 50 kW at 3,000, 5,000, and 7,000 rpm with a constant coolant temperature of 50°C. Stator winding, internal/external case, inverter, and coolant temperatures were measured throughout the tests. Shown in Fig. 8 are the results from a test conducted at 50 kW and 3,000 rpm. The hottest location in the motor is near the upper portion of the stator, which is farthest from the heat exchanger, as indicated by the light blue line. This particular test condition was maintained for about 3.3 minutes, at which time a stator temperature of 150°C was reached. For the same conditions, 50 kW was maintained at 5,000 rpm for about 14.2 minutes and at 7,000 rpm for about 18.5 minutes until a stator temperature of 150°C was reached. The duration of operation at a specific power level was significantly affected by speed, coolant temperature, and temperature restraints placed on the stator.

Additional data, further analyses, and more elaborate documentation of the findings and results from the FY 2008 benchmarking efforts can be found in [1].

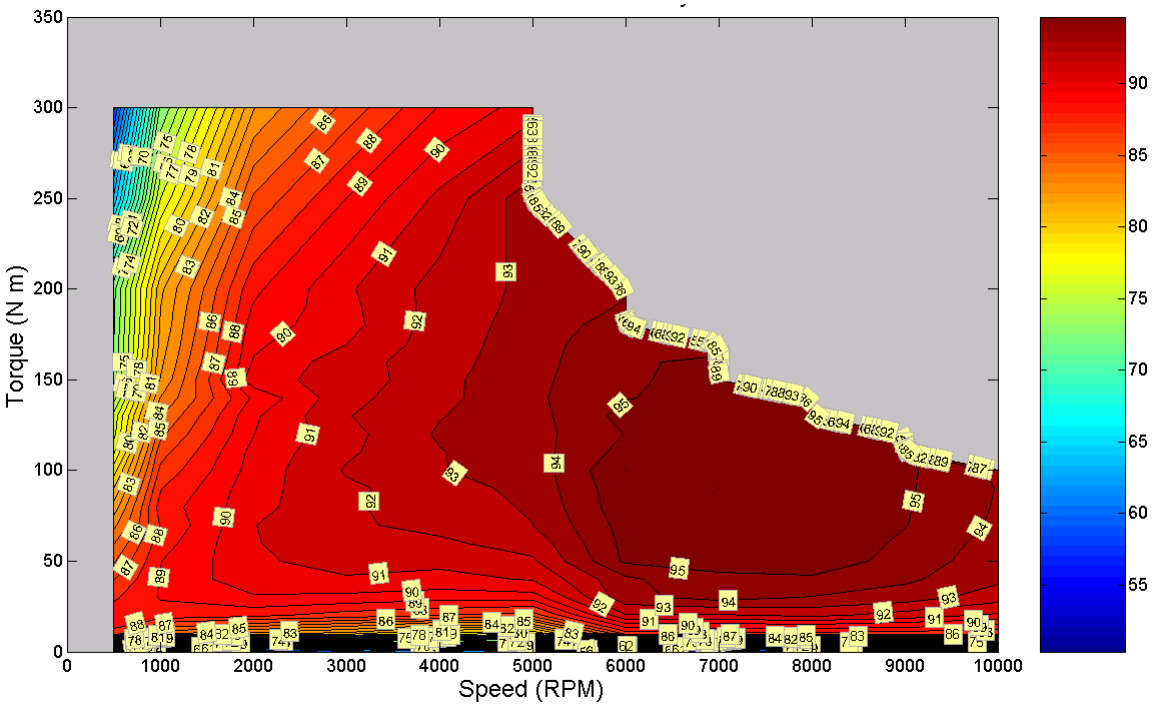

Fig. 7. 2008 Lexus LS600h motor efficiency map.

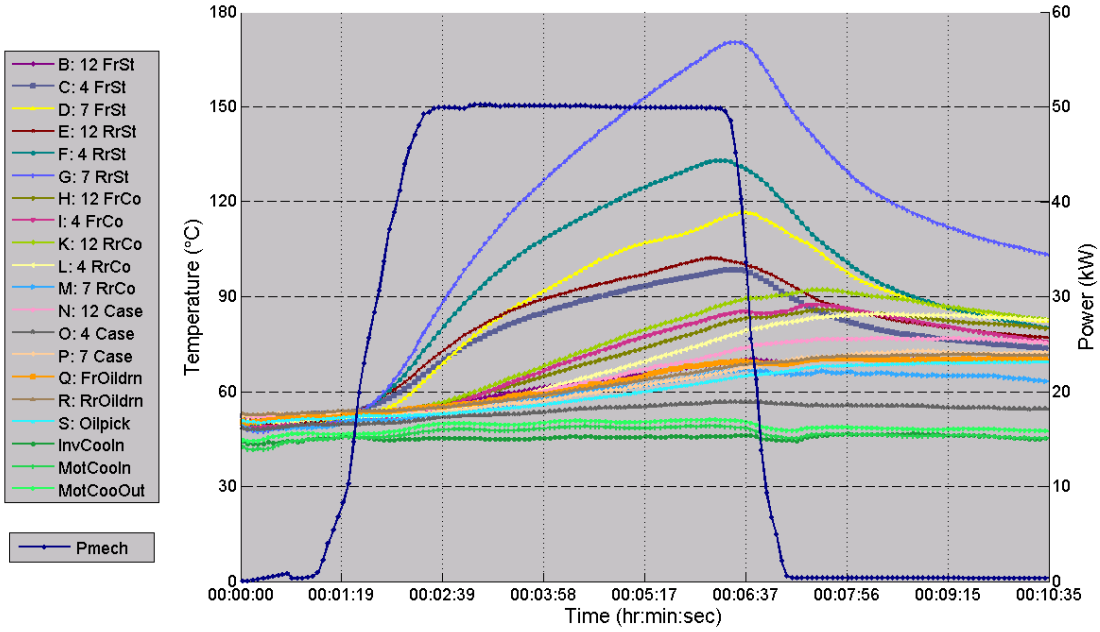

Fig. 8. 2008 LS600h continuous tests at 50 kW and 3,000 rpm.

Conclusions

- Benefits of the double-sided cooling technique lead to immense advances in inverter specific power and power density (about a 50% increase)
- The IGBT and diode count is reduced, even though the LS600h has a higher power rating than the Camry.
- Cost of some PCU components may not be advantageous.
- Motor stator outer diameter is reduced to 76% that of the Camry.
- Motor lamination stack length is more than doubled.
- Air-gap surface area is significantly larger than in the Camry but uses only 7.92 lb of copper vs 12.5 lb in the Camry.
- Motor magnet mass increased from ~2 to ~3lb.
- Power density of the Lexus motor has been improved to 2.5 kW/kg from 1.7 kW/kg in the Camry.
- Specific power of the Lexus motor has been improved to 6.6 kW/L from 5.9 kW/L in the Camry.
- Torque per current suffers at low currents but is superior at high currents.
- Motor efficiencies are above 90% for a great portion of the operation range, even better than the Camry.
- The 18 second peak power capability of the primary Lexus motor is about 110 kW at 5,000 rpm.
- Continuous duration varies significantly with speed and specified stator temperature limit. A power level of 50 kW was maintained at 7,000 rpm for about 18.5 minutes, at which a stator temperature of 150°C was reached.

Publications

1. T. A. Burress, et al., *Evaluation of the 2008 Lexus LS600h Hybrid Synergy Drive System*, ORNL/TM-2008/185, Oak Ridge National Laboratory, 2008.

T. A. Burress
C. L. Coomer
S. L. Campbell
L. E. Seiber
L. D. Marlino
J. P. Cunningham
A. A. Wereszczak

References

1. T. A. Burress, C. L. Coomer, S. L. Campbell, L. E. Seiber, L. D. Marlino, R. H. Staunton, and J. P. Cunningham, *Evaluation of the 2007 Toyota Camry Hybrid Synergy Drive System*, ORNL/TM-2007/190, Oak Ridge National Laboratory, 2007.

DISTRIBUTION

Internal

1. D. J. Adams
2. K. P. Gambrell
3. J. B. Green, Jr.
4. L. D. Marlino
5. M. Olszewski
6. Laboratory Records
   Authors
   Co-Authors

External

7. R. Al-Attar, DCX, raa9@chrysler.com.
8. S. J. Boyd, U.S. Department of Energy, EE-2G/Forrestal Building, 1000 Independence Avenue, S.W., Washington, D.C. 20585.
9. J. Czubay, General Motors Corporation, GM Powertrain Headquarters, Mail Code: 483-710-270, 895 Joslyn Avenue, Pontiac, Michigan 48340.
10. H. Dadkhah, Chrysler, LLC, CIMS 526-00-00, 1960 Technology Drive, Building D, Troy, Michigan 48083.
11. P. B. Davis, U.S. Department of Energy, EE-2G/Forrestal Building, 1000 Independence Avenue, S.W., Washington, D.C. 20585.
12. R. R. Fessler, BIZTEK Consulting, Inc., 820 Roslyn Place, Evanston, Illinois 60201-1724.
13. S. Gopalakrishnan, General Motors Corporation, RMB-356, Mail Code 480-106-390, 30500 Mound Road, Warren, Michigan 48090.
14. G. Hagey, 501 Randolph St., Williamsburg, Virginia 23185.
15. E. Jih, Ford Motor Company, Scientific Research Laboratory, 2101 Village Road, MD-1170, Rm. 2331, Dearborn, Michigan 48121.
16. K. J. Kelly, National Renewable Energy Laboratory, 1617 Cole Boulevard, Golden, Colorado 80401.
17. F. Leonardi, Ford Motor Company, 15050 Commerce Drive, North, Dearborn, Michigan 48120-1261.
18. F. Liang, Ford Motor Company, Scientific Research Laboratory, 2101 Village Road, MD1170, Rm. 2331/SRL, Dearborn, Michigan 48121.
19. M. W. Lloyd, Energetics, Inc., 7164 Columbia Gateway Drive, Columbia, Maryland 21046.
20. M. Mehall, Ford Motor Company, Scientific Research Laboratory, 2101 Village Road, MD-2247, Rm. 3317, Dearborn, Michigan 48124-2053.
21. N. Olds, United States Council for Automotive Research (USCAR), nolds@uscar.org
22. S. A. Rogers, U.S. Department of Energy, EE-2G/Forrestal Building, 1000 Independence Avenue, S.W., Washington, D.C. 20585.
23. G. S. Smith, General Motors Advanced Technology Center, 3050 Lomita Boulevard, Torrance, California 90505.
24. R. A. Sullivan, U.S. Department of Energy, EE-2G/Forrestal Building, 1000 Independence Avenue, S.W., Washington, D.C. 20585.